The role of LRRK2 in lung adenocarcinoma

Aspasia GKASTI

Acknowledgments

`*Life is like riding a bicycle. To keep your balance, you must keep moving*`, as Albert Einstein once said. That is a quote that accompanied me all the five years of my PhD studies. A lot of different circumstances some easier than others, which triggered a lot of emotions, that made me stronger to never give up my goals and helped me to grow as a scientist but mainly as a person. The completion of the PhD thesis would not have been possible without the immense support of people from the working and non-working environments.

First, I would like to thank my two thesis supervisors Prof. Daniel Constam and Prof. Etienne Meylan. It would not have been possible for me to start or continue my PhD studies without them. So, I would like to thank you for accepting me into our labs, for the scientific advice, and for all the conversations we had together.

I would also like to thank my jury members for accepting my invitation to participate in my oral exam and evaluate my thesis. Thank you, Prof. Lingner, for being my mentor and the president of my private defense jury. Thank you Dr.Perentes and Prof. Konstantinidou for being my external experts and Dr. Scnheider for being my internal expert.

Then, I would like to thank some people from the Constam`s and the former Meylan`s laboratories who helped me adapt to the new environments, taught me tons of molecular techniques, and made the lab life more joyful. I would first like to thank Julien, who was my master's thesis supervisor back in 2018. Thank you for welcoming me into the lab, for teaching me how to use multiple techniques including flow cytometry, for trusting me to work with you on a collaboration you had, and for supporting me to continue with PhD studies. Silvia, thank you for your kindness and openness and you Christine for all the administrative support, as well as the long discussions especially in difficult times. Nadine, thank you for your bioinformatics support and your warmth. Caroline, Pierre-Benoit, and Gael, I appreciate the good times in the lab and the intensive dive into the French culture. But among the former people of Meylan lab, a special thank goes to Anita, with whom we experienced and overcame together difficult circumstances and shared feelings in uncertain times. From the Constam lab, I would like to thank Cece for the friendship, openness, laughs, and long talks about our projects and about funny and weird things that were happening in our everyday lives. I am also very thankful to Olga for the friendship, the support, the long talks (scientific or not), and the fun times in and outside the lab. Lei, thank you for the unlimited positivity you spread around you, the laughs, and the conversations. I am also grateful to have had Ben, sitting next

Abstract

Lung cancer is the leading cause of cancer-related deaths worldwide and the most common lung cancer subtype is lung adenocarcinoma (LUAD). Frequently mutated genes involve activating mutations in *KRAS* and loss of function mutations in *TP53.* LUADs primarily arise from alveolar type II cells (ATII), a very specialized lung epithelial cell type that is characterized by the expression of surfactant protein C (SPC). During tumor progression, cancer cells undergo de-differentiation to adapt and survive in the continuously changing tumor environment. Changes may include the upregulation of genes like the glucose transporter 1 (*Glut1*) which facilitates the uptake of glucose, and the downregulation of others, like the Leucin-rich repeat kinase 2 (*Lrrk2*). Lrrk2 is a multidomain protein that has both a kinase and a GTP catalytic activity and point mutations of it have been linked with Parkinson's disease (PD). R1441C Lrrk2 is one of the PD mutations that is found in the GTP domain and affects positively the kinase activity of the enzyme.

In our study, we focused on the role of Lrrk2 in lung adenocarcinoma. For that, we used the transgenic mouse model *Kras* $^{LSL-G12D/WT}$*; Tp53* $^{fl/fl}$ (KP), in which we intratracheally instilled Ad5.SPC-Cre viral vectors to specifically target ATII cells (SPC+) and initiate tumors. In a transcriptomic analysis of magnetically sorted CD45 negative KP and *Kras* $^{LSL-G12D/WT}$*; Tp53* $^{fl/fl}$*; Glut1* $^{fl/fl}$ (KPG1) tumors cells, we found that *Lrrk2* together with some other genes that are important for the lamellar bodies were downregulated in KP cells. Lamellar bodies (LBs) are lysosome-related organelles that are produced and stored by ATII cells. In normal lungs, they store surfactant that they release in the alveolar space to reduce the tension in the air-liquid interface. Bioinformatic analysis of LUAD patient data from the cancer genome atlas (TCGA) database, revealed that the high *LRRK2* expression correlates with better patient survival and that this *LRRK2*-high group, maintains genes that are enriched in normal ATII cells, like surfactant protein C (*STFPC*) and ATP-cassette transporter A3 (*ABCA3*). Overexpression of *LRRK2* in human lung cancer cell lines induced their apoptotic cell death *in vitro*. Thus, the positive correlation of the *LRRK2*-high group with a better patient outcome and the cell death induction upon *LRRK2* overexpression, made us hypothesize that *LRRK2* acts as a tumor suppressor for lung cancer cells. To elucidate that, we crossed KP with *Lrrk2* $^{R1441C/Wild-Type}$ (L) mice to generate the *Kras* $^{LSL-G12D/WT}$*; Tp53* $^{fl/fl}$*; Lrrk2* $^{R1441C/Wild-Type}$ (KPL) mouse model. First, analysis of healthy wild-type and R1441C Lrrk2 lungs revealed no morphological and ultrastructural changes in the ATII cells and their LBs respectively. Localization of Lrrk2 in the pro-SPC + regions in ATII cells implies a functional role of Lrrrk2 in the LBs. Furthermore, tumor-bearing KPL mice did not show a consistent reduction in their tumor growth rate, while quantification of the Lrrk2 protein levels by immunofluorescence revealed that KPL cells maintain more Lrrk2 protein levels than KPs. Finally, considering together RNA-sequencing, *in vitro,* and *in vivo* results, we think that both the wild-type and R1441C Lrrk2 can inhibit autophagy, with this effect being exacerbated in mutant cells. We hypothesize that Lrrk2 regulates autophagy via inhibition of the PI3K-II/Beclin-1 pathway, which could potentially regulate early lung tumor development.

Keywords: Lung adenocarcinoma, KP mice, Lrrk2, R1441C Lrrk2, lamellar body, PD-linked mutation.

Résumé

Le cancer du poumon est la principale cause de décès liés au cancer dans le monde, et le sous-type le plus courant de cancer du poumon est l'adénocarcinome pulmonaire (LUAD). Les gènes fréquemment mutés impliquent des mutations activatrices dans KRAS et des mutations de perte de fonction dans TP53. Les LUAD proviennent principalement des cellules de type II alvéolaire (ATII), un type de cellule épithéliale pulmonaire très spécialisé caractérisé par l'expression de la protéine surfactante C (SPC). Au cours de la progression tumorale, les cellules cancéreuses subissent une dédifférenciation afin de s'adapter et de survivre dans un environnement tumoral en constante évolution. Ces changements peuvent inclure la surexpression de gènes tels que le transporteur du glucose 1 (Glut1), qui facilite l'absorption du glucose, et la sous-régulation d'autres gènes, comme la leucine-rich repeat kinase 2 (Lrrk2). Lrrk2 est une protéine multidomaine qui possède à la fois une activité kinase et une activité catalytique GTP, et des mutations ponctuelles de celle-ci ont été liées à la maladie de Parkinson (PD). La mutation R1441C de Lrrk2 est l'une des mutations de la PD qui se trouve dans le domaine GTP et affecte positivement l'activité kinase de l'enzyme.

Dans notre étude, nous nous sommes concentrés sur le rôle de Lrrk2 dans l'adénocarcinome pulmonaire. Pour cela, nous avons utilisé le modèle de souris transgénique Kras $^{LSL-G12D/WT}$; Tp53 $^{fl/fl}$ (KP), dans lequel nous avons instillé intratrachéalement des vecteurs viraux Ad5.SPC-Cre pour cibler spécifiquement les cellules ATII (SPC+) et initier des tumeurs. Dans une analyse transcriptomique des cellules tumorales magnétiquement triées CD45 négatives KP et Kras $^{LSL-G12D/WT}$; Tp53 $^{fl/fl}$; Glut1 $^{fl/fl}$ (KPG1), nous avons constaté que Lrrk2 ainsi que d'autres gènes importants pour les corps lamellaires étaient sous-régulés dans les cellules KP. Les corps lamellaires (LB) sont des organites liés aux lysosomes produits et stockés par les cellules ATII. Dans les poumons normaux, ils stockent le surfactant qu'ils libèrent dans l'espace alvéolaire pour réduire la tension à l'interface air-liquide. L'analyse bioinformatique des données de patients LUAD provenant de la base de données du cancer genome atlas (TCGA) a révélé que l'expression élevée de LRRK2 était corrélée à une meilleure survie des patients et que ce groupe à haute LRRK2 maintenait des gènes enrichis dans les cellules ATII normales, tels que la protéine surfactante C (STFPC) et le transporteur A3 à cassette ATP (ABCA3). La surexpression de LRRK2 dans des lignées cellulaires de cancer du poumon humain a induit leur mort cellulaire apoptotique in vitro. Ainsi, la corrélation positive du groupe à haute LRRK2 avec un meilleur résultat pour les patients et l'induction de la mort cellulaire par surexpression de LRRK2 nous ont amenés à formuler l'hypothèse que LRRK2 agit comme un suppresseur de tumeur pour les cellules du cancer du poumon. Pour élucider cela, nous avons croisé KP avec des souris Lrrk2 $^{R1441C/Wild-Type}$ (L) pour générer le modèle de souris Kras $^{LSL-G12D/}$WT ; Tp53 $^{fl/fl}$; Lrrk2 $^{R1441C/Wild-Type}$ (KPL). Tout d'abord, l'analyse des poumons sains de type sauvage et de Lrrk2 R1441C n'a révélé aucun changement morphologique et ultrastructural dans les cellules ATII et leurs LB respectivement. La localisation de Lrrk2 dans les régions pro-SPC+ des cellules ATII implique un rôle fonctionnel de Lrrk2 dans les LB. De plus, les souris KPL porteuses de tumeurs n'ont pas montré de réduction cohérente de leur taux de croissance tumorale, et la quantification des niveaux de protéine Lrrk2 par immunofluorescence a révélé que les cellules KPL maintenaient plus de niveaux de protéine Lrrk2 que les cellules KP. Enfin, en tenant compte des résultats de la séquençage d'ARN, in vitro et in vivo, nous pensons que tant le Lrrk2 de type sauvage que le Lrrk2 R1441C peuvent inhiber l'autophagie, avec cet effet étant exacerbé dans les cellules mutantes. Nous

suggérons que Lrrk2 régule l'autophagie en inhibant la voie PI3K-II/Beclin-1, qui à son tour peut réguler la croissance tumorale.

Mot clés: Adénocarcinome du poumon, souris KP, Lrrk2, R1441C Lrrk2, corps lamellaire, mutations liées à la PD

Table of Contents

List of figures

List of tables

Acronyms and Abbreviations

A

ABCA3	ATP-binding cassette transporter A3
AH	Alveolar hyperplasia
AMPK	5′ AMP-activated protein
ANK	Ankyrin repeat
ARM	Armadillo repeat motif
ASOs	Antisense oligonucleotides
ATG	Autophagy-related genes
ATI	Alveolar type I cells
ATII	Alveolar type II cells

B

BADJs	Bronchioalveolar-duct junctions
BALF	Bronchoalveolar lavage fluids
BASCs	Bronchioalveolar stem cells
BLOC	Biogenesis of lysosome-related organelles complex

C

CaMK	Ca2+/calmodulin-dependent protein kinase
CARM1	Coactivator-associated arginine methyltransferase 1
CHIP	Heat shock protein 70 (Hsp70)-interacting protein
CMA	Chaperone-mediated autophagy
COR	C-terminal of ROC
CPT	Choline phosphotransferase

D

DAG	Diacylglycerol
DEGs	Differentially expressed genes
DPPC	Dipalmitoyl phosphatidylcholine
DSPG	Disaturated-phosphatidylglycerol

E

EGFR	Epidermal growth factor receptor
EM	Electron microscopy

F

FADD   FAS-associated death domain protein

G

GDP   Guanosine diphosphate

GEMMs   Genetically engineered mouse models

GLUT1   Glucose transporter 1

GTP   Guanosine triphosphate

H

HPS   Hermansky-Pudlak syndrome

Hsc70   Heat shock cognate 70 kDa protein

Hsp70   Heat shock protein 70

J

JIP4   JNK- interacting protein 4

K

KD   Knock-down

KI   Knock-in

KIN   Kinase domain

KO   Knock-out

KP   *Kras* $^{LSL\text{-}G12D/WT}$*; Tp53* $^{fl/fl}$

KPG1   *Kras* $^{LSL\text{-}G12D/WT}$*; Tp53* $^{fl/fl}$*; Glut1* $^{fl/fl}$

KPL   *Kras* $^{LSL\text{-}G12D/WT}$*; Tp53* $^{fl/fl}$*; Lrkk2* $^{R1441C/WT \ or \ R1441C/ \ R1441C}$

KRAS   Kirsten rat sarcoma 2 viral oncogene homolog

L

LAMP-2A   Lysosome-associated membrane protein type 2A

LAMP-3   Lysosome-associated membrane glycoprotein 3

LBO   Lamellar-body like organelles

LBs   Lamellar bodies

LC3B   Microtubule-associated protein 1A/1B-light chain 3B

LDs   Lipid droplets

LPCAT1   Acyl-CoA: lysophosphatidylcholine acyltransferase

LPS   Lipopolysaccharide

LROs   Lysosome-related organelles

LRR   Leucine-rich repeat

Lrrk1   Leucine-rich repeat kinase 1

LRRK2   human Leucine-rich repeat kinase 2

Lrrk2   Leucine-rich repeat kinase 2

LUAD   Lung Adenocarcinoma

M

mTOR   Mechanistic target of rapamycin

mut/mut   *Lrrk2* $^{R1441C\,/\,R1441C}$ alleles

mut/wt   *Lrrk2* $^{R1441C\,/\,wild\text{-}type}$ alleles

N

NAADP   Nicotinic acid adenine dinucleotide phosphate

NAD   Nicotinamide adenine dinucleotide

NESCs   Neuroepithelial stem cells

NK   Natural killer cells

non-TRU   Non-terminal respiratory unit

NSCLC   Non-small cell lung cancer

O

OCTX   Occipital cortex

ORO   Oil Red O

P

PC   Phosphatidylcholine

PD   Parkinson's disease

PG   Phosphatidylglycerol

PI   Proximal-proliferative

PKA   Protein kinase A

PP   Proimal-inflammatory

PREs   Pumilio response elements

pro-SPC   Premature surfactant protein C

PUM1   Pumilio 1

PUM2   Pumilio 2

R

ROC   Ras-of-Complex

ROS   Reactive oxygen species

S

S6K   Ribosomal protein S6 kinase

SCLC   Small-cell lung cancer

SN   Substantia nigra

SP-A   Surfactant protein A

SP-B   Surfactant protein B

SP-C   Surfactant protein C

SP1   Transcription factor specificity protein 1

T

TCGA   The Cancer Genome Atlas

TFEB   Transcription factor EB

TGN   Trans-Golgi network

TK   Tyrosine kinases

TKL   Tyrosine kinase-like kinase

TM   Tubular myelin

TP53   Tumor protein 53

TRU   Terminal respiratory unit

U

UPS   Ubiquitin-proteasome system

UTR   Untranslated regions

W

wt/wt   Lrrk2 wild-type alleles

µ

μCT   Micro-computed tomography

Chapter 1 - Introduction

1.1. Lung Cancer

1.1.1. Epidemiology

Lung cancer is the second-most frequently diagnosed cancer type in both men and women, accounting for 11.4% of estimated new cases worldwide (Figure 1a). It was ranked as the top cause of cancer-related deaths in 2020, having a mortality rate higher than breast and colorectal cancer combined, the other two most common cancer types (Figure 1b)[1]. Furthermore, the 5-year prospective survival of lung cancer patients is one of the lowest, as a result of late diagnosis, at advanced stages in which cancer cells have also metastasized to other organs, making the disease less curable. Interestingly, the percentage of people living for at least 3 years after the diagnosis rose from 19% in 2001 to 21% in 2004 and 31% in 2015 through 2017, with the median survival increasing from 8 to 13 months in the US during that same period[2].

Many risk factors play a role in the development of lung cancer; including tobacco use, alcohol consumption, unhealthy diet, physical inactivity, air pollution, and the genetic prevalence of mutations. Cigarette smoking is the main cause, accounting for more than 80% of lung cancer cases in the US[2].
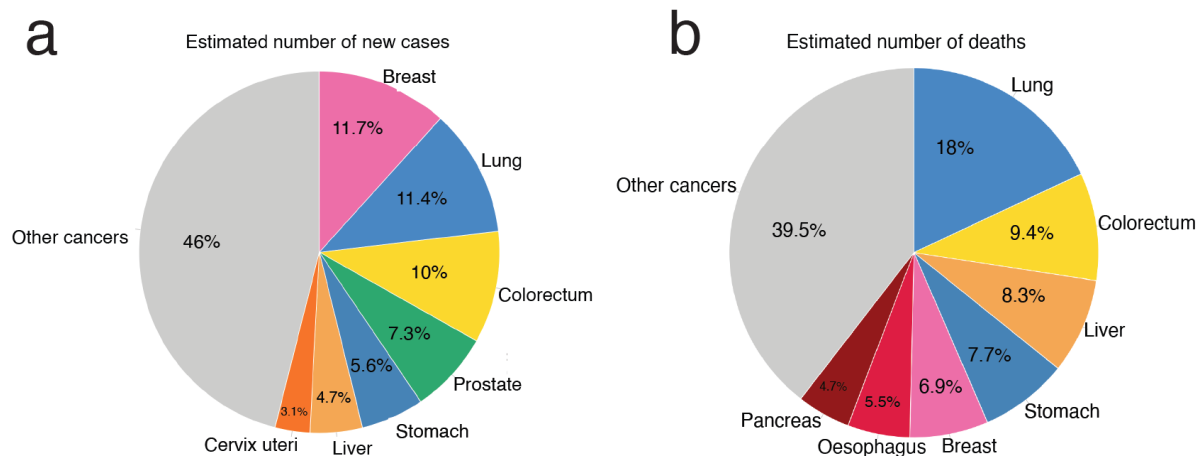
Figure 1. Worldwide estimation of the new cases and deaths of the top 10 most frequent cancer types in 2020. (**a**) Pie chart showing the percentage of estimated new cases for each cancer type over 5 years in 2020 for both men and women. (**b**) Pie chart showing the percentage of estimated deaths caused by each cancer type over 5 years in 2020 for both men and women. Source: GLOBOCAN 2020.

1.1.2. Lung cancer Subtypes

Lung cancer is histopathologically classified into two main types, the non-small cell lung cancer (NSCLC) and the small cell lung cancer (SCLC), which account for 81% and 13.5% of all lung cancer cases, respectively (Figure 2a). NSCLC can be further subdivided into Lung Adenocarcinoma (LUAD), Squamous Cell Carcinoma (SqCC), and Large Cell Carcinoma. LUAD is the leading lung cancer subtype, with an estimate of 57% in the US (Figure 2b). This classification is based on histopathological findings that mainly include the tumor cell morphology. To better evaluate and more accurately classify lung tumors, the guidelines for the new lung tumor classification, released in 2021 by the World Health Organization (WHO), emphasize the importance of the genetic and molecular testing that would supplement the histopathological findings. The aim of those guidelines is the use of more specific treatments that would eventually lead to personalized therapies and more efficient treatment of the lung cancer patients [3,4].
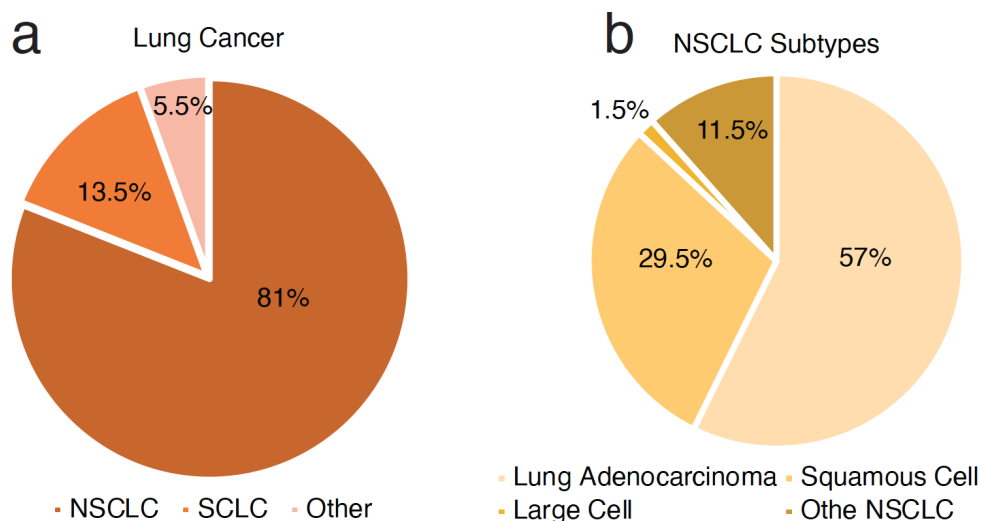
Figure 2. Frequency of lung cancer types of both men and women in the US, in the years 2015-2019. (**a**) Pie chart illustrating the percentages of the main lung cancer types. NSCLC; Non-small cell

lung cancer, SCLC; Small cell lung cancer. (**b**) Pie chart showing the percentages of NSCLC subtypes. Source: American Society, Inc. Surveillance and Health Equity Science, 2023.

1.2.   Lung Adenocarcinoma (LUAD)

1.2.1. Genetic alterations in LUAD

A large-scale sequencing study performed in 441 tumors including lung, ovarian, breast, and prostate cancers and their subtypes revealed that LUAD tumors have the highest mutation rate of 3.5 per Mb [5]. It was found that there are 22 to 26 genes that are the most frequently mutated genes in LUAD, that include oncogenes; *KRAS*, *EGFR, ALK, ERBB2, BRAF* and tumor suppressors; *TP53, PTEN,* and *CDKN2A. The* top three most commonly altered genes are the tumor protein 53 (*TP53),* Kirsten rat sarcoma 2 viral oncogene Homolog (*KRAS),* and epidermal growth factor receptor *(EGFR)* [4,6]. *TP53* encodes the transcription factor p53 which regulates programs crucial for the cell cycle arrest, apoptosis, metabolism, autophagy, and senescence [7,8]. In LUAD, *TP53* is mutated in almost 50% of all cases (Figure 3). Typically these mutations result in either complete loss of p53 protein function or dominant negative activity of the mutant protein which is induced upon its dimerization with a wild-type p53 [9].

KRAS encodes for a GTPase, KRAS, that is active and signals when guanosine triphosphate (GTP) is bound on it while becoming inactive when the γ phosphate of GTP is hydrolyzed and converted into guanosine diphosphate (GDP). Multiple extracellular stimuli can activate KRAS, which can then transduce the signals to downstream effectors pathways, including the mitogen-activated protein kinase (MAPK) and phosphoinositide 3-kinase (PI3K). KRAS regulates fundamental cell processes such as cell survival, cell differentiation, and cell proliferation [10,11]. Mutations in this gene account for 20-30% of LUAD patients (Figure 3). Oncogenic mutations in KRAS are missense mutations in the glycine at position 12, or of glutamine (Gln) at position 61. Glycine 12 is substituted by cysteine (G12C), valine (G12V), or aspartic acid (G12D) in 39%, 18%, and 18% of the total *KRAS* mutant patients respectively. The G12D is also the most common *KRAS* mutation in non-

smokers and, similar to the other mutations, causes a reduction in the GTPase activity of the enzyme, resulting in increased signaling to its downstream effectors [12].

KRAS mutations have been shown to co-occur with alterations in other genes in NSCLC [13,14]. More specifically, *TP53* and Serine/Threonine Kinase 11 (*STK11*) are two tumor suppressor genes that are simultaneously mutated with *KRAS* in 42% and 29% of NSCLC patients examined [13]. The different pair of mutations drive the activation of different signaling pathways that affect different biological processes [13-15]. Before lung cancer patients get into a treatment, the genetic background of their lesions is an important factor to be considered for a more efficient combatting of the disease.

Histotype	Type of genomic aberrations	Gene		Frequency (%)
NSCLC LUAD	Fusions	ALK		3-7
		ROS1		2-3
		RET		1-2
		NTRK1		1-2
	Mutations	EGFR		30-40
		BRAF		0.5-5
		KRAS		20-30
		MET		3-4
		PTEN		1.7
		PDGFRA		6-7
		PIK3CA		5
		TP53		52
	Copy number gene alterations	Gains	ERBB2	2-5
			EGFR	10
			MET	2-5
			TERT	75
		Losses	CDKN2A	7

Figure 3. Genetic landscape of lung adenocarcinoma cells. Table illustrating the genes that are most commonly mutated in lung adenocarcinoma, the type, and the frequency of those mutations. Source: Marino et al., 2019.

1.2.2. Engineered mouse models for LUAD

To study and recapitulate the human LUAD in mice, genetically engineered mouse models (GEMMs) have been developed, two of them being the *Kras* $^{G12D/wt}$ and the *Kras* $^{G12D/wt}$*; Tp53* $^{fl/fl}$.

The *Kras* $^{G12D/wt}$ (K) mouse model is a conditional knock-in model that harbors a wild-type (wt) and a knock-in *KrasG12D* allele, with the latter having a *LoxP-Stop-LoxP* cassette before the first exon of the mutant *Kras*. The expression of this conditional oncogenic mutant *KrasG12D* allele is induced upon homologous recombination of the *LoxP* sites, by the Cre recombinase. The delivery of the enzyme to the alveolar space is performed through intratracheal or intranasal instillation of mice with adenoviral or lentiviral vectors that express the Cre recombinase upon epithelial cell transduction. Lung tumors arising from these mice are mostly adenomas, hence this mouse model is usually used to recapitulate human LUAD at an early tumor stage [16,17].

For a faster progression of lung tumors, the *Kras* $^{G12D/wt}$*; Tp53* $^{fl/fl}$ (KP) mouse model was generated. These carry one copy of the aforementioned conditional, Cre-inducible *KrasG12D* allele described before and the *Tp53* gene is flanked with *LoxP* sites in both alleles. Thus, upon delivery of Cre-recombinase, there is a deletion of *Tp53* in both alleles and expression of the mutant *Kras* $^{G12D/wt}$. Lung tumors arising from these KP mice develop to more advanced stages than the K mouse model, progressing from alveolar hyperplasia (AH) to metastatic carcinoma tumor grade 5 [17,18]. The grading of those lesions is based on morphological changes mainly in their nuclei and performed according to the previously described grading system [18]. Grade 1 tumors have regular nuclear morphology, while Grade 2 tumor cells have more enlarged nuclei, accompanied sometimes by nucleoli. In Grade 3, the cells have distorted big nuclei and exhibit the presence of nucleoli, whereas Grade 4 tumor cells are characterized by a high degree of nuclear atypia, with abnormally enlarged and hyperchromatic nuclei. Finally, Grade 5 tumors have all the characteristics of grade 4 plus an unusual growth of fibrous tissue surrounding tumor cells [18].

1.2.3. Cells of origin of LUAD

Both in LUAD patients as well as in the established LUAD mouse models mentioned before, tumors develop in the periphery of the lungs [17,19]. Four main epithelial cell types comprise the distal airways; the alveolar type I and type II cells (ATI and ATII), the club cells (formerly known as Clara cells), and the bronchioalveolar stem cells (BASCs) (Figure 4) [20,21].

ATII cells are cuboidal epithelial cells that serve as progenitors of ATI, playing a crucial role in the alveolar epithelial repair and regeneration upon lung injury [22-23]. Their main function is the production and storage of pulmonary surfactant that is secreted in the alveolar space, to thereby decrease the air-liquid surface tension while breathing, and to provide a host defense mechanism. ATII cells are characterized by the surfactant protein C (SPC+) expression [24]. On the other hand, ATI are thin epithelial cells that cover approximately 95% of the internal lung surface area. They play a role in the gas exchange and are characterized by the expression of podoplanin (Pdpn). Club cells are non-ciliated secretory epithelial cells that contribute to lung homeostasis, and regeneration, as well as to host defense and protection against lung inflammation and damage. They are characterized by the expression of club cell-specific protein 10 (CC10+) [25,26]. Finally, BASCs are found at the bronchioalveolar-duct junctions (BADJs). They are multipotent lung epithelial stem cells that contribute to lung regeneration or repair upon lung injury and express both SPC and CC10 protein markers (SPC+ CC10+) [21].

Sutherland et al. demonstrated that both ATII (SPC+) and club cells (CC10+) can initiate and sustain malignant transformation upon *KrasG12D* expression in combination or not with *Tp53* loss, with the ATII cells (SPC+) being the most prevalent cell of origin for LUAD. Interestingly, it was described that club cells (CC10+) can transdifferentiate into SPC+ cells and in this way, tumor cells were able to sustain the malignant phenotype. LUADs arising from ATII (SPC+) or club cells (CC10+) are characterized by different histopathological features [27]. On the other hand, the lack of tumor formation by BASCs (SPC+ CC10+), suggests that this is not the cell type from which adenocarcinomas arise [27,28].
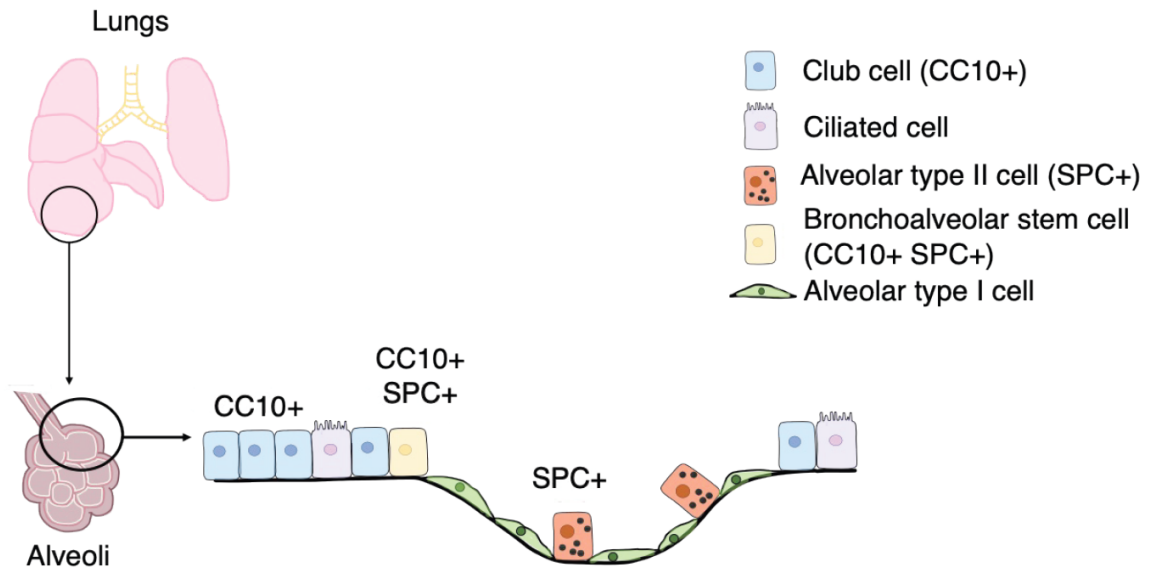
Figure 4. Prevalent cells of origin of lung adenocarcinoma. Epithelial cells in the alveoli of the distal airways**.** Alveolar type II cells are characterized by the SP-C protein expression (SPC+). Club cells are marked by the expression of the CC-10 (CC10+), whereas bronchoalveolar stem cells express both SP-C and CC-10 proteins (SPC+ CC10+). Alveolar type II cells (SPC+) and club cells (CC10+) are the two cell types that give rise to lung adenocarcinomas, with the ATII cells being the most predominant ones.

1.2.4. Autophagy in LUAD

Autophagy is a cellular process that involves the degradation and recycling of cellular components. There are three main types: macro-autophagy, micro-autophagy, and chaperone-mediated autophagy (CMA). Autophagy is mainly regulated by the inhibition of the mechanistic target of rapamycin (mTOR) or the activation of 5′ AMP-activated protein kinase (AMPK). Both mTOR inhibition and AMPK activation serve as inducers of autophagy in response to stressors such as starvation. The transcription factor EB (TFEB) then plays a crucial role as a positive regulator of autophagy and lysosomal biogenesis. Translocation of TFEB to the nucleus is inhibited upon phosphorylation by mTOR and induced upon phosphorylation by AMPK [29,30].

The role of autophagosomes is to engulf damaged or unnecessary cellular components, such as organelles or cytosolic proteins for their delivery to lysosomes. Autophagosome formation is initiated by membrane nucleation, followed by elongation

of the nascent membrane bilayer, and maturation (Figure 5). The autophagy-related (ATG) protein family contributes significantly to each of these steps. In addition, autophagosome formation depends on the microtubule-associated protein 1A/1B-light chain 3B (LC3B) [31,32]. Once the autophagosomes have been fully formed, they fuse with lysosomes, which contain enzymes that break down the engulfed material into its basic components, such as amino acids, nucleotides, and fatty acids. These recycled building blocks can be used by the cell to generate new cellular structures and energy.

Autophagy has been shown to play a crucial role in cancer. More specifically, in *Kras*-driven lung cancers, deletion of the *atg7* gene blocked the growth of lung tumor cells and altered the normal function of mitochondria. Since *Kras* $^{G12D/wt}$; *Atg7$^{-/-}$* or *Kras$^{G12D/wt}$; TP53* $^{fl/fl}$; *Atg7$^{-/-}$* lung tumors do not progress to adenomas or adenocarcinomas, these hyperplastic lesions are classified as benign oncocytomas. Tumor cells in these lesions are characterized by the accumulation of lipid droplets, defective mitochondria, and proliferative arrest. Hence, autophagy regulates the progression and de-differentiation of lung tumor cells in *Kras*-driven lung cancers [33,34].
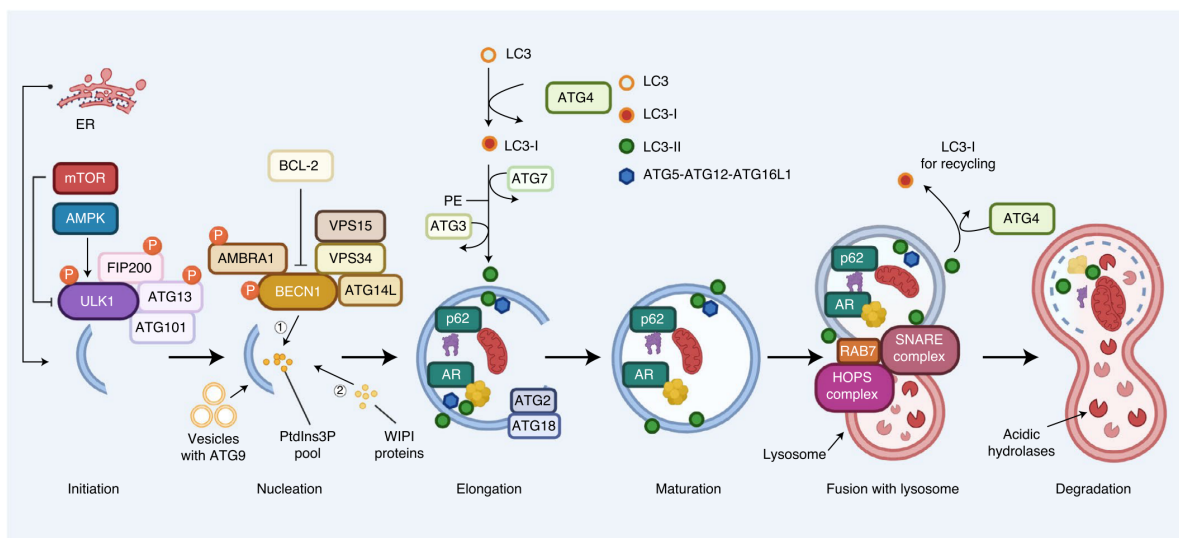
Figure 5. Autophagosome formation. This process can be dissected into five different steps: initiation, nucleation, membrane expansion/elongation, maturation, and fusion. Source: Y. Aman et al, 2022 [35].

1.3. Alveolar Type II cells

As stated above, ATII cells are secretory lung epithelial cells that represent the main cell of origin of LUAD [27]. Their principal function is the production and storage of pulmonary surfactant into specialized lysosome-related organelles (LROs) that are called lamellar bodies (LBs).

1.3.1. Lysosome-related organelles

Different types of lysosome-related organelles (LROs) are expressed by and stored in specialized cell types, providing cell-type-specific functions. LROs include the lamellar bodies in lung epithelial type II cells and keratinocytes, the Weibel-Palade bodies in endothelial cells, the melanosomes in melanocytes, retinal and iris pigment epithelial cells, and the basophilic granules in basophils and mast cells [36]. LROs have many common characteristics with lysosomes including the presence of lysosomal proteins in their limiting membrane, such as the Lysosome-associated membrane glycoprotein 3 (Lamp-3) and an acidic luminal pH. LROs are characterized by their ability to secrete their contents, but different cargos in their lumen provide a distinct function to the cell type that produces them. The functions of LROs in different cell types are diverse and include the stimulation of lung plasticity, pigmentation, and immune response through the secretion of surfactant by ATII cells, secretion of melanin by melanosomes, or the release of basophilic granules by basophils upon inflammatory stimuli respectively.

LROs originate either from the trans-Golgi network (TGN) or the endocytic system (early, recycling, or late endosomes) [37], but the exact processes of LRO biogenesis and cargo delivery are not yet fully understood. LRO biogenesis involves several proteins of the SNARE family that generally regulate intracellular trafficking by mediating vesicle fusion events[38]. In addition, several Rab GTPases and proteins that regulate the SNARE family are involved as well [39].

1.3.2. Lung lamellar bodies

Lung LBs are LROs that are produced by and stored in ATII cells. They are characterized by a dense highly-structured multilamellar morphology in thin-layer electron microscopy (EM) [40]. LBs contain surfactant which consists of 90% of lipids and 8-10% of proteins. Surfactant is secreted in the alveolar space to facilitate breathing by reducing the tension in the air-liquid interface in the lungs [40,41]. After secretion, pulmonary surfactant is converted into tubular myelin (TM), forming a lipid layer in the alveoli [42,43] (Figure 6a-c).
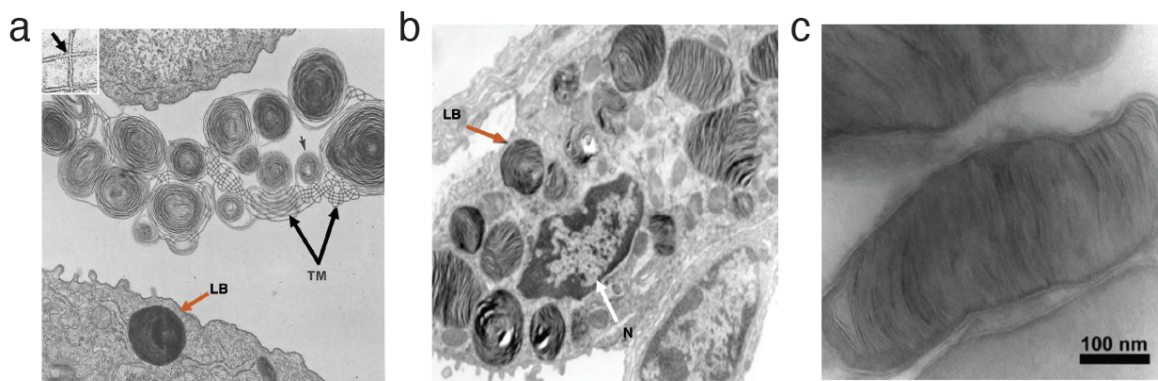
Figure 6. Morphology of lung lamellar bodies and tubular myelin in the alveolar type II cells and the alveoli. (**a**) Electron microscopy picture showing a lamellar body inside an alveolar type II cell and the structure of the secreted surfactant, which is converted into a lattice-like structure known as tubular myelin. (**b**) Electron microscopy picture showing multiple lamellar bodies sitting in the cytoplasm of an alveolar type II cell. (**c**)Higher magnification of an electron microscopy image showing the multilamellar structure observed in the lumen of the lamellar bodies. Black arrows, tubular myelin (TM) ; orange arrow, lamellar body (LB), white arrow, Nucleus (N). Source: Williams et al. 1977, Glasser et al, 2011, Ridsdale et al., 2011.

1.3.2.1. Main lipid and protein components of lung LBs

The major phospholipids of pulmonary surfactant are phosphatidylcholine (PC) and phosphatidylglycerol (PG), particularly dipalmitoyl phosphatidylcholine (DPPC) and disaturated-PG (DSPG), respectively [44,45] (Figure 7a). Surfactant synthesis requires *de novo* lipid synthesis (approximately 45%), or lipid recycling pathways (55-75%) [46]. ATII cells can recycle previously used lipids present in the alveolar space, or lipids that are released by neighboring cells, such as lipofibroblasts [47,48]. The *de novo*

synthesis of surfactant is performed through the Kennedy pathway which includes the phosphorylation of choline, its conversion into CDP-choline, and the synthesis of DPPC by choline phosphotransferase (CPT) with the use of diacylglycerol (DAG) [49]. On the other hand, the recycling pathways involve the de-acylation of monounsaturated PC, followed by the re-acylation of the generated lyso-PC (LPC) with saturated species by acyl-CoA: lysophosphatidylcholine acyltransferase (LPCAT1) to be converted into DPPC [50-51].

Proteomic analysis of LBs isolated from rat lungs identified forty-four different proteins and classified them into eight functional categories, with the top three groups being calcium-binding, structural, and surfactant-related proteins [52] (Figure 7b). Among the surfactant-related proteins, the surfactant proteins (SP); SP-A, SP-B, and SP-C have been associated with the stability, assembling, and reconstruction of pulmonary-surfactant. SP-C is a hydrophobic 21-kDa protein (called pro-SPC) which is proteolytically cleaved to a mature 4.2-kDa peptide [53]. Its expression starts early during embryonic development once the lungs are forming. At this early stage, all epithelial cells of the developing airways express SP-C at high levels. Once the respiratory tubules have been fully formed, it is only the ATII cells and the BASCs that continue to express it, making this protein a specific marker for those cell types [54]. SP-C plays a role in the stabilization of the pulmonary surfactant in the alveoli and in quick forming of phospholipid films [55]. Surprisingly, deletion of *SP-C* did not alter the formation of LBs in ATII cells or TM in the alveolar space [56]. SP-B is a hydrophobic 24-kDa protein that is proteolytically cleaved to a mature 8.7-kDa peptide [57]. Deletion of *SP-B* has been shown to cause lethal respiratory distress in newborns. Interestingly *SP-B* knock-out mice lacked TM in their alveoli and had disorganised LBs, showing that SP-B protein is important for the package of surfactant phospholipids into multilamellar concentric structures in ATII cells [58]. Another surfactant protein, SP-A, is a hydrophilic protein that associates with phospholipids and plays an important role in the TM formation, the uptake of phospholipids through endocytosis by ATII cells, and their remodeling [42,47-59]. In addition to the surfactant proteins, the ATP-binding cassette transporter A3 (ABCA3) is considered a specific ATII cell marker. ABCA3 is a transmembrane lipid transporter that localizes at the limiting membrane of LBs. *Abca3* knock-out pups die after birth due to respiratory distress. Their ATII cells lack LBs, and show altered surfactant lipid synthesis as well as impaired processing of SP-B [59,60,61].
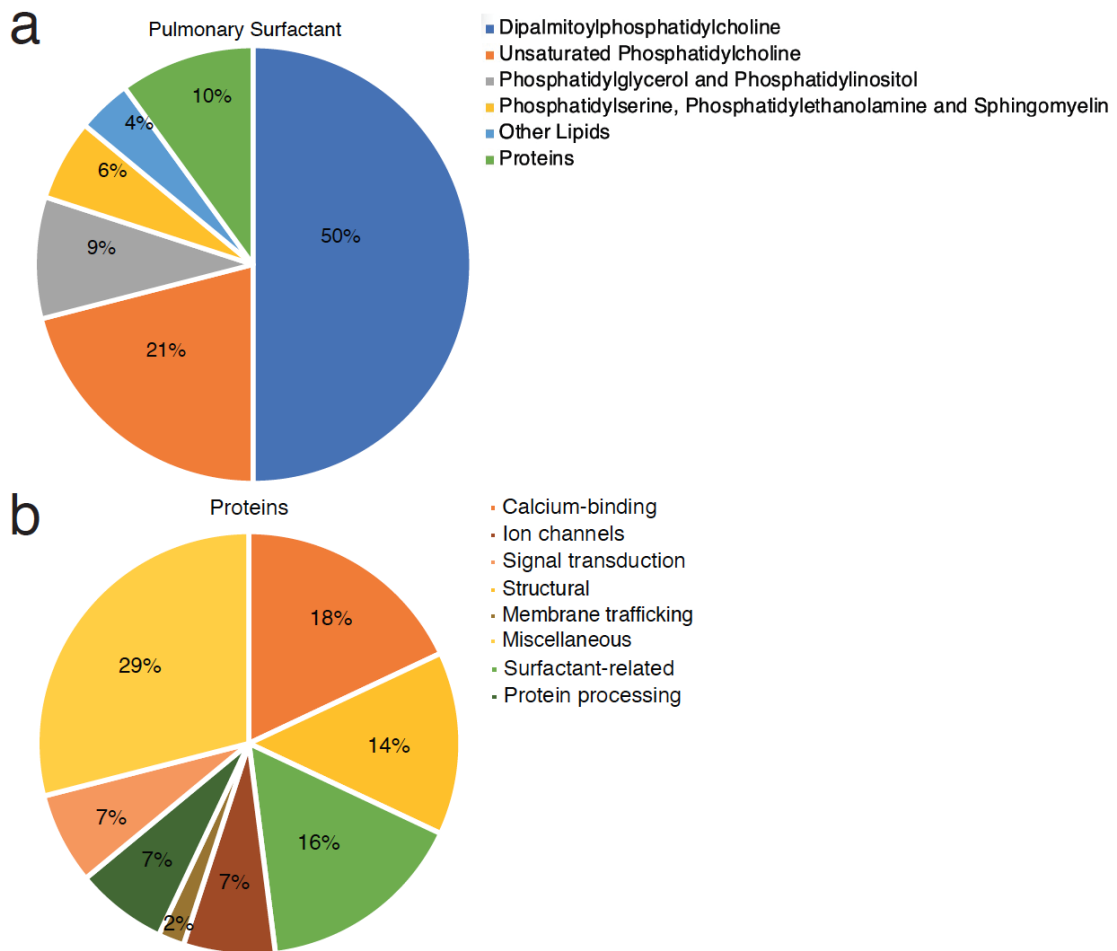
Figure 7. Pulmonary surfactant composition. (**a**) Pie chart illustrating the percentage of the lipid and protein components of pulmonary surfactant (**b**) Pie chart showing the percentage of the main protein categories identified in a proteomic analysis of rat lamellar bodies. Source: Agassandian & Mallampalli, 2013 and Wang et al., 2008.

1.3.2.2. Secretion of lung LBs

Secretion of pulmonary surfactant can be initiated through physiological or chemical stimuli. The primary physiological stimulus is the mechanical stretching of the alveoli occurring during inspiration. It has been proposed that the ATI cells are the sensors of this event, which would in turn stimulate ATII cells in a paracrine way, via ATP release [62]. This signal causes an increase in the intracellular concentration of Ca $^{2+}$ in ATII cells [63], which induces the fusion of LBs with the plasma membrane and eventually

the surfactant release in the alveolar space [64]. Other physiological or pharmacological agents like purinergic agonists (ATP and UTP), cholera toxin, or forskolin can stimulate surfactant release through activation of protein kinase A (PKA), or C (PKC), or of Ca2+/calmodulin-dependent protein kinase (CaMK) [65]. The secretion of LB contents is a slow procedure that can be initiated within seconds to minutes and can last up to 1h [66].

1.3.2.3. Clearance of pulmonary surfactant

Pulmonary surfactant forms a lipid layer in the alveolar space which is eventually cleared by resident immune cells and by ATII cells. Specifically, SP-A stimulates the uptake of lipids from isolated ATII cells and alveolar macrophages *in vitro* [67,68]. Furthermore, an *in vivo* study in rabbits described that the lipid uptake from ATII cells reaches more than 60% of total surfactant lipid clearance, whereas alveolar macrophages contribute to it at only 20% [69]. Interestingly, upon lung injury, the abundance of surfactant components in the alveolar space changes. In a model of acute lung injury that was induced through the intratracheal administration of lipopolysaccharide (LPS), an increase of macrophages and neutrophils in the alveolar space contributes to surfactant clearance [70]. Hence there is a synergistic mechanism for pulmonary surfactant recycling and clearance involving both the ATII cells and immune cells such as the alveolar macrophages and neutrophils.

1.3.2.4. Diseases linked to malfunction of LBs

Alterations in lamellar bodies or the surfactant component synthesis can be the consequences of mutations in *ABCA3* or *SP-B*. These lead to a malformation or complete absence of normal LBs and an altered lipid surfactant composition that results in respiratory failure of newborns after birth [71,72]. Furthermore, mutations of proteins important for the lysosome formation or the trafficking of selective cargos from the Golgi apparatus to lysosomes can result in defective formation and secretion of LBs. Hermansky Pudlak syndrome (HPS) is characterized by mutations in Adaptor Protein *(AP)-3* or the Biogenesis of Lysosome related Organelles Complex (BLOC)-1 to −3 (*BLOC1, BLOC2, BLOC-3*) which are involved in cargo trafficking and lysosome

formation respectively [73]. Patients with HPS have an accumulation of giant lamellar bodies in their ATII cells, associated with a defective secretion [74]. Hence, regulation of LB and lysosome synthesis, trafficking, and formation of the TM in the alveoli play important roles in normal ATII-cell physiology and normal lung function.

1.4. Leucine-rich repeat kinase 2 (Lrrk2)

Leucine-rich repeat kinase 2 (Lrrk2) is a large 286-kDa multi-domain protein that belongs to the Roco, a family of GTPases characterized by the presence of a central ROC-COR domain (Ras of complex proteins/C-terminal of Roc) [75,76]. Lrrk2 consists of seven structural domains: armadillo repeat motif (ARM), ankyrin repeat (ANK), leucine-rich repeat (LRR), Ras-of-Complex (ROC), C-terminal of ROC (COR), kinase (KIN), and WD40 domains. Lrrk2 can hydrolyze ATP and GTP through the KIN and ROC domains respectively, whereas the ARM, ANK, LRR, and WD40 are implicated in protein-protein interactions.

The closest homolog of Lrrk2 is the Leucine-rich repeat kinase 1 (Lrrk1), with which they share almost identical domain structure [77] (Figure 8a). The gene expression levels of *Lrrk2* and *Lrrk1* have been analyzed in both neonatal and adult mouse tissues. The results showed the highest *Lrrk2* expression in kidneys, lungs, and lymph nodes, whereas the highest *Lrrk1* expression was found in lymph nodes, stomach, and heart in adult mice [78] (Figure 8b, c).
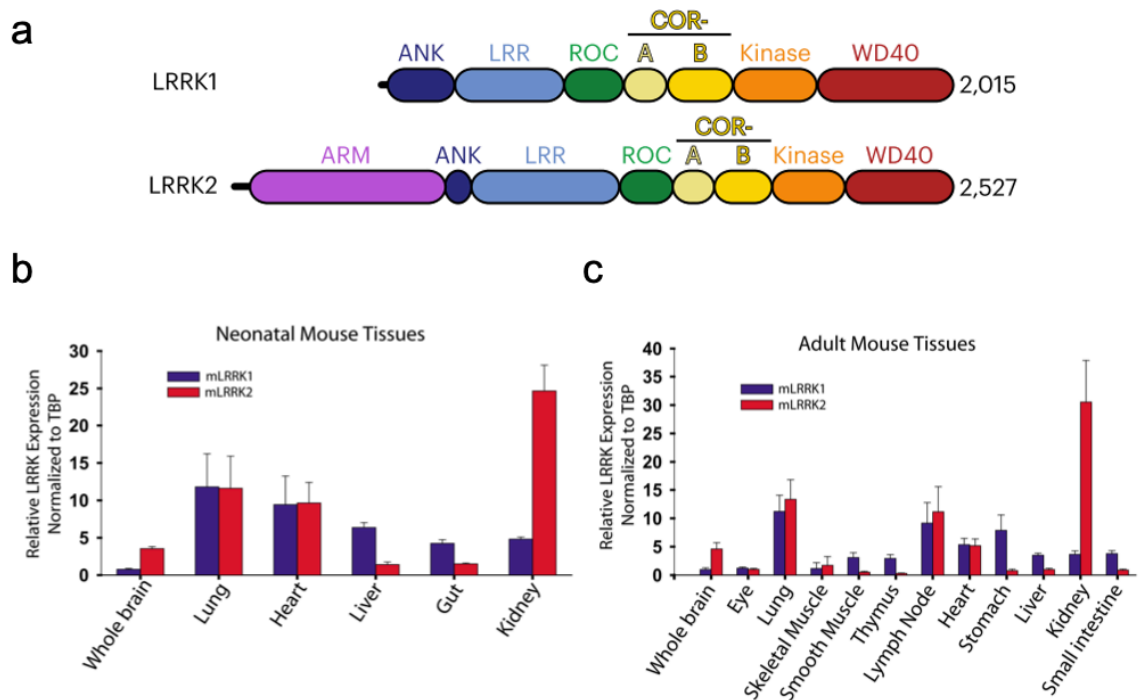
Figure 8. *Lrrk1* and *Lrrk2* mRNA levels in neonatal and adult mouse tissues. (**a**) Scheme showing the domain similarity of LRRK1 and LRRK2 proteins (**b**) Box plot illustrating the relative expression of *Lrrk1* and *Lrrk2* in neonatal mouse tissues and (**c**) in adult mouse tissues. The relative expression of each of those two genes was normalized to the TBP (*TATA*-binding protein). Source: Reimen et al., 2023, Biskup et al, 2007.

1.4.1. LRRK2 structure

The structures of full-length human LRRK2 and of a construct comprising its ROC-COR-Kinase-WD40 domains (LRRK2RCKW) have recently been determined by cryo-EM analysis [79]. In addition, recent analysis by cryo-electron tomography revealed the structure of microtubule-bound full-length LRRK2 within cells [80].

LRRK2 has both a kinase and a GTPase hydrolysis activity and belongs to the tyrosine kinase-like kinase (TKL). Unlike other tyrosine kinases (TK), TKLs lack the TK-specific motifs. LRRK2 exists in two conformations, the open and closed conformation for the inactive and active state. The KIN domain of LRRK2 is surrounded by the ANK, LRR, ROC, COR, and WD40 domains (Figure 9). The LRR domain wraps around much of the KIN domain, thereby hindering access of the latter to ATP. In addition, this interaction with the KIN domain stabilizes an enzymatically inactive open conformation

of LRRK2 [77]. The ROC and COR domains are also in close proximity to the KIN domain. Mutations in the ROC-COR domain altering their conformation thus may result in the misplacement of the KIN domain, eventually altering the kinase activity of the enzyme. LRRK2 exists as a monomeric protein but can homodimerize in cells. This homodimerization is suggested to occur between the COR domains of two LRRK2 monomers, and specifically by the COR-B subdomain [77,81]. The transition between a dimeric and monomeric state is regulated by the GTP turnover [82]. Finally, Myasnikov et al. showed that the so-called hinge helix between the first and the second LRR forms a bridge between the ARM and WD40 domains [77]. Pathogenic mutations that block this interaction enable the WD40 domain to instead dimerize with itself. Dimerization of the WD40 domain in turn has been proposed to mediate the formation of pathogenic LRRK2 filaments [77,83].
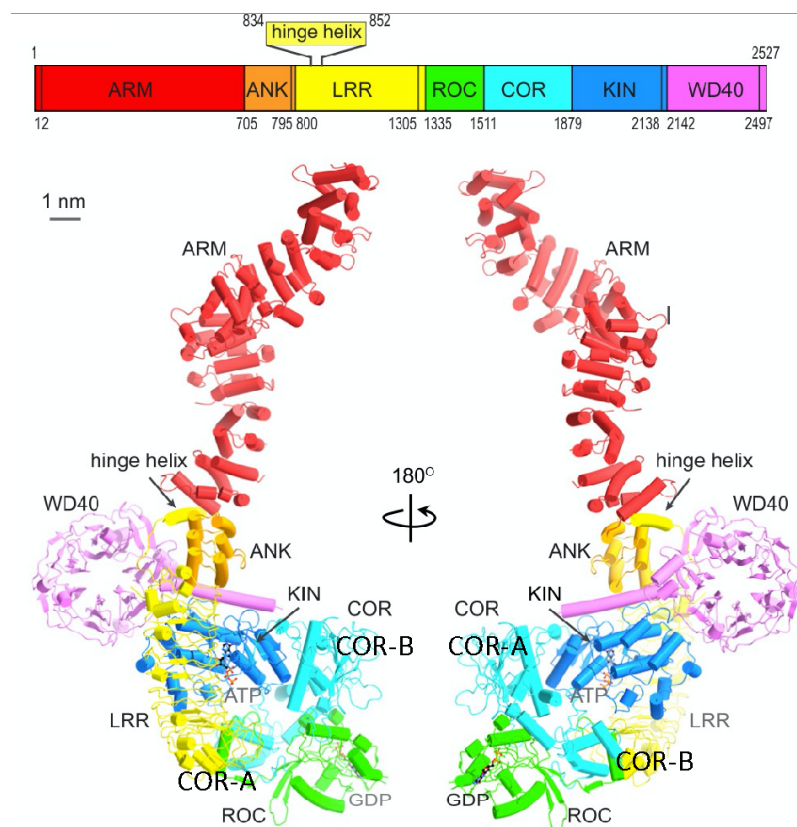
Figure 9. The human LRRK2 structure. Top scheme: the seven functional domains of human LRRK2. The 3D structure (below) of human LRRK2 domains at two views. ARM, armadillo repeats; ANK, ankyrin repeats; LRR, leucine-rich repeats; ROC, Ras-of-Complex; COR, C-terminal of ROC; KIN, kinase domain; and WD40 repeats are colored in red, orange, yellow, green, cyan, blue, and violet, respectively. Source: Myasnikov et al, 2021.

1.4.2. LRRK2 in Parkinson's disease

Autosomal dominant mutations in *LRRK2* have been linked and associated with familial and sporadic forms of Parkinson's disease (PD). More than 100 missense and nonsense mutations have been reported in *LRRK2*, but only a few have been proven to be pathogenic [84], including: *2019S, R1441C/G/H, Y1699C, S1761R,* and *I2020T*. Interestingly these known pathogenic *LRRK2* mutations are clustered in the ROC-COR and KIN domains, and most of them have been shown to result in an enhanced kinase activity of the enzyme [85,86]. The *G2019S* has been identified in up to 42% of familial cases and consists of the most common and well-studied *LRRK2* PD-linked mutation. On the contrary, R1441C *LRRK2* mutation is located in the ROC-COR domain and leads not only to an increase in the LRRK2 kinase activity but also to a decrease in the rate of GTP hydrolysis, with no change in the GTP binding efficiency [87,88].

LRRK2 is implicated in many biological processes including lysosomal homeostasis, autophagy, vesicle trafficking, and lipid metabolism [89,90]. The altered kinase activity of the enzyme drives an altered activation of downstream substrates, like the Rab GTPases (RAB10 and RAB12), affecting in this way downstream signaling pathways [91,92,93].

1.4.3. LRRK2 phosphorylation

LRRK2 is a highly phosphorylated protein, as was shown by phosphosite mapping via mass spectrometry, in which at least 74 phosphorylation sites were identified [94,95]. Those phosphorylation sites include mainly serines (59%), threonines (37%), and tyrosines (4%). They cluster between the ANK and the LRR domain at serines S860, S910, S935, S955, S973, and S976. S935 and S910 have been widely studied and their phosphorylation positively correlates with the LRRK2 kinase activity. Interestingly 60% of the phosphosites are autophosphorylation sites [93-96]. An example is S1292, which has been shown to be phosphorylated in the gain-of-function *LRRK2* mutants (N1437H, R1441C/G/H, Y1699C, G2019S, and I2020T) [97,98].

1.4.4. Regulation of LRRK2 expression and degradation

1.4.4.1. Transcriptional and post-transcriptional regulation of LRRK2 mRNA levels

The *LRRK2* gene is located on chromosome 12 and computational transcription factor search (PROMO- an online tool) in this gene revealed three transcription factor specificity protein 1 (SP1) binding sites [99]. SP1 is a transcription factor that is ubiquitously expressed in cells and is involved in cell growth, cell differentiation, and prevention of the CpG island methylation [100,101]. It can bind to *GC*-box and *GT/CACCC*-box, and in the *LRRK2* promoter, three SP1 binding sites with the following sequences; *GGGCGGTGC*, *CGTCCGCCCG*, and *GGGGCGGGGA*, were identified [98,102]. Overexpression of *SP1* in HEK293 cells, upregulated the mRNA and protein levels of LRRK2, whereas siRNA of *SP1* significantly decreased the *LRRK2* expression in these cells [99].

Furthermore, it was described that the *LRRK2* mRNA can be post-transcriptionally regulated by miRNAs and RNA-binding proteins, like Pumilio 1 (PUM1) and Pumilio 2 (PUM2) [103,104]. PUM proteins bind to RNA at *AU*-rich sequences called Pumilio Response Elements (PREs) and in humans, the optimal PRE motif is *UGUA(A/U)AUA* [105]. PREs are mainly located at the 3' untranslated regions (UTR) of the target mRNAs and their presence is a strong predictor of a PUM protein target [103,106]. Analysis of the 3' UTR sequences of human *LRRK2* identified 9 PREs. Knockdown (KD) of *PUM1* and *PUM2* using a mix of siRNAs targeting both proteins increased the *LRRK2* expression. By contrast, KD of *PUM2* alone, did not mimic that effect, suggesting that *LRRK2* mRNA is mainly regulated by PUM1 and not by PUM2. With the use of the prediction tool miRanda, 448 miRNAs were identified to target *LRRK2* and 233 for *PUM1.* Interestingly, in the human neuroblastoma cell line SH-SY5Y, *PUM1* and *LRRK2* share 5 miRNAs; miR-205-5p, miR- 181a-5p, miR-181b-5p, miR-181d-5p, and miR-186-5p, which are predicted to bind the 3' UTR sequence of human *LRRK2.* This observation made the authors suggest that those 5 miRNAs, could either regulate simultaneously the translation of both *PUM1* and *LRRK2* mRNAs or have a repressive

role on the *LRRK2* mRNA translation, that is complementary to the one of PUM1[101-103].

1.4.4.2. LRRK2 splice variants

The human *LRRK2* gene contains 51 exons. The full-length *LRRK2* mRNA is the predominant one, but at least five shorter protein-coding transcripts have been identified [107,108]. Giesert et al. described three splicing isoforms also in mice, including the full-length mRNA, an isoform that lacks only exon 5 but otherwise shares the same protein sequence and a third isoform that lacks 19 exons and terminates in an alternative exon, the exon 42a. Interestingly, PCR analysis on RNA samples from different mouse tissues (brain, lung, spleen, liver, heart) and primary neuronal, microglia, and astrocyte cell cultures revealed that the *Lrrk2* variant lacking exon 5 may represent the main isoform since it was present in all the tissues and cell types tested and particularly abundant in astrocytes. By contrast, the full-length *Lrrk2* transcript was barely visible in an agarose gel of any other cell type. PCR for the second alternative variant in brain, lung, kidney, heart samples as well as primary neuronal, microglial, and astrocytic cell cultures, showed that it was present in all cells and tissues but microglial cells [107].

In another study, 10 human brain regions from 134 healthy individuals were analyzed by microarray for *LRRK2* gene expression and revealed the existence of multiple mRNA transcripts, with the occipital cortex (OCTX) and the substantia nigra (SN) having the highest number of alternative splicing events [109,110]. Three main *LRRK2* splice variants were analyzed; the first one lacks exons 32–33 in the ROC-COR domain, the second one lacks exons 42–43 in the KIN domain and the third one lacks exons 48–50 in the WD40 domain. The absence of exons 32-33 was suggested to alter the inherent flexibility of the COR domain, which normally plays a role in the dimerization of the enzyme, whereas the truncation of exons 42–43 leads to the complete abolishment of the kinase activity of LRRK2 [106].

Overall, it is clear that there are multiple *LRRK2* variants in different tissues and cell types. Depending on the missing exons, this can affect different functional domains of the enzyme, and in the worst-case scenario abolish completely its activity.

1.4.4.3. Regulation of LRRK2 degradation

LRRK2 protein can be degradated by both the ubiquitin-proteasome system (UPS) and the chaperone-mediated autophagy (CMA) (Figure 10). The UPS involves the attachment of the 76-residue ubiquitin protein to the targeted protein as a post-translational modification via a sequential reaction that involves three enzymes : an Ub-activating enzyme (E1), an Ub-conjugating enzyme (E2), and an Ub ligase (E3) [111]. E1 binds to the ubiquitin molecule in an ATP-dependent manner and transfers it to E2, while E3 catalyzes the transfer of the ubiquitin molecules from E2 to the targeted proteins. The resulting polyubiquitination, targets the substrate for degradation by the 26S proteasome [112]. Heat shock protein 70 (Hsp70)-interacting protein (CHIP), which functions as an E3 ubiquitin ligase, binds directly to the ROC domain of LRRK2 and indirectly to its ARM domain via the Heat shock protein 90 (Hsp90). Co-immunoprecipitation experiments showed that these interactions are not altered in G2019S, R1441C, and D1994A LRRK2 mutants. Then the association of CHIP to LRRK2 drives the ubiquitination of the protein for proteasomal degradation. On the contrary, Hsp90 blocks that CHIP-mediated LRRK2 degradation through its binding to the LRRK2 ARM domain, and stabilization of the LRRK2 protein [113,114]. Hence, the interactions and proportions of Hsp90 and CHIP in the cells could affect the LRRK2 degradation by the proteasome.

The CMA pathway starts with the binding of the heat shock cognate 70 kDa protein (Hsc70) to a recognition motif (KFERQ) of the target protein. This protein complex binds to the lysosome-associated membrane protein type 2A (LAMP-2A) in lysosomes. LAMP-2A in turn multimerizes to form the translocation complex which regulates the uptake of the target protein for lysosomal degradation [115,116]. LRRK2 contains eight putative CMA recognition motifs and is partially degraded by CMA. Interestingly, high levels of LRRK2 can inhibit the formation of the CMA translocation complex, thereby leading to impaired degradation of other CMA-substrates like a-

synuclein in neuronal cells. Analysis of the degradation of the LRRK2 mutants G2019S and R1441C, showed that they associated less strongly with the lysosomal LAMP-2A. Consequently, they were less efficiently internalized and degraded in lysosomes compared to the controls. Finally, the LRRK2's association with the lysosomal membrane increased upon the presence of other CMA-substrates in both LRRK2 wild-type and G2019S / R1441C mutant cells [87].

In summary, while LRRK2 can be degraded by at least two known protein degradation pathways, impaired clearance via CMA can significantly stabilize some of the mutant LRRK2 variants found in PD patients compared to the wild-type.
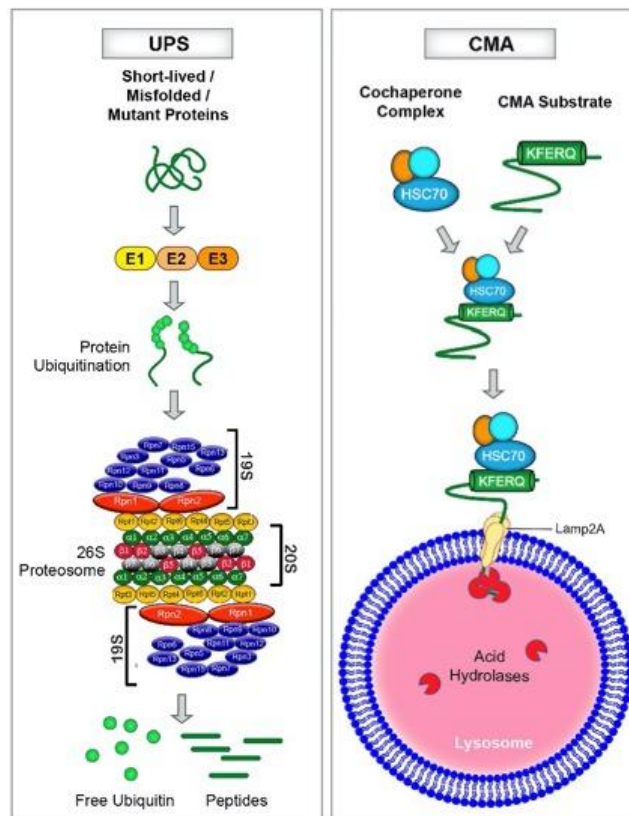
Figure 10. Two pathways of protein degradation. The left panel illustrates the Ubiquitin Proteasome System (UPS) which involves three enzymes, E1, E2, and E3 to target proteins and transfer ubiquitin molecules to them. Those molecules are then recognized by the 26S proteasome complex that degrades the tagged protein. The right panel shows the Chaperon-Mediated Autophagy pathway, which involves the co-chaperone complex Hsc70 for motif recognition of target proteins, and the lysosomal receptor LAMP2A mediating their delivery to lysosomes for degradation.. Source: Ghosh, 2020.

1.4.5. LRRK2 inhibitors

The increase in the kinase activity of several known PD-associated LRRK2 variants led to the development of kinase inhibitors as a potential therapy for PD patients. There are two main classes of kinase inhibitors, type I and type II. The type I inhibitors bind to the kinase domain of the LRRK2 in its closed conformation, when the enzyme is active, whereas type II inibitors maintain the kinase domain open in an inactive state. Type I inhibitors are more potent and efficient in inhibiting Lrrk2 kinase activity [117].

Commercially available type I inhibitors that are widely used *in vitro* include LRRK2-IN-1, GSK2578215A and MLi-2. Among these, LRRK2-IN-1 that demonstrated the greatest affinity for both wild-type and G2019S mutant LRRK2, with IC50 values of 13 nM and 6 nM respectively. LRRK2-IN-1 emerged as a potentially selective LRRK2 inhibitor from a screen of 300 compounds. However, it also showed a significant affinity for 12 other kinases and was unable to induce the dephosphorylation of S910 and S935 sites in LRRK2 in the brain [118]. GSK2578215A is a more selective LRRK2 inhibitor. With an IC50 of 10.9 and 8.9 nM for the wild-type and G2019S LRRK2 and it still showed high affinity for LRRK2, but it targeted only 3 additional kinases of a total of 308 potential off-targets examined. Similarly to the LRRK2-IN-1, though, it did not inhibit the phosphorylation of S910 and S935 LRRK2 in the brain [119]. MLi-2 demonstrates over 295-fold selectivity for LRRK2 over 308 other kinases and can block the phosphorylation of S935 LRRK2 in the brain. However, it did not affect the motor phenotype of the disease, hence failing to reduce striatal dopamine levels [120]. Finally, a molecule PF-06685360 (PFE-360) that has been recently developed by Pfizer, can penetrate the blood-brain barrier and has an IC50 of 2.3 nM. This compound is currently in preclinical trials. Other kinase inhibitory molecules are also currently in or entering soon to clinical trials, with the most promising molecule being BIIB122 (DNL151), currently evaluated in Phase III clinical trials [121] (Table 1).

In addition to small molecule kinase inhibitors, antisense oligonucleotides (ASOs) have also been developed. ASOs are short sequences of 10 to 20 base pairs, selectively targeting mRNA expression through principles like degradation via ribonuclease H or inhibition of pre-mRNA splice sites. ASOs are administered through

a single injection to the brain [122, 123]. BIIB094, which belongs to that category of drugs, is currently tested in a Phase I clinical trial (Table 1) [119].

Table 1. Lrrk2 inhibitors in development. Source: Katie Kingwell et al., 2023.

Drug	Company	Properties	Status
BIIB122 (DNL151)	Biogen/Denali	Small-molecule kinase inhibitor	Phase III and II
BIIB094 (ION859)	Biogen/Ionis	Antisense oligonucleotide	Phase I
S221237	Servier/Oncodesign	Small-molecule kinase inhibitor	Phase I to start
NEU-723	Neuron23	Small-molecule kinase inhibitor	Phase I to start
PFE-360	Cerevel/Pfizer	Small-molecule kinase inhibitor	Preclinical
ESB5070	Escape Bio	G2019S-selective small-molecule kinase inhibitor	Preclinical
Undisclosed	Merck & Co.	Small-molecule kinase inhibitor	Undisclosed

1.5. Role of mouse Lrrk2 in normal lung physiology

The role of Lrrk2 in normal lung physiology has been mainly studied in *Lrrk2* knock-out (KO) animals or in the context of Lrrk2 kinase inhibition as a candidate therapy for PD. *Lrrk2* KO mice and rats showed an increase in the number and size of lamellar bodies, while vacuolation and enlargement of ATII cells were apparent by light microscopy [124,125]. This was also observed in the ATII cells of macaques after treatment with MLi-2[126]. Furthermore, stimulation of ATII cells from *Lrrk2* KO rats with ATP *in vitro* led to an increase in LB fusion with the cell membrane and a decrease in the phospholipid contents [122]. These observations point to a role for Lrrk2 in LB homeostasis. Finally, mice expressing a kinase-dead variant showed no Lrrk2 morphological changes in the lungs, but the levels of full length Lrrk2 were slightly decreased, implying the kinase activity of Lrrk2 is important for its stabilization [125].

Chapter 2 - Aim

Lung cancer is the leading cause of cancer-related deaths worldwide, with the most common cancer type being the lung adenocarcinoma (LUAD). Activating mutations in *KRAS* and loss of function alterations in *TP53* are among the most frequent genetic alterations in LUADs. The poor life expectancy after diagnosis and the aggressiveness of the disease highlight the need for new pharmacological targets.

This work aimed to elucidate the role of LRRK2 in lung adenocarcinoma. First, I assessed the *LRRK2* expression in human lung adenocarcinomas. Then, I evaluated whether the PD-linked R1441C *Lrrk2* mutant that leads to a hyperactive kinase activity of the enzyme will cause a delay in lung tumor development in mice. Finally, I explored the morphological changes in R1441C *Lrrk2* mutant alveolar type II cells.

I started by monitoring the expression levels of *LRRK2* in lung adenocarcinoma patients using public data from the human Cancer Genome Atlas (TCGA) database. Then, since the *LRRK2* expression was shown to positively correlate with a better patient outcome of LUAD patients *in silico,* we decided to cross mice that harbor the PD-linked R1441C *Lrrk2* mutation to *Kras* $^{G12D/WT}$*; Tp53* $^{fl/fl}$ (KP) mice to generate the *Kras* $^{G12D/WT}$*; Tp53* $^{fl/fl}$*; Lrkk2* $^{R1441C/WT}$ (KPL) mouse model. These animals were used for the assessment of lung tumor development and characterization of their lesions. Furthermore, RNA-sequencing of KP and KPL cancer cells was performed for the exploration of pathways in which Lrrk2 is involved in lung cancer cells while generation of KP and KPL tumor-derived cell lines was used for the validation of signalling pathways *in vitro*. Assessment of the morphological and ultrastructural changes of ATII cells and LBs were finally performed in healthy Lrrk2 wild-type and R1441C mutant mice.

Chapter 3 - Results

3.1. Preliminary data for the Lamellar body (LB)-related genes in KP mice

3.1.1. LB-related genes are down-regulated in KP tumors

Previous work by the Meylan lab showed that deletion of the glucose transporter 1 (GLUT1) in KP mice decreased the proportion of advanced tumors that were characterized as adenocarcinomas, even without altering the tumor growth rate [127]. Furthermore, in the same study, it was the first time to be shown in this model that lung cancer cells harbor lamellar-body like organelles (LBOs). LBOs accumulate ^{13}C-biomass upon ^{13}C-glucose injection in tumor-bearing KP and, to a lesser extent, in KPG1 mice [127].

To further characterize KP and KPG1 cancer cells and the differences between them, we compared their transcriptomes by RNA sequencing. We focused on CD45-negative sorted cells, which consist mainly but not exclusively of cancer cells. Interestingly, among the top 60 downregulated genes in KP versus KPG1 cells, we found no less than six genes that are known to be involved in the physiology of LBs (Figure 11). Specifically, from the list of the top sixty downregulated genes in KP versus KPG1 cancer cells, six LB-related genes were present: *Lamp-3*, *Sftpc*, *Slc34A2*, *Abca-3*, *Lrrk2,* and *Lpcat1*. This finding made us hypothesize that the KP tumors, which were more advanced than KPG1, attenuate the lamellar body program during tumor progression.
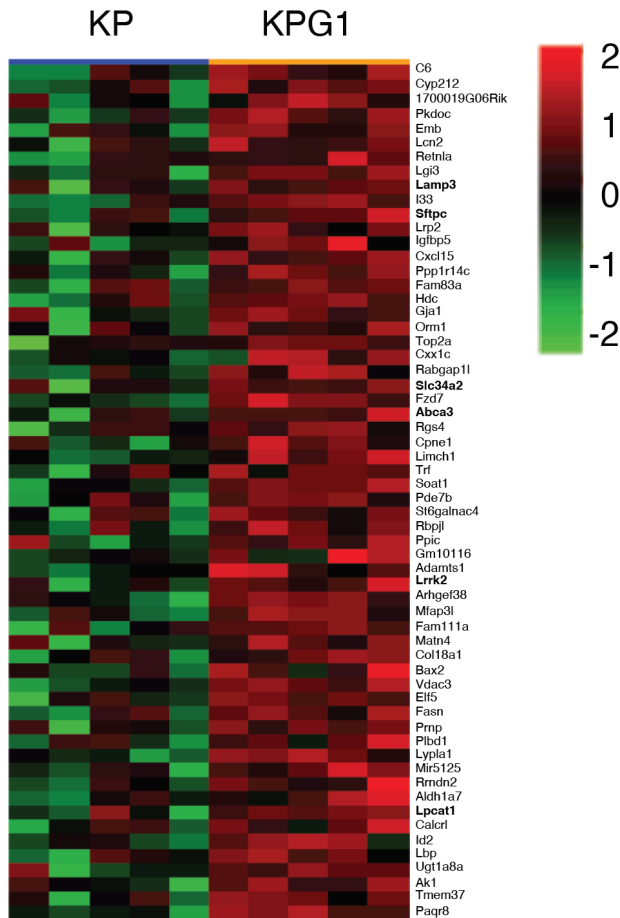
Figure 11. LB-related genes are downregulated in KP compared to KPG1 tumor cells. Heatmap showing the top 60 downregulated genes in KP versus KPG1 cancer cells from the Hallmark gene set. p-value: 2.10-3 by permutation test. The lamellar body genes are in bold. Color legend: black: median expression, red: above the median, green: below the median for each gene. Data was obtained with Dr. C.Contat and bioinformatic analysis was performed by Dr.N.Zangger.

3.2. Expression of LB-related genes in human lung adenocarcinoma

3.2.1. High expression of LB-related genes correlates with better overall survival of LUAD patients

To assess the importance of LB-related genes in lung adenocarcinoma (LUAD), we first monitored their expression levels in lung adenocarcinoma patients using public data from the human Cancer Genome Atlas (TCGA) database. After defining the median expression levels for each of the LB-related genes (*LAMP-3*, *SFTPC*, *SLC34A2*, *ABCA-3*, *LRRK2*, *LPCAT1*), two groups per gene were distinguished; the high- and low- expressing groups. All values were then normalized to the total number of samples per group and their estimated overall survival was plotted. Interestingly, Kaplan-Meier plots revealed that high expression of all of the LB-related genes examined correlated with a better overall survival of LUAD patients (Figure 12a). Furthermore, pairwise analysis revealed that the expression levels of all of these LB-

related genes strongly correlated with one another, as expected if they function in a shared regulatory program (Figure 12b). Finally, we explored the regulatory elements of the promoter regions of the LB-related genes to identify a common transcription factor that may regulate their expression. For such an analysis, we used the JASPAR database which contains 519 binding sites from vertebrates. Only the top eleven transcription factors that were common among the six genes were plotted (Figure 12c). The top predicted transcription factor was ZNF263, followed by RREB1, EGR1 and SP1. A literature search indicated that SP1 regulates the expression of *Lrrk2* [99]. However, no other LB-related genes are known to be regulated by SP1 or by any of the other candidate regulatory factors identified here. Overall, these results show that the expression levels of *LAMP-3*, *SFTPC*, *SLC34A2*, *ABCA-3*, *LRRK2,* and *LPCAT1* in human LUAD cells strongly correlate with one another and thus are likely regulated by one or several shared transcription factors. Most importantly, high expression of any of these LB-related genes correlates with a better prognosis for LUAD patients.
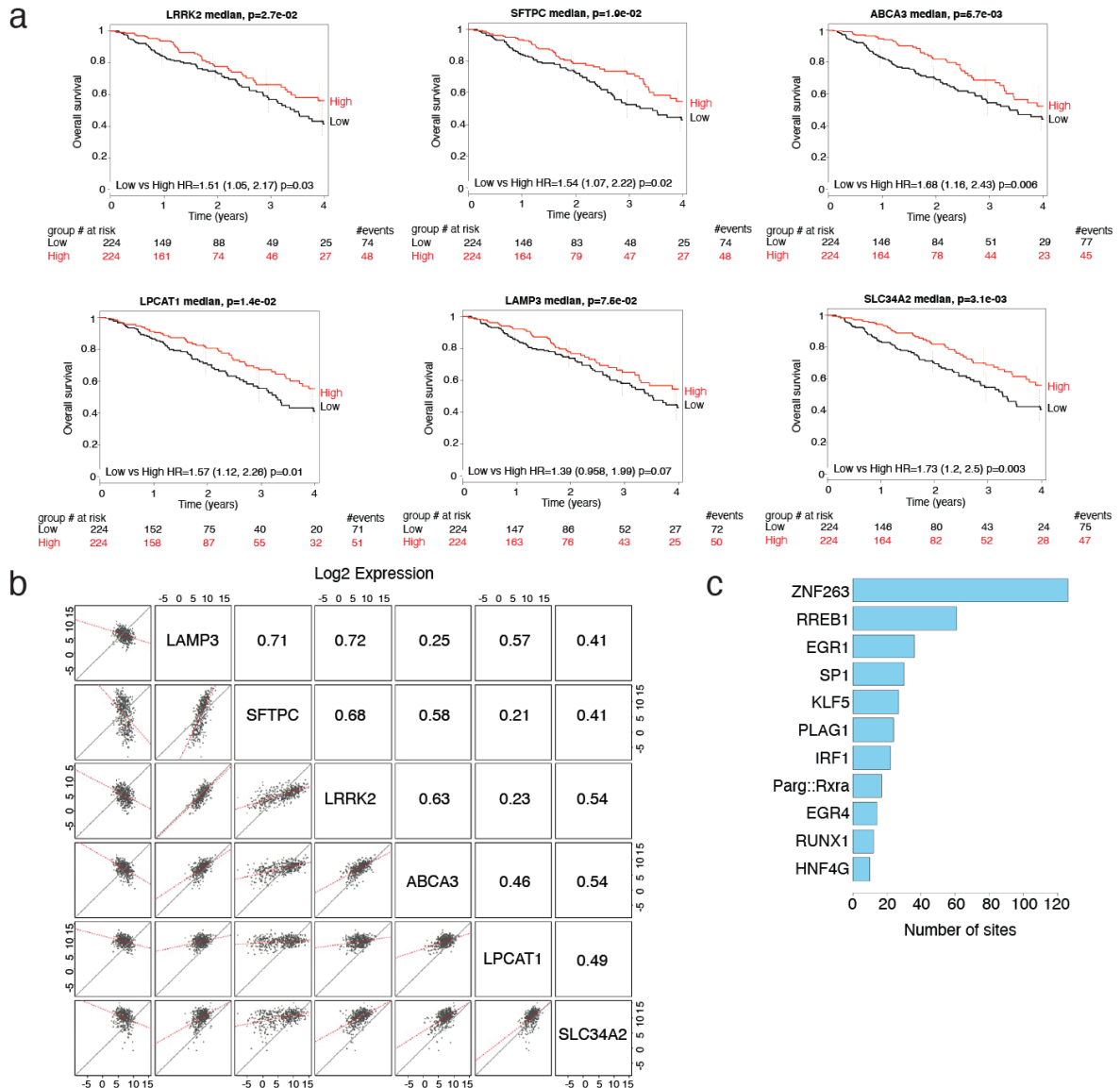
Figure 12. Survival analysis of 448 human lung adenocarcinoma samples based on the LB-gene-related expression. (a) Median LB-related gene expression value splits down the samples into low- and high-expressing groups. Kaplan-Meier plots show the overall survival for each LB-related gene. p-values were computed with the Wald test (**b**) Pairwise correlation of LB-related genes (*LAMP-3*, *SFTPC*, *SLC34A2*, *ABCA-3*, *LRRK2* and *LPCAT1*) (**c**) Plot showing the top eleven transcription factors based on computational analysis of the promoter region of the six LB-related genes (*LAMP-3*, *SFTPC*, *SLC34A2*, *ABCA-3*, *LRRK2,* and *LPCAT1*). Data was obtained in collaboration with the bioinformatician Dr. N. Zangger.

3.2.2. *LRRK2* expression in human lung adenocarcinoma

Among the six LB-related genes analyzed here, *LRRK2* most attracted our attention.

Besides the correlation of its mRNA expression levels with a better patient outcome (Figure 12a), Lrrrk2 protein plays a role in lung LB homeostasis. However, the exact functions and mechanisms of *Lrrk2* in normal lung physiology and in lung cancer cells are unknown. Furthermore, *LRRK2* mutations have been linked with Parkinson's disease (PD). Thus, some transgenic mouse models that harbor *LRRK2* point PD mutations have been developed and the role of the protein has been widely studied in neurons. Therefore, the preliminary results we obtained from the analysis of the TCGA LUAD data, the prior knowledge on the function of *LRRK2* in neuronal cells, and the existence of transgenic mouse models that could facilitate its investigation, made us decide to further continue our study on Lrrk2.

First, we analyzed gene expression differences between the *LRRK2* low- versus high-expressing groups. We found that these groups are characterized by a differential gene expression profile (Figure 13a), with the *LRRK2* high-expressing group being enriched in gene sets that are involved in the lamellar body program and surfactant metabolism (Figure 13b). These results and the positive correlation of *LRRK2* with the other LB-related genes (Figure 12b) suggest that *LRRK2* is co-regulated with LB genes, which are important for the normal physiology of ATII cells. We also found that the *LRRK2* high-group shows a lower representation of genes found in mTORC1 signaling and glycolysis gene sets (Figure 13b), two pathways that are enriched in the lung tumor cells [127,128,129]. Hence, those results validate that the *LRRK2* high- group recapitulates more the normal ATII cell physiology rather than the cancer-related phenotype.

If *LRRK2* functions as a tumor suppressor, one might expect it to be mutated at elevated frequency among lung cancer patients. To test this prediction, we analyzed the status of *LRRK2* mutations and their frequency among LUAD patients in the TCGA database. We found that LRRK2 was indeed mutated in up to 5% of 448 LUAD patients, with 12 different mutations to be identified. Ten of them were missense, one silent, and one frame-shifting splice site, five of which were localized in the ROC-COR and KIN catalytic domains (Figure 13c).

We then assessed the expression of LRRK2 in LUAD patients at different tumor stages. To bin tumors into four different stages, we considered tumor sizes (T-stage),

the extent of lymph node metastasis (N-stage), and the metastatic spread to other organs (M-stage). Each of these parameters was subdivided into subcategories. Among T-stages, T1, T2, and T3 denote tumors between 2-3cm, 3-7cm or bigger than 7cm, respectively, whereas even larger tumors that expand into other structures were classified as T4. Among N-stage, N0 to include patients with no lymph node metastasis and N3 to group patients with lymph node metastasis on the opposite side of the affected lung. Finally, M-stage (M0, M1a, M1b) defines the spread of cancer cells into other organs, with M0-stage patients not having metastasized cells and M1b having cancer cells that are spread to distant parts of the body, like the liver or bones. All these parameters considered, we found a downregulation of *LRRK2* when the tumors are advanced, big, and metastatic (TNM stage 4) (Figure 13d). These results indicate that *LRRK2* expression levels gradually decrease during tumor progression.

a   100 top fold changes up and down DEGs

b
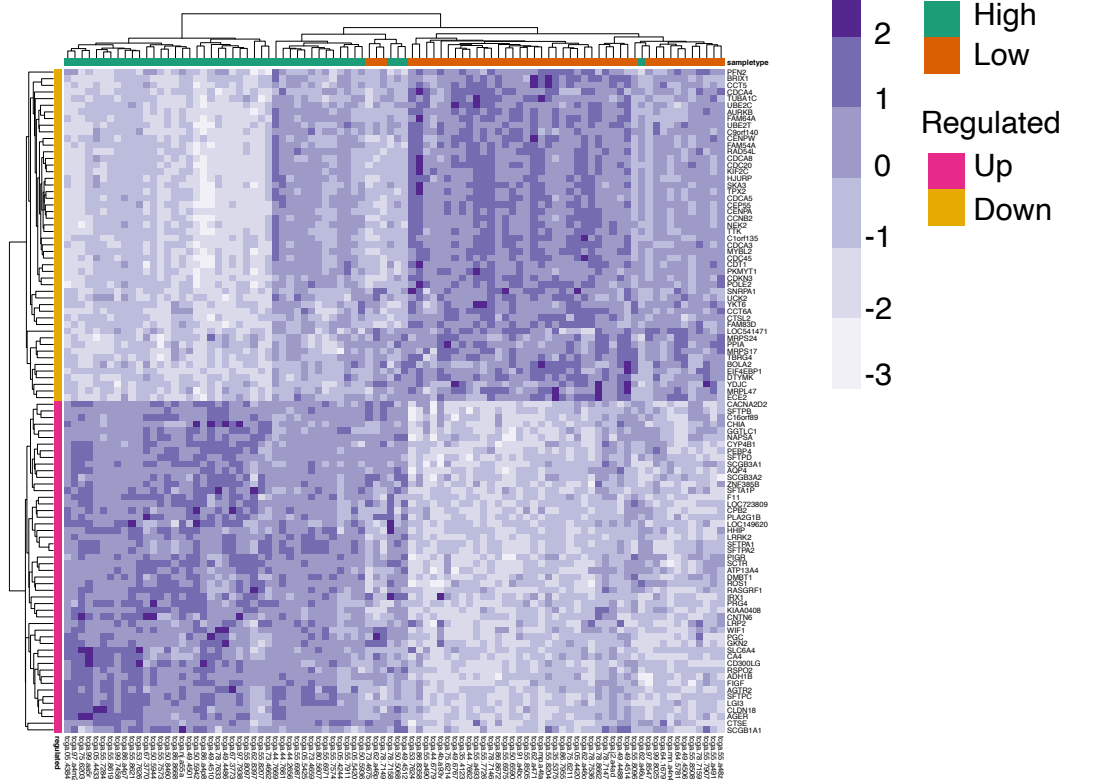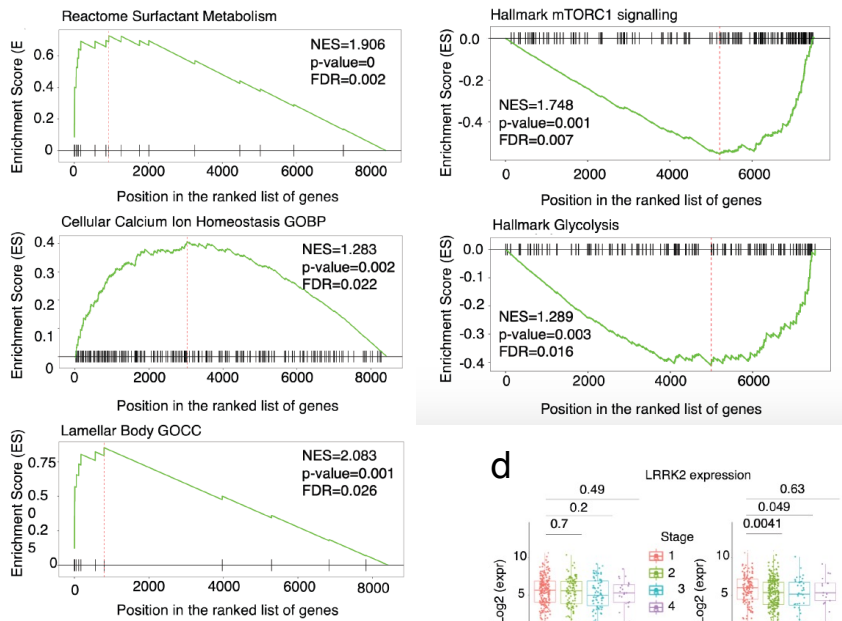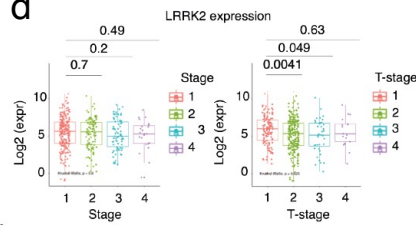
c

Protein Change	Mutation Classification	Domain
p.L121L	Silent	ARM
p.L2500V	Missesnce	WD40
p.G1116	Splice site	LRR
p.D1549N	Missesnce	COR
p.S966F	Missesnce	ANK
p.G1589E	Missesnce	COR
p.S764C	Missesnce	ANK
p.W1602C	Missesnce	COR
p.R960W	Missesnce	ANK
p.Y2023C	Missesnce	KIN
p.L44P	Missesnce	ARM
p.E1399D	Missesnce	COR

d

Figure 13. Differential transcriptional profile of human *LRRK2* high versus *LRRK2* low lung tumor samples. (**a**) Heatmap showing the top 100 differentially expressed genes in high- and low-*LRRK2* groups. Each gene is represented by a single row and each expressing group is in columns. Color legend: light purple: median expression, dark purple: above median expression, white: below median expression, green: *LRRK2* high- expressing group, orange: *LRRK2* low- expressing group, pink: upregulated genes, yellow: downregulated genes. p-value: 2.10-3 by permutation test (**b**) Gene set enrichment analysis (GSEA) plots of the selected activated and repressed gene sets. The enrichment score is plotted across the list of genes ranked by their correlation to *LRRK2* expression. The normalized enrichment scores (NES), p-values, and their false discovery rate (FDR) adjusted values were rounded off to three decimal digits (**c**) Table showing the type of mutations and the amino acid-induced alteration of LRRK2 in human LUAD samples. Data was obtained and bioinformatically analyzed by the master's student Catia Forsell and by the bioinformatician Dr. N. Zangger (**d**). Strip-chart of the mean *LRRK2* expression by TNM- or T-stages. For each sub-stage, the black point range shows the average *log2 LRRK2* expression ± standard deviation (S.D.). p-values were computed with Kruskal-Walli's test with a cutoff of 0.05.

3.2.3. Overexpression of *LRRK2* in human non-small cell lung cancer (NSCLC) cell lines induces apoptotic cell death

To further investigate the role of LRRK2 in lung cancer, I analyzed its expression in a panel of human NSCLC cell lines (H441, A549, Calu6, H1944, H1975) by western blot. As a positive control, I transfected an *LRRK2-GFP* expression plasmid into the easily transfectable cell line; 293T cells. As shown in Figure 14a, the expression of endogenous *LRRK2* varied considerably among the NSCLC cell lines examined, with the highest levels being observed in A549 and H441 cells, whereas in Calu6 and H1975 cells, LRRK2 expression was below detection.

Based on these observations, I decided to overexpress *LRRK2-GFP* in two cell lines that highly express LRRK2 (A549, H441 cells) and in one that does not (H1975 cells). As a positive control for the transfection, I used the 293T cells and as a control plasmid, a *GFP*-expressing construct. Forty-eight hours post-transfection, I collected the cells, stained them with Annexin-V and DAPI, and the proportions of apoptotic, necrotic, and alive cells were assessed by flow cytometry (Figure 14b). Interestingly, overexpression

of *LRRK2* in A549, H441, and H1975 cells resulted in an increased proportion of apoptotic cells when compared to the control *GFP*-transfected cells (Figure 14b). On the contrary, apoptosis was not triggered in the *LRRK2-GFP* or *GFP*-transfected 293T cells (Figure 14b), indicating that the cellular toxicity of overexpressed LRRK2 was specific to the human NSCLC cell lines. Additionally, in all the cell lines of the GFP negative fraction, most of the cells both in the *LRRK2-GFP* and *GFP*-control condition were necrotic (Figure 14b), demonstrating that *LRRK2-GFP* positive cells became apoptotic due to the overexpression of *LRRK2* and not due to un-specific toxicity of transient transfection.

To validate the induction of NSCLC cell death upon *LRRK2* overexpression, I repeated the transfection of the same plasmids in A549 cells that had been plated before on coverslips and stained for the apoptotic marker, cleaved caspase-3, and DAPI. As shown in Figure 14c, more *LRRK2-GFP* than *GFP* transfected cells were positive for cleaved caspase-3. Overall, these results suggest that overexpression of *LRRK2* in human NSCLC cell lines induces their apoptotic cell death, in line with our hypothesis that LRRK2 expression in lung adenocarcinoma cells may have a tumor suppressive function.
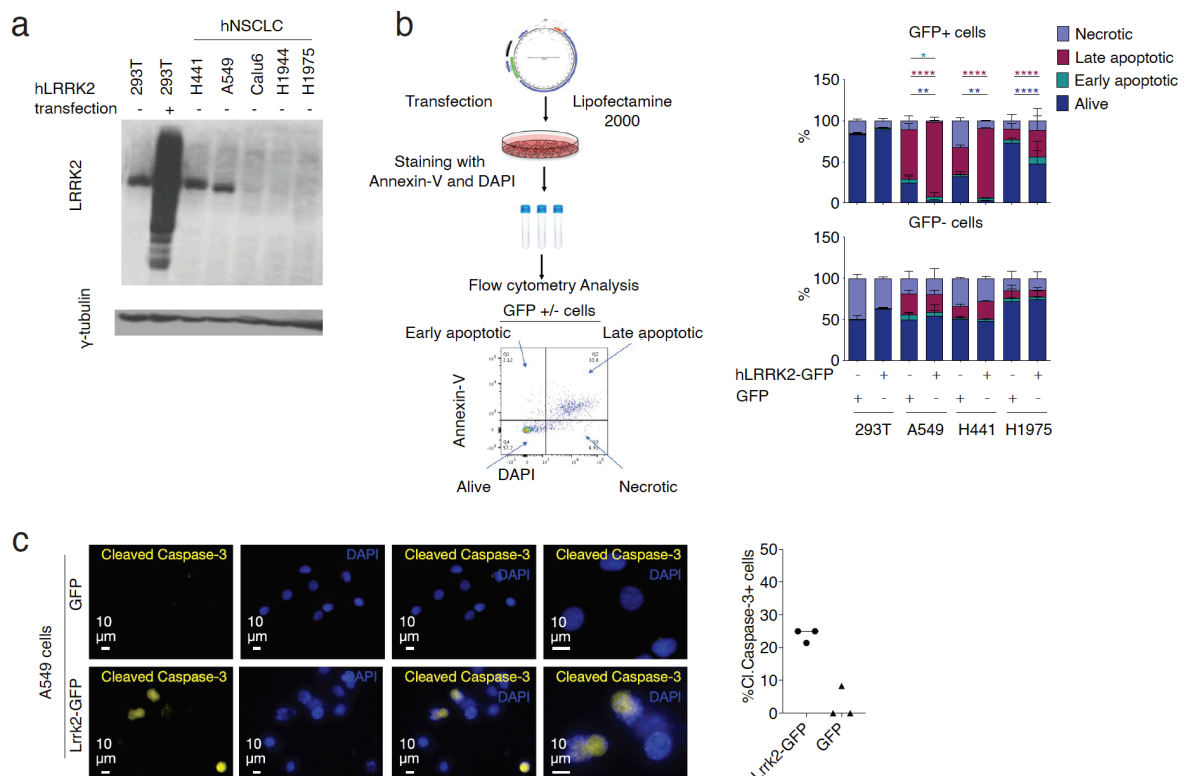
Figure 14. Cell death induction of human NSCLC cell lines upon *LRRK2* overexpression. (a) Western blot analysis of endogenous Lrrk2 and γ-tubulin in extracts of 293T, H441, A549, Calu6, H1944, or H1975 cells. Where indicated, 293T cells were transiently transfected with *LRRK2-GFP* 48 hours before analysis. (**b**) Scheme illustrating the workflow of the transfection and staining of 293T, H441, A549, and H1975 cells. Flow cytometric quantification of apoptotic, necrotic cells, or live cells of the indicated cell lines 48 hours after transfection with *GFP* control or *LRRK2-GFP* plasmids. Two-way ANOVA was used for the statistical analysis. (**c**) Representative example of a cleaved caspase-3 (cCasp3) and DAPI immunofluorescence (IF) staining of A549 cells transfected with *LRRK2-GFP* or *GFP* control. Dot plot illustrating the percentage of Cleaved caspase-3+ cells that were quantified in three different pictures for *LRRK2-GFP* and *GFP* control plasmid transfected cells (n=30 and 20 cells analyzed respectively). Scale bar: 10 *μ*m.

3.3. Characterization of healthy KPL lungs

To directly test if *Lrrk2* has a tumor-suppressive function in lung adenocarcinoma, we decided to use a mouse model that harbors the PD-linked R1441C *Lrrk2* mutation, which increases the kinase activity of the enzyme [88]. Although that mutation was not detected in LUAD patients (Figure 13c), we considered that the above-the-baseline levels Lrrk2 activity in mutant cells might reduce the lung tumor growth and hence it is relevant for the aim of this work. Considering that, we crossed KP mice with Lrkk2 $^{R1441C/WT}$ knock-in mice (L) to generate the *Kras* $^{LSL-G12D/WT}$*; Tp53* $^{fl/fl}$*; Lrkk2* $^{R1441C/WT \, or}$ $^{R1441C/ \, R1441C}$ (KPL$^{mut/wt \, or \, mut/mut}$) mouse model. Before generating KPL mice in sufficient numbers to initiate tumors, I tested in a pilot study if the presence of one or two copies of *Lrkk2* ^{R1441C} might alter the expression levels and localization of Lrrk2 or the morphology or function of ATII cells in healthy lungs of KPL compared to KP mice prior to the onset of tumorigenesis.

3.3.1. Expression and localization of Lrrk2 in healthy KPL lungs

To assess the expression of endogenous wild-type Lrrk2 in the different lung cell types, cryosections of healthy mouse lungs, cell-type specific markers and Lrrk2 were labeled by indirect immunofluorescent staining. As shown in figures 15a-d, all of the cell types examined expressed *Lrrk2,* including alveolar type II (ATII) cells marked by pro-SPC co-staining, alveolar type I cells (Podoplanin+), immune cells (CD45+) and

endothelial cells (CD31+). The highest Lrrk2 staining intensity was observed in the ATII and immune cells. In good agreement, strong expression of Lrrk2 has previously been described in ATII and CD45+ cells; neutrophils, monocytes, macrophages, T-cells B-memory, and a subset of dendritic cells [125,130,131].

Analysis at higher magnifications showed that Lrrk2 localized diffusely throughout the cytoplasm but with increased accumulation in pro-SPC-stained subregions (Figure 15e). Specifically, it was detected either around pro-SPC+ regions or co-localized with pro-SPC. Lrrk2 has been shown to play a role in vesicular trafficking, and its localization at the lysosome and exosome membrane has been described before [132,133,134]. Our present finding that Lrrk2 staining in ATII cells co-localized with pro-SPC indicates that it is enriched on LBs. To see if this localization pattern in LBs changes when Lrrk2 is mutated, I stained healthy Lrrk2 wild-type (KP) and mutant (KPL[mut/wt or mut/mut]) lung cryosections with Lrrk2, pro-SPC and DAPI. I observed no difference in the localization of these two proteins in Lrrk2 wild-type (KP) and mutant (KPL[mut/wt or mut/mut]) ATII cells (Figure 15e).
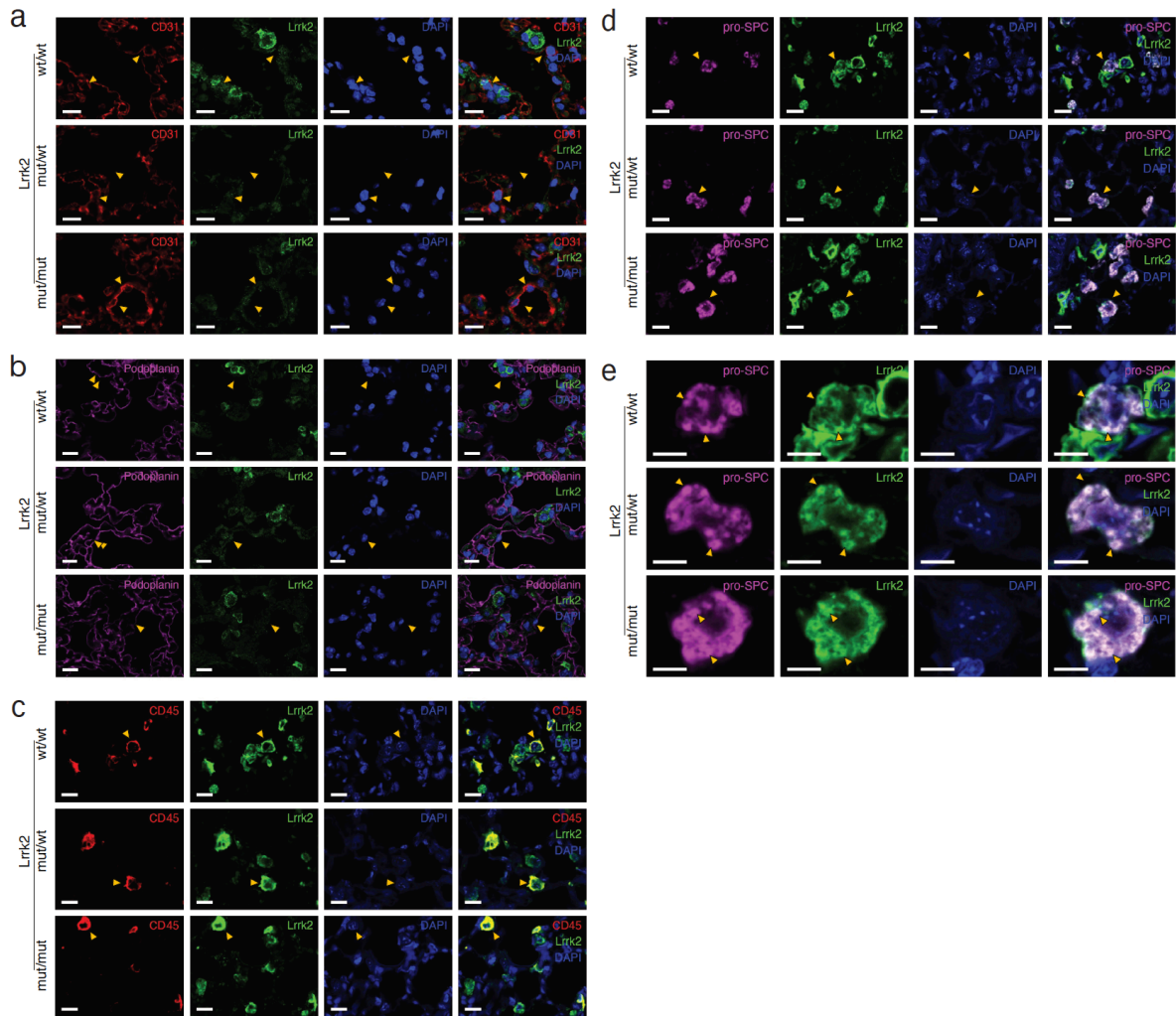
Figure 15. Co-localization of Lrrk2 with the LB-marker pro-SPC in Lrrk2 wild-type and mutant ATII cells. (**a**) Representative images of Lrrk2, CD31, and DAPI immunofluorescence (IF) staining of Lrrk2 wild-type and mutant healthy lung sections. Yellow arrowheads point to the localization of Lrrk2 in CD31+ cells. Scale bar: 10 μm. (**b**) Representative example of Lrrk2, Podoplanin, and DAPI immunofluorescence (IF) staining of Lrrk2 wild-type and mutant healthy lung sections. Yellow arrowheads point to the localization of Lrrk2 in Podoplanin+ cells. Scale bar: 10 μm. (**c**) Representative example of Lrrk2, CD45, and DAPI immunofluorescence (IF) staining of Lrrk2 wild-type and mutant healthy lung sections. Yellow arrowheads point to the localization of Lrrk2 in CD45+ cells. Scale bar: 10 μm. (**d**) Representative example of a Lrrk2, pro-SPC, and DAPI immunofluorescence (IF) staining of Lrrk2 wild-type and mutant healthy lung sections. Yellow arrowheads point to the localization of Lrrk2 in pro-SPC+ areas.Scale bar: 10 μm. (**e**) Representative example of a higher magnification of Lrrk2, pro-SPC, and DAPI immunofluorescence (IF) staining of Lrrk2 wild-type and mutant healthy lung sections. Yellow arrowheads point to the (co-)localization of Lrrk2 with pro-SPC. Scale bar: 5 μm.

3.3.2. Morphological characterization of healthy KPL lungs

Next, I asked if the presence of one or two R1441C mutant *Lrrk2* alleles alters the morphology of ATII cells or their LBs. Analysis at the time of sacrifice of healthy animals revealed no significant changes in the weights of either the lung or spleen of KP, KPL^mut/wt or KPL^mut/mut mice (Figure 16a). To visualize cell morphologies, paraffin sections of healthy KP, KPL^mut/wt and KPL^mut/mut lungs were stained using hematoxylin and eosin (H&E). Analysis of the size and shape of ATII cells by a certified pathologist revealed no histopathological changes in the ATII cells of Lrrk2 mutant lungs compared to WT (Figure 16b). Abnormal enlargement and vacuolation of ATII cells had been previously described in in *Lrrk2* knock-*out* (KO) lungs [125,135].

To analyze the ultrastructural morphology of LBs, healthy KP, KPL^mut/wt and KPL^mut/mut lung sections were examined using electron microscopy. The normal dense multi-lamellar morphology of LBs showed no overt morphological change (Figure 16c). However, compared to wild-type, mutant cells appeared to abnormally accumulate lipid droplets (LDs) (Figure 16c). In an attempt to verify this apparent increase, whole lung sections from healthy *Lrrk2* wild-type and mutants were incubated with Oil Red O (ORO) to stain neutral lipids, and with Alcian blue as a nuclear counter staining. The quantification was performed using a script that detects the ORO+ vesicles and the nuclei and then normalizes the total number of lipid droplets to the number of nuclei detected. After quantifying the number of ORO+ vesicles per cell in whole lungs of three to four mice per genotype (KP, KPL^mut/wt or KPL^mut/mut), we saw no difference in the total number of LDs per cell between those three groups (Figure 16d). Given that this analysis was not specific to a certain cell type, we then decided to focus on ATII cells. To this end, cryosections of healthy lung mutant (KPL ^mut/wt) mice were stained for pro-SPC and ORO. The staining revealed no ORO+ vesicles in ATII cells, but in cells that were in close proximity (Figure 16e). To test if these ORO+ cells correspond to resident immune cells, I stained healthy mutant (KPL ^mut/wt) lungs for the immune cell marker CD45 and ORO. No co-localization was observed between these two markers (Figure 16f). Possibly, the cells which accumulated the ORO+ vesicles correspond to pulmonary lipofibroblasts which localize adjacent to ATII cells. Pulmonary lipofibroblasts are known to produce triglycerides and other neutral lipids for storage in lipid droplets. Then, they either transfer those lipids to ATII cells or they stimulate them for surfactant synthesis [136,137].

Overall, this first part of my thesis shows no visible alterations in the morphology, size, or shape of KPL^mut/wt or KPL^mut/mut ATII cells and LBs when compared to wild-type control. Quantification of LDs in whole lungs of the three different genotypes also showed no change in the total number of ORO+ vesicles per cell. Interestingly, the ORO+ vesicles were not localized in ATII cells, but in cells adjacent to them, which we presume are lipofibroblasts.
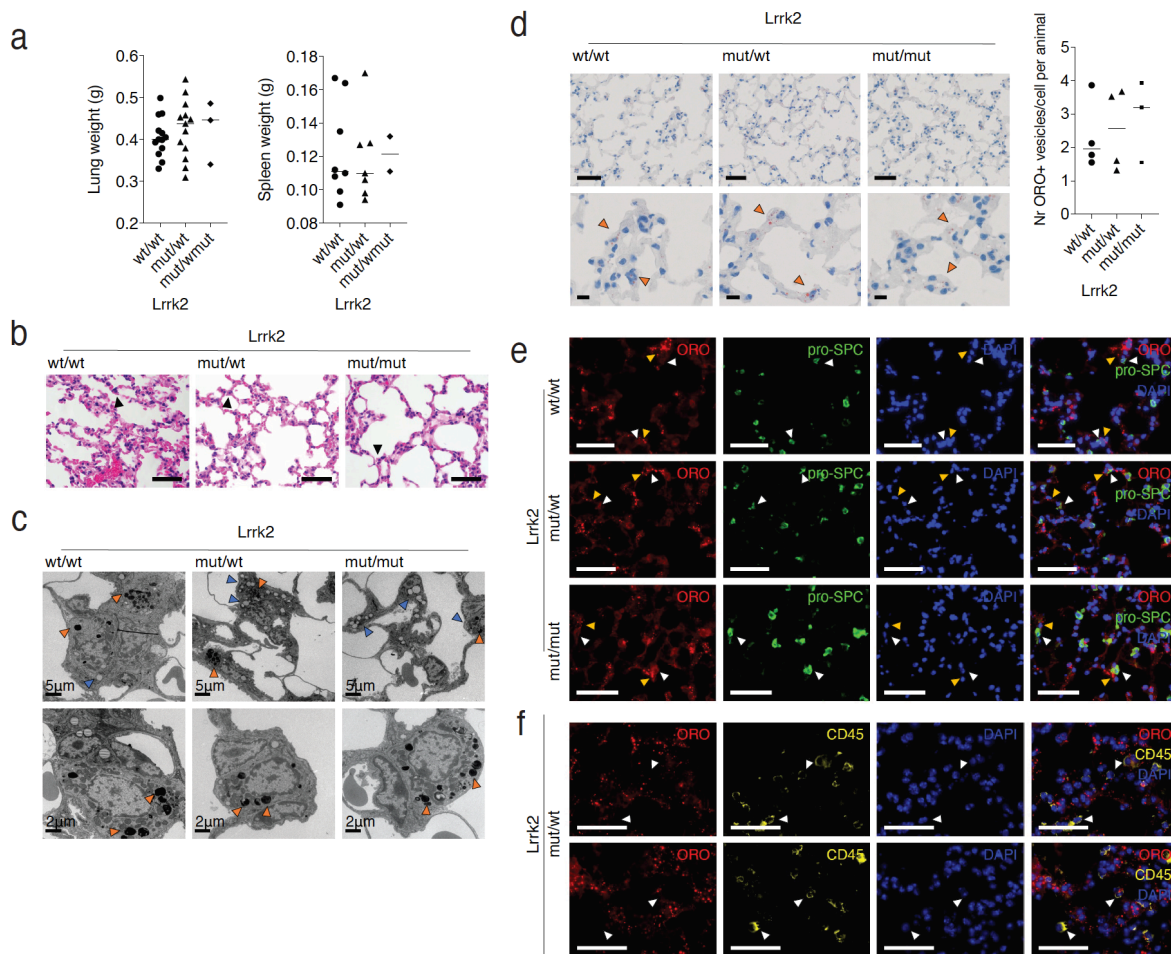
Figure 16. No morphological and ultrastructural differences in *Lrrk2* wild-type and mutant ATII cells. (a) Scatter plots with mean ± S.D. displaying healthy *Lrrk2* wild-type (KP) and mutant (KPL^mut/wt and KPL^mut/mut) lung and spleen weights (n = 12, 13, and 4 respectively) at sacrifice. Whitney test was used for statistical analysis. **(b)** Representative images of sections from healthy *Lrrk2* wild-type (KP) and mutant (KPL^mut/wt and KPL^mut/mut) lungs stained for H&E. Black arrowheads point to ATII cells. Scale bars: 50 *μ*m. Data obtained in collaboration with the certified veterinary pathologist C. Göpfert, EPFL, Switzerland **(c)** Representative transmission electron microscopy (TEM) micrographs from healthy *Lrrk2* wild-type (KP) and mutant (KPL^mut/wt and KPL^mut/mut) lungs showing the LBs in ATII cells and the

LD accumulation in mutant lung cells. Orange arrowheads point to LBs and blue arrowheads to LDs. Data were obtained in collaboration with the BioEM Facility, EPFL, Switzerland. (**d**) Representative images of healthy *Lrrk2* wild-type (KP) and mutant (KPL[mut/wt] and KPL[mut/mut]) lung sections stained for ORO and Alcian blue. Orange arrowheads point to ORO+ vesicles. Scale bar: 50 and 10 μm. Scatter plots with mean ± S.D. displaying the number of ORO+ vesicles per cell in healthy KP, KPL[mut/wt] and KPL [mut/mut] lungs sections (n = 4, 4 and 3 respectively). Mann-Whitney test revealed no significant changes. (**e**) Representative images of pro-SPC, ORO, and DAPI stainings in healthy KP, KPL[mut/wt,] and KPL[mut/mut] lungs sections. White arrow heads point to pro-SPC+ cells and yellow arrows to ORO+ cells that are adjacent to pro-SPC+ cells. Scale bar: 50 μm. (**f**) Representative images of CD45, ORO, and DAPI stainings in healthy KP, KPL[mut/wt,] and KPL[mut/mut] lungs sections. Scale bar: 50μm.

3.3.3. *In vivo* functionality of ATII cells in healthy lungs of KPL mice

Lrrk2 is known to play a role in LB homeostasis [125,138] and some *in vitro* assays with ATII cells isolated from *Lrrk2* KO and wild-type rats have been described [138]. In these assays, LBs from *Lrrk2* KO ATII cells were exocytosed faster *in vitro* upon ATP treatment and contained fewer phospholipids compared to wild-type cells. To test *in vivo* whether the exocytosis of LBs is also altered by the *Lrrk2* R1441C allele, I performed bronchoalveolar lavage (BAL) in healthy *Lrrk2* wild-type and R1441C mutant mice at sacrifice to collect fluids and to detect the SPC concentration. Since exocytosis of LBs is difficult to directly quantify *in vivo,* I instead used an ELISA kit to measure as a proxy the secretion of SPC. Although only a few KPL[mut/mut] mice were available for this analysis, KPL[mut/wt] and KPL[mut/mut] ATII cells appeared to regulate the LB exocytosis differently than their wild-type counterparts. In particular, there was a strong trend for a decreased SPC concentration in bronchoalveolar lavage fluids (BALF) of KPL[mut/wt] lungs compared to wild-type. By contrast, the KPL[mut/mut] cells showed a strong tendency to secrete higher concentrations of pro-SPC in their BALF, suggesting increased LB exocytosis by the homozygous mutant ATII cells compared to wild-type. However, neither of these trends reached statistical significance (Figure 17).
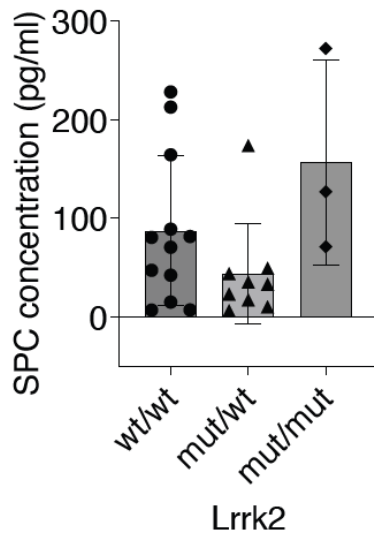
Figure 17. SPC concentration in BAL of *Lrrk2* wild-type and mutant ATII cells. Scatter plots with mean ± S.D. displaying the SPC concentration detected in the BALF of healthy *Lrrk2* wild-type (KP) and R1441C mutant (KPL$^{mut/wt}$ and KPL$^{mut/mut}$) mice (n = 12, 9 and 3 respectively) at sacrifice. Statistical test used, Mann-Whitney test.

3.4. Analysis of KPL tumors

Having characterized the morphological and functional consequences of R1441C *Lrrk2* mutation in healthy lungs, I next focused on the main aim of this project which was to investigate the role of Lrrk2 in lung adenocarcinoma.

3.4.1. Role of Lrrk2 in early KP tumor progression

The first approach was to assess if the R1441C mutant *Lrrk2* influences tumor initiation. To initiate tumorigenesis, KP and KPL$^{mut/wt}$ mice were intratracheally instilled with adenoviral vectors (Ad5.SPC-Cre viral vectors) which express the Cre recombinase. In KPs, Cre-*LoxP* recombinations activate oncogenic *KrasG12D* and concomitantly delete both *Tp53* alleles, specifically in SPC+ cells. By contrast, Lrrk2 is expected to be constitutively activated by the R1441C mutation at all times already before the onset of tumorigenesis. To evaluate the role of the enzyme in early-stage disease, mice were sacrificed twenty weeks post-tumor initiation, which is four weeks before the typical endpoint chosen by our laboratory for KP mice. The follow-up of the lung tumors by µCT revealed that the average tumor growth rates were similar in KP and KPL$^{mut/wt}$ mice (Figure 18a). To determine the advancement of the disease, whole tumor-bearing lung sections were stained for H&E and the tumor grades were assessed by the pathologist. Surprisingly, no differences in the tumor grades of the two genotypes were observed (Figure 18b). In parallel, the tumor number per animal

was counted, and again no differences were observed between the two groups (Figure 18c).

Before further analyzing the characteristics of the lesions, it was crucial to first assess the expression levels of *Lrrk2*. For that, whole tumor-bearing lung sections were stained for Lrrk2 and DAPI and the total fluorescence intensity of Lrrk2 per cell for each lesion was determined. As shown in figure 18d, the fluorescent intensity of Lrrk2 per cell was the same in KP and KPL$^{mut/wt}$ tumors. Given that the kinase activity of R1441C mutant Lrrk2 is increased [87,88] the phosphorylation of a known substrate, Rab10, at the T73 site was examined by immunofluorescent staining [92]. I observed no change in the fluorescence intensity of phospho-Rab10T73 per cell in KP versus KPL$^{mut/wt}$ lesions (Figure 18d). This could mean that immunostaining is not sufficiently quantitative to detect the expected increase, that the kinase activity of wild-type Lrrk2 is not rate-limiting for phosphorylating Rab10 on T73, or that increased phosphorylation may be compensated by a corresponding increase of de-phosphorylation.

Even though R1441C Lrrk2 induced no consistent changes in either the tumor growth rates or in tumor grades or in Rab10 phosphorylation, we explored whether it can influence the proliferative and/or apoptotic capacity of the tumor cells. To address this, whole lung sections of tumor-bearing KP and KPL$^{mut/wt}$ mice were indirectly stained for the proliferation marker Ki-67 or the apoptotic marker cleaved caspase-3. With the use of a script, we could detect the positively stained cells as well as the total number of nuclei of a defined area, in our case, each area corresponded to one individual tumor. Then, the proportions of single positive cells per lesion were determined. Interestingly, I found that while there were no differences in the proportions of proliferative cells, apoptotic cells were significantly increased in KPL versus KP tumors (Figure 18e). Altogether, the findings of this part demonstrate that the KP and KPL$^{mut/wt}$ tumors grew and advanced similarly, while the cancer cells were proliferating similarly but and dying more through apoptosis. We hypothesized that since most of the tumors had already progressed to adenocarcinomas (tumor grade 4) in both KP and KPL$^{mut/wt}$ mice, animals might have to be sacrificed at an even earlier time point to exclude a potential transient difference in tumor growth also at earlier stages (Grades 1-3).
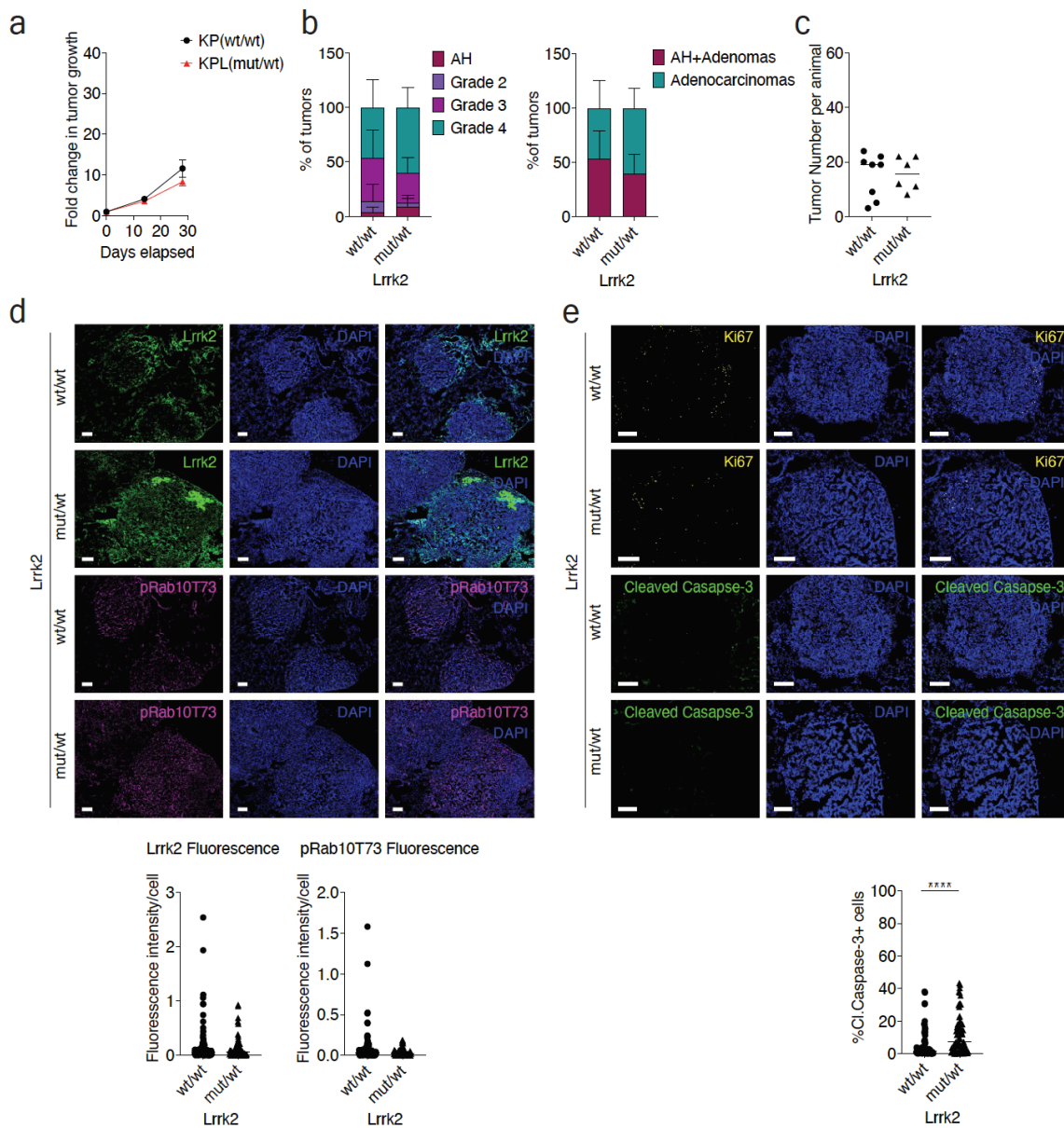
Figure 18. R1441C Lrrk2 mutation in KP tumors does not impact tumor progression 20 weeks post-tumor initiation. (**a**) Graph with mean ± S.E.M. indicating the fold changes of KP and KPL[mut/wt] tumor volumes (n =42 and 38 tumors, respectively) monitored by micro-computed tomography (*μ*CT), starting at 16 weeks post-tumor initiation with tumor volumes set to 1. Statistical test used, Mann-Whitney test. (**b**) Percentage of KP and KPL[mut/wt] lesions classified by tumor grades, from alveolar hyperplasia (AH) to grade 4. Data was obtained in collaboration with the certified veterinary pathologist C. Göpfert. (**c**) Scatter plot with mean ± S.D. showing the total number of KP and KPL[mut/wt] lesions per mouse (n =8 and 6 mice, respectively). Statistical test used, Mann-Whitney test. Data was obtained in collaboration with the certified veterinary pathologist C. Göpfert. (**d**) Representative images of whole tumor-bearing KP and KPL[mut/wt] lung sections stained for Lrrk2 and DAPI or phospho-RAB10 T73 and DAPI. Scale bar: 200 *μ*m. Scatter plots with mean ± S.D. displaying the fluorescence intensity of Lrrk2

per cell in each lesion. Statistical test used, Mann-Whitney test. (**e**) Representative images of whole lung sections from tumor-bearing KP and KPL$^{mut/wt}$ stained for Ki-67 and DAPI or Cleaved Caspase-3 and DAPI. Scale bar: 200 μm. Dot plots with mean ± S.D. displaying the proportions of Ki67+CD45- cells and Cleaved Caspase-3+ cells in each lesion. Statistical test used, Mann-Whitney test.

3.4.2. Role of Lrrk2 in advanced KP lesions

3.4.2.1. Analysis of tumor growth rates of advanced KP and KPL lesions at the endpoint

To evaluate the role of Lrrk2 in advanced tumors, mice were sacrificed at the endpoint between 23- to 24-weeks post-tumor initiation, depending on the health condition of the animals. Analysis of the μCT scans showed that the tumor growth rates of KP and KPL$^{mut/wt}$ mice were similar (Figure 19a), although two out of five cohorts showed significantly reduced tumor growth rates in KPL$^{mut/wt}$ compared to KPs (Figure 19g). Grading of all the lesions and analysis of their total numbers per animal revealed no differences between the three genotypes in either of these two cohorts individually (Figure 19b, c), or if they were pooled together (Figure 19h). Also, quantification of the area that is occupied by NSCLC as compared to the healthy lung compartment for the assessment of the tumor burden revealed no differences between the KP and KPL$^{mut/wt}$ mice (Figure 19d).

Since the KPL $^{mut/wt}$ and KPL $^{mut/mut}$ mice behaved similarly in terms of tumor growth, we decided to further focus our analysis on the heterozygous *Lrrk2* mutant animals. Similar to the aforementioned analyses at an earlier stage, the proliferative and apoptotic capacity of the tumor cells were assessed. Quantification of the fluorescent intensity of Lrrk2 per cell in all lesions showed that the KPL$^{mut/wt}$ tumors were more adept at maintaining the expression of *Lrrk2* compared to the KP ones (Figure 19e). This was also observed in the cohorts where the difference in tumor growth rate was significantly reduced (Figure 19i). However, the fluorescence intensity of phospho-Rab10T73 per cell was equivalent in KP and KPL$^{mut/wt}$ lesions (Figure 19e, i).

Immunostainings of tumor-bearing lung sections for Ki-67 and cleaved-caspase-3 surprisingly showed that the KPL$^{mut/wt}$ tumors were proliferating faster compared to the

controls whereas there were no differences in the proportion of apoptotic cells (Figure 19f). On the contrary, such an increase in proliferation was not found in the two cohorts where a decrease in tumor growth rates in mutant animals was observed (Figure 19j). Overall, the results of this part showed that although Lrrk2 protein levels were maintained more in advanced KPL$^{mut/wt}$ compared to KP tumors, the effect of the R1441C mutation was not always consistent and clear between the cohorts. Possibly, the average growth rate of KPL$^{mut/wt}$ tumors is diminished only at even earlier stages than the ones examined, and only transiently, followed by a phase where they catch up on the KP tumors. This hypothesis would be consistent with the paradoxical increase of the Ki-67 staining observed in some of the KPL tumor cohorts specifically at the endpoint. Analysis at an early time point before week 20 would be needed to further test this scenario.
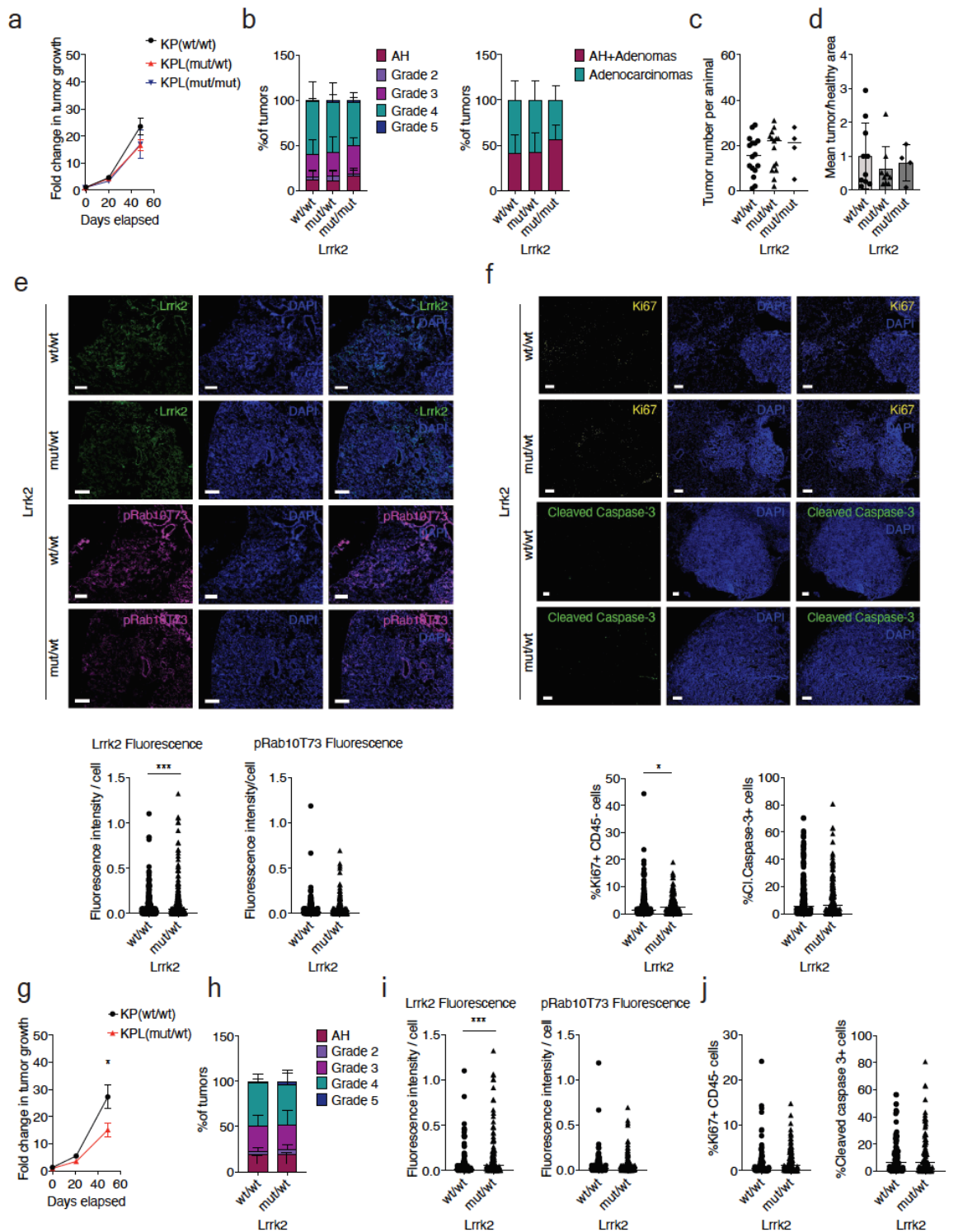
Figure 19. Lrrk2 R1441C mutation in KP tumors does not consistently slow tumor progression 24 weeks post-tumor initiation. (**a**) Graph with mean ± S.E.M. indicating the fold changes of KP, KPL^(mut/wt) and KPL^(mut/mut) tumor volumes (n = 71, 77 and 15 tumors, respectively) monitored by micro-

computed tomography (μCT), starting at 16 weeks post-tumor initiation, with tumor volumes set to 1. Statistical test used, Mann-Whitney test. (**b**) Percentage of KP and KPL[mut/wt] lesions classified by tumor grades, from alveolar hyperplasia (AH) to grade 4. Data was obtained in collaboration with the certified veterinary pathologist C. Göpfert. (**c**) Scatter plot with mean ± S.D. showing the total number of KP and KPL[mut/wt] lesions per mouse (n =16, 15, 4 mice respectively).Statistical test used, Mann-Whitney test. Data was obtained in collaboration with the certified veterinary pathologist C. Göpfert. (**d**) Scatter plot with mean ± S.D. showing the mean tumor burden of KP and KPL[mut/wt] mice (n=10, 9, 4 mice respectively). Statistical test used, Mann-Whitney test. Data was obtained in collaboration with the certified veterinary pathologist C. Göpfert. (**e**) Representative images of whole tumor-bearing KP and KPL[mut/wt] lung sections stained for Lrrk2 and DAPI or phospho-RAB10 T73 and DAPI in each individual lesion. Scale bar, 200 μm. Statistical test used, Mann-Whitney test. (**f**) Representative images of whole tumor-bearing KP and KPL[mut/wt] lung sections stained for Ki-67 and DAPI or Cleaved-caspase 3 and DAPI. Scale bar: 200 μm. Statistical test used, Mann-Whitney test. (**g**) Graph with mean ± S.E.M. indicating the fold changes of KP and KPL[mut/wt] and tumor volumes (n = 29 and 32 tumors, respectively) monitored by micro-computed tomography (μCT), starting at 16 weeks post-tumor initiation with tumor volumes set to 1. Statistical test used, Mann-Whitney test. (**h**) Percentage of KP and KPL[mut/wt] lesions classified by tumor grades, from alveolar hyperplasia (AH) to grade 4. Data was obtained in collaboration with the certified veterinary pathologist C. Göpfert. (**i**) Representative images of whole tumor-bearing KP and KPL[mut/wt] lung sections stained for Lrrk2 and DAPI or phosphor-RAB10 T73 and DAPI in each lesion. Scale bar: 200 μm. Statistical test used, Mann-Whitney test. (**j**) Representative images of whole tumor-bearing KP and KPL[mut/wt] lung sections stained for Ki-67 and DAPI or Cleaved-caspase 3 and DAPI. Scale bar: 200 μm. Statistical test used, Mann-Whitney test.

3.4.2.2. Advanced KPL lesions lose Lrrk2 expression during tumor progression

The Lrrk2 protein levels quantified by immunofluorescence in KP and KPL[mut/wt] tumors in the mice sacrificed at the endpoint made us wonder whether the *Lrrk2* expression is downregulated also in KPL tumors, similarly to what was observed initially in KP tumors (Figure 11). To address this, serial sections of whole tumor-bearing lung sections of KP and KPL[mut/wt] mice were stained for Lrrk2 and DAPI, or by H&E. In the final sections, the pathologist graded all tumors individually. In parallel, the fluorescent intensity of Lrrk2 per cell was quantified per lesion and binned by tumor grades. As shown in figure 20a, Lrrk2 protein levels are decreasing during disease progression, both in KP and KPL[mut/wt] tumors.

To extend our analysis to potentially subtle effects of the R1441C *Lrrk2* mutation on the cancer cell transcriptomes, we performed bulk RNA-sequencing analysis of FACS-sorted CD45-negative cells from KP, KPL^mut/wt and KPL^mut/mut. Each tumor was cut into two pieces so that one half was available for histological evaluation of the grade of the sequenced lesions. Most of the tumors were advanced (grade 4) in all groups (Figure 20b). Analysis of the *Lrrk2* gene expression levels in those lesions confirmed that *Lrrk2* is down-regulated during tumor progression in all three conditions. However, it was surprising to see that the *Lrrk2* expression was even more decreased in KPL^mut/wt compared to KP tumors. This downregulation contrasts the protein expression results in KPL^mut/wt tumors (Figure 19d), suggesting that there is either a differential degradation of the R1441C Lrrk2 protein or a differential mechanism of regulation of the mutant gene expression compared to the control.
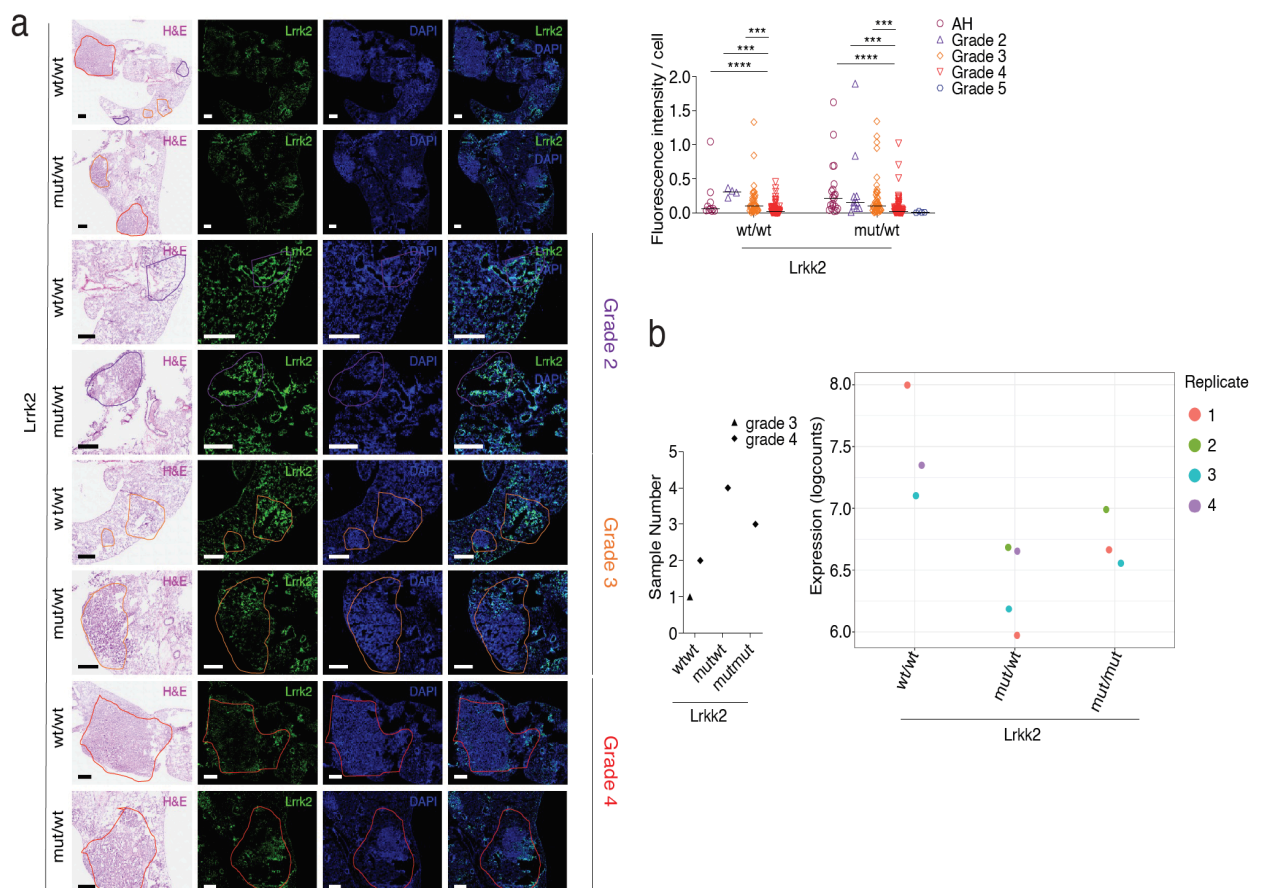
Figure 20. *Lrrk2* expression is down-regulated during KP and KPL ^mut/wt tumor progression.
(**a**) Representative images of whole tumor-bearing KP and KPL^mut/wt lung sections stained for H&E or Lrrk2 and DAPI. Single tumors have been annotated in different colors, each representing a tumor

grade. Purple: Grade 2, Orange: Grade 3, Red: Grade 4. Scale bar: 200μm. Statistical test used, Mann-Whitney test. Data were obtained in collaboration with the certified veterinary pathologist C. Göpfert. Scatter plot with mean ± S.D. showing the total number of KP and KPL$^{mut/wt}$ lesions per mouse (n =389 and 287 tumors analyzed respectively). Statistical test used, Mann-Whitney test. (**b**) Scatter plot showing the total number of KP, KPL$^{mut/wt}$ and KPL$^{mut/mut}$ lesions per grade. Dot plot showing Lrrk2 expression of each KP, KPL$^{mut/wt}$ and KPL$^{mut/mut}$ lesion that was used for RNA-sequencing. Bioinformatics analysis, courtesy of Dr. N. Zangger.

3.4.2.3. Analysis of tumor-infiltrating immune cells

In an attempt to explain why the R1441C mutant Lrrk2 slowed the average tumor growth rates in some but not all cohorts of KP and KPL$^{mut/wt}$ mice, we stained tumor-bearing lung sections for the immune cell marker CD45. This initial analysis of 193 and 216 KP and KPL$^{mut/wt}$ tumors respectively, indicated that the frequency of CD45+ cells per tumor might be increased in KPL$^{mut/wt}$ lesions compared to KP controls (Figure 21a). To characterize which immune cell types, if any, differentially infiltrate the tumors, we stained the main immune cell populations in dissociated KP and KPL$^{mut/wt}$ tumors and assessed the proportions of each by multi-color flow cytometry. The analysis revealed that although no differences in the total proportion of immune cells between the KP and KPL$^{mut/wt}$ tumors were observed, there was an increase in the proportion of natural killer cells in KPL$^{mut/wt}$ lesions (Figure 21b). Interestingly, the frequency of NK cells similarly increases in KPG1 tumors induced by adenoviral Ad5.SPC-Cre (unpublished data by C. Contat, 2020), suggests that there is a shared mechanism of chemotaxis of this cell type between the KPG1 and KPL$^{mut/wt}$ cancer cells in the SPC-derived tumors.
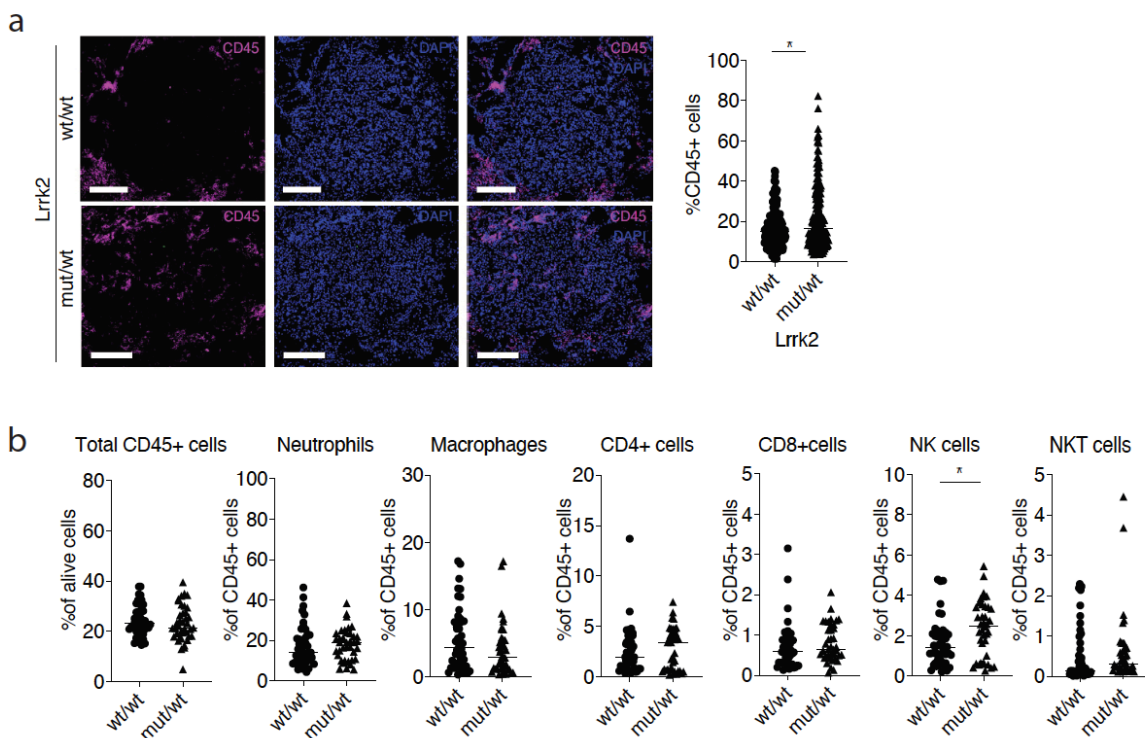
Figure 21. Increased infiltration of Natural Killer cells in KPL^mut/wt tumors. (**a**) Representative images of tumor-bearing lung sections from KP and KPL^mut/wt stained for CD45 and DAPI. Scale bar: 200 μm. Scatter plot with mean ± S.D. showing the total frequencies of CD45+ cells in KP and KPL^mut/wt lesions (n=193 and 216 respectively). Statistical test used, Mann-Whitney test. (**b**) Proportions of total immune cells (CD45+ cells), Neutrophils, Macrophages, CD4 T cells, CD8 T cells, Natural Killer cells (NK), and Natural Killer T cells (NKT). Statistical test used, Mann-Whitney test.

3.4.2.4. LB-associated proteins are more strongly expressed in KPL compared to KP tumors

As part of the characterization of the KP and KPL ^mut/wt tumors, and since Lrrk2 expression was maintained in KPL^mut/wt lesions (Figure 19d), we wondered if other lamellar body-related proteins are similarly maintained in advanced tumors. Immunofluorescence of whole KP and KPL^mut/wt lung sections with two LB markers, pro-SPC, and Abca3, revealed that the protein levels of both of them are expressed significantly more in KPL^mut/wt compared to the KP tumors (Figure 22)
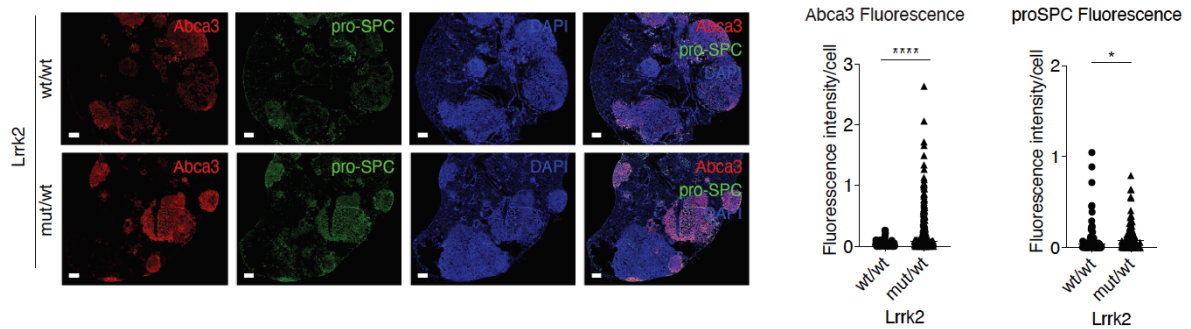
Figure 22. Pro-SPC and Abca3 protein levels are maintained in KPL^mut/wt tumors. Representative images of whole tumor-bearing KP and KPL^mut/wt lung sections stained for pro-SPC or Abca3 and DAPI. Scale bar: 500 μm. Scatter plot with mean ± S.D. showing the total fluorescent intensity per cell for pro-SPC or Abca3 in KP and KPL^mut/wt lesions. Statistical test used, Mann-Whitney test.

3.4.2.5. KPL^mut/wt cancer cells down-regulate pathways that are regulated by the mTORC1

Bulk RNA of KP, KPL^mut/wt and KPL^mut/mut CD45-negative sorted tumor cells was sequenced in an attempt to characterize the KPL ^mut/wt cells and identify regulatory pathways that are affected by the Lrrk2 mutant. Analysis revealed that several signaling pathways that are known to be regulated by mTORC1 are downregulated in KPL^mut/wt cells. Those include the lysosome pathway, the fatty acid metabolism, as well as the insulin signaling pathways (Figure 23a). The downregulation of *Lrrk2* expression in KPL^mut/wt cells was co-occurring with the downregulation of mTORC1-target pathways which indicate an active mTORC1 signaling. Hence, we hypothesized that the increase in the Lrrk2 protein levels that were maintained in KPL^mut/wt tumors (Figure 20d), will be linked with an inactive mTORC1 signaling. To test such a hypothesis, whole lung tumor sections of KP and KPL^mut/wt mice were stained for two downstream effectors of mTORC1, the phospho-S6 Kinase (p-S6K) and the transcription factor EB, Tfeb. Quantification of the proportions of p-S6K+ and p-Tfeb+ cells in each lesion revealed no change in p-S6K+ cells between the two groups, but there was a decrease of the p-Tfeb+ cells in KPL^mut/wt tumors (Figure 23b). This decrease was in line with what had been observed in the RNA-sequencing results and made us speculate that there may be another mechanism of regulation of Tfeb, mTORC1-dependent or not, and mediated by the Lrrk2 kinase activity.
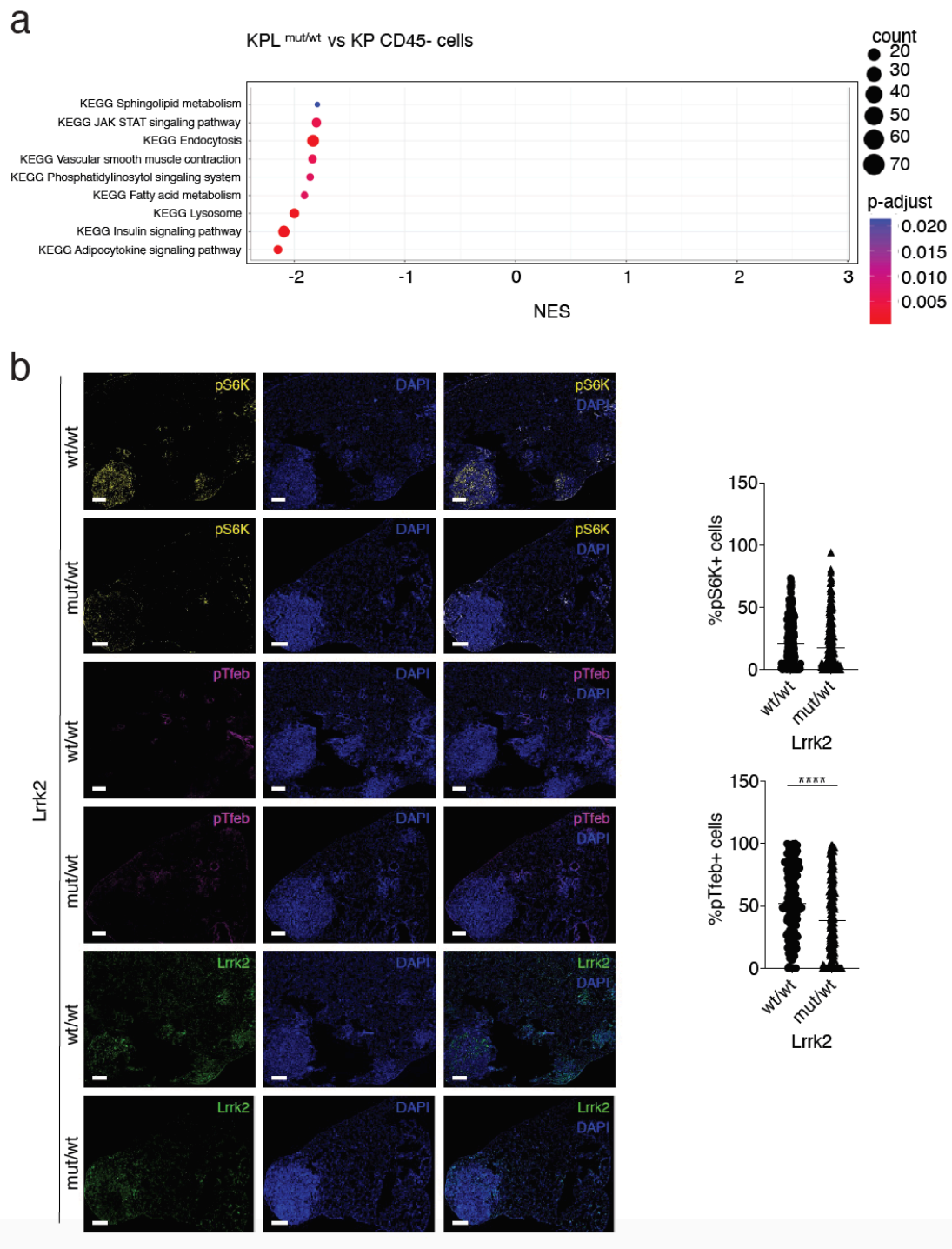
Figure 23. Decreased phosphorylation of the transcription factor Tfeb. (**a**) Plot illustrating some of the mTORC1-regulating signaling pathways that were downregulated in KPL$^{mut/wt}$ compared to KP cancer cells. Bioinformatics analysis, courtesy of Dr. N. Zangger. (**b**) Representative images of serial whole tumor-bearing KP and KPL$^{mut/wt}$ lung sections stained for phosphorylated (p)-S6K, phosphorylated (p)-Tfeb or Lrrk2 and DAPI. Scale bar: 400 μm. Scatter plot with mean ± S.D. showing

the total proportion of (p)-S6K+ or (p)-Tfeb+ cells in KP and KPL$^{mut/wt}$ lesions. Statistical test used, Mann-Whitney test.

3.4.2.6. Lrrk2 kinase inhibition alters the activation of mTORC1 and the autophagy levels

In parallel to the immunofluorescent staining of phosphorylated S6K and Tfeb, I tested if pharmacological inhibition of Lrrk2 kinase alters the activation of mTORC1. As a readout, I analyzed mTOR autophosphorylation in a panel of cell lines that I derived from KP, KPL$^{mut/wt}$ and KPL$^{mut/mut}$ tumors (Figure 24a). Before treating any of these cell lines with the Lrrk2-specific inhibitor MLi-2, it was important to first assess whether they express Lrrk2. Analysis by RT-qPCR showed that the expression level of *Lrrk2* varied considerably among the cell lines examined regardless of their Lrrk2 genotypes (Figure 24b). After confirming that the cells express *Lrrk2*, they were plated, grown in culture for two days, and 0.1µM of MLi-2 or Temsirolimus, an mTOR inhibitor, were added and incubated for 4h. Cell pellets were used for Western Blot analysis.

Detection of the phosphorylation of a known substrate of Lrrk2, the Rab12 at the S106 site, was used to assess the efficiency of the Lrrk2 kinase inhibition. Figure 24c illustrates that upon MLi-2 treatment, there was a significant reduction of pRab12S106/Rab12 ratio in all the cell lines tested, confirming the efficient Lrrk2 kinase inhibition. It was then important to examine if the activation of mTORC1 changes upon MLi-2 treatment. Interestingly, there was an increase in the phosphorylation of mTORC1 in MLi-2-treated cells that did not reach statistical significance (Figure 24d). Finally, the autophagy markers, LC3B and Beclin-1, which had been described to be regulated by two distinct pathways, were used for the assessment of the autophagic flux in these cells upon Lrrk2 inhibition. Interestingly, even when mTORC1 activation was increased, the LC3-II/I levels increased in all cell lines, whereas the Beclin-1 levels remained intact (Figure 24e), confirming that the two proteins are differentially regulated; we conclude Lrrk2 kinase inhibition may lead to an increase in the autophagic flux, in a mTORC1-independent manner.
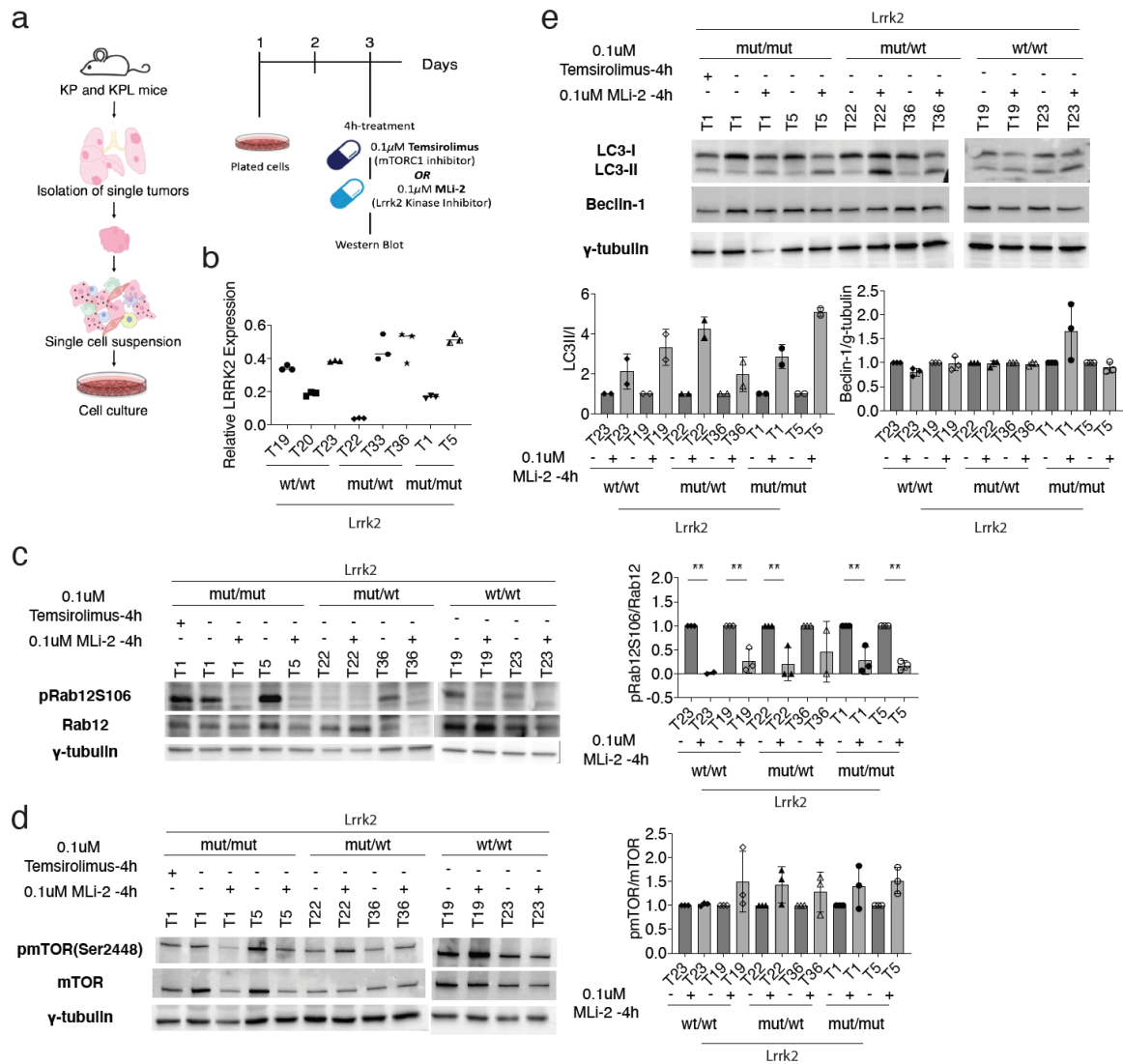
Figure 24. Lrrk2 kinase inhibition induces a slight activation of mTORC1. (**a**) Scheme illustrating the workflow for the isolation and development of tumor-derived cell lines. Scheme showing the time frame of the experiment. (**b**) Scatter plot with mean ± S.D. showing the relative *Lrrk2* expression levels in mouse tumor-derived cell lines as quantified by RT-qPCR. (**c**) Western blot for the detection of pRab12S106, Rab12, and γ-tubulin in 0.1μM of MLi-2, 0.1μM Temsirolimus or DMSO treated KP, KPL [mut/wt] and KPL [mut/mut] cell extracts. Dot plot with mean ± S.D. showing the pRab12S106/Rab12 ratio as quantified from the band intensities. Statistical test used, Mann-Whitney test (**d**) Western blot analysis of phospho-mTORC1 (S2448), mTORC1, and γ-tubulin in extracts of KP, KPL [mut/wt] and KPL [mut/mut] cells after treatment with 0.1μM of MLi-2, 0.1μM Temsirolimus, or DMSO (control). Scatter plot with mean ± S.D. showing the pmTORC1(S2448)/mTORC1 ratio inferred from the band intensities. Statistical test used, Mann-Whitney test (**e**) Western blot for the detection of LC3I, LC3II, Beclin-1, and γ-tubulin in 0.1μM of MLi-2, 0.1μM Temsirolimus or DMSO treated KP, KPL [mut/wt] and KPL [mut/mut] cell extracts. Dot plot with mean ± S.D. showing the LC3-II/LC3-I or Beclin-1/γ-tubulin ratio as quantified from the band intensities. Statistical test used, Mann-Whitney test.

Chapter 4 - Discussion

This *in vivo* study characterized the morphology of healthy wild-type and R1441C Lrrk2 mutant lungs and explored the role of the R1441C Lrrk2 variant in lung adenocarcinoma using the *Kras* $^{G12D/WT}$*; Tp53* $^{fl/fl}$ (KP) mouse model.

4.1. Healthy KPL lungs

4.1.1. Lrrk2 co-localizes with pro-SPC in ATII cells

Lrrk2 was shown to be expressed by ATII cells and in some populations of CD45+ cells (neutrophils, monocytes, macrophages, T-cells, B-memory and a subset of dendritic cells) [125,130,131]. Here, immunofluorescent staining of healthy lung sections showed that Lrrk2 protein in addition was expressed by ATI and CD31+ cells (Figure 15a, b). Furthermore, co-staining of Lrrk2 with pro-SPC revealed the colocalization of Lrrk2 with the LB marker pro-SPC that was not altered in R1441C Lrrk2 mutant ATII cells.

Previous studies have implicated the role of Lrrk2 with the endo-lysosomal system, vesicular trafficking and LB-homeostasis [124,139,134]. Lrrk2 has been shown to be activated and recruited to lysosomes upon lysosomal overload stress induced by the lysosomotropic agent chloroquine (CQ). There, it phosphorylates at least two known substrates, Rab8 and Rab10 [92], stabilizing them on the lysosomal membrane. The two Rab proteins then regulate their effector proteins EHBP1 and EHBP1L1 to thereby control the lysosomal enlargement and secretion [132]. Overexpression of PD-associated mutant forms of human *LRRK2* in HEK293 cells resulted in their recruitment to lysosomes and suppressed the lysosomal enlargement that is normally seen upon CQ treatment [132]. Furthermore, the role of Lrrk2 in LBs has been revealed in *Lrrk2* KO animals. It was described that *Lrrk2* KO ATII cells accumulate enlarged and vacuolated LBs [124,135]. Interestingly, stimulation of isolated *Lrrk2* KO ATII cells with ATP *in vitro* led to faster LB exocytosis compared to the control [121]. These results contrast those of Araki et al., who detected a decreased concentration of SPC in BALF of *Lrrk2* KO mice, pointing towards an impaired LB-exocytosis in *Lrrk2* KO cells *in*

vivo[140]. Overall, these results suggest that Lrrk2 has a crucial role in lysosomal and LB homeostasis, in line with its localization on lysosomal membranes. Further analysis of the proteomes of *Lrrk2* KO and wild-type LBs by mass spectrometry showed an increased accumulation of many Rab proteins, including the Rab8 and Rab10 in the *Lrrk2* KO LB fraction [140]. Based on these results and the similarities between LBs and lysosomes, we hypothesize that the localization of wild-type and R1441C mutant Lrrk2 in pro-SPC+ areas may point to a role of Lrrk2 in the secretion of LBs, probably in a similar mechanism as the one observed in stressed lysosomes.

4.1.2. No morphological or ultrastructural changes in KPL ATII cells

Previous analysis of *Lrrk2* KO mice revealed that the size of ATII cells in the lung and the number of their vacuolated LBs were increased compared to the wild-type. However, whether the R1441C mutation alters the function of Lrrk2 in the lung is not known. To explore if it influences LB formation or function, I compared ATII cells in lungs of wild-type versus R1441C *Lrrk2* mice using light and electron microscopy. ATII cells of R1441C Lrrk2 mutant mice were not overtly abnormal in size or shape, and their LBs displayed no change in the dense multi-lamellar morphology that is characteristic of this organelle.

Proteomic analysis previously indicated that the enlargement of LBs in *Lrrk2* KO cells is mediated by the subunit BORCS6 of the BLOC-1-related complex (BORC). Specifically, it was proposed that Lrrk2 regulates the binding of BORCS6 on the LB membrane. However, when *Lrrk2* is deleted, BORCS6 together with LAMTOR regulates the LB enlargement [140]. Lrrk2-dependent phosphorylation of BORCS6 was not detected in cells overexpressing Y1699C mutant *Lrrk2*, and there is no data for the effect of the mutant on the LB enlargement or the binding of BORCS6 to the lysosomal membrane. Thus, we assume that since in our model *Lrrk2* is expressed, BORCS6 should be bound on the limiting membrane of LBs, inhibiting their enlargement. This could be a possible explanation for why we do not see any vacuolation of LBs in the healthy KPL lungs.

Regarding the lipid droplet accumulation that was observed in R1441C *Lrrk2* mutant lungs, we presumed that these cells are lipofibroblasts. Even if those cells have not been described to have a role in lung adenocarcinoma, they are known to have a supportive function towards ATII cells, either by stimulating or providing them with lipids for surfactant synthesis [136,137]. Thus, it would be interesting to confirm by immunofluorescence whether these cells are lipofibroblasts. In a second step, one should assess whether the mutant lipofibroblasts accumulate more ORO+ vesicles than the control. Furthermore, lipidomic profiling of isolated ATII cells could provide insights into the role of Lrrk2 in lipid metabolism. PD-associated mutations in LRRK2 are linked to changes in brain and plasma lipids [90,141,142,143]. *Lrrk2* KO mice have an altered sphingolipid composition and increased levels of ceramide in brain [90]. Moreover, R1441C *LRRK2* PD carriers have decreased levels of cholesterol, whereas G2019S carriers have reduced levels of ceramide and diacylglycerol in their plasma [141,142].

4.1.3. Trend for a decreased SPC concentration in BALF of heterozygous KPL mice

Assessment of the pro-SPC concentration in BALF of Lrrk2 wild-type and R1141C mice revealed a decreased concentration of pro-SPC in R14414C *Lrrk2* heterozygous lungs.

In *Lrrk2* KO mice, it was shown that ATII cells accumulate more and bigger LBs, which are secreted faster than in wild-type cells upon ATP stimulation *in vitro*. Also, measurement of secreted radiolabeled phospholipids showed that their concentration was decreased in *Lrrk2* KO cells, suggesting that either the *Lrrk2* KO LBs had a reduced phospholipid content, or that the packing of lipids in LBs was impaired [124]. An opposing study in *Lrrk2* KO mice demonstrated lower concentration of SPC in BALF of those animals, implying that *Lrrk2* KO cells have an impaired exocytic capacity *in vivo* [140]. Furthermore, in the context of PD, homozygous R1441C *LRRK2* knock-in (KI) adrenal chromaffin cells secrete less of catecholamine, pointing to an impaired exocytic mechanism [13]. However, the underlying mechanism is not known. Furthermore, none of these experiments provided any information about the

intracellular Ca^{2+} level, which is the physiological stimulus driving LB exocytosis in ATII cells [124].

The decrease of SPC in BALF of heterozygous KPL mice that we observed in heterozygous R1441C mutant *Lrrk2* lungs indicates that their ATII cells also likely secrete fewer LBs in the alveolar space. To further validate this hypothesis and to more accurately assess how the R1441C mutation affects LB exocytosis, stimulation of *Lrrk2* KO and wild-type ATII cells with 100 *μ*M ATP and monitoring of the intracellular Ca^{2+} concentrations and LB-fusion events should be performed using the protocol of Frick et al. [63]. Alternative possible scenarios such as impaired SPC trafficking to LBs, or premature cleavage of pro-SPC in R1441C *Lrrk2* mutants seem less likely since the immunofluorescent staining of pro-SPC with Lrrk2 shows its accumulation in intracellular vesicles and not at the plasma membrane (Figure 15e) [144].

4.2. LRRK2 expression in LUAD patients

LRRK2 expression in LUAD patients has been described previously [145,146,147]. Firstly in an analysis of the TCGA LUAD RNA-seq data, *LRRK2* was identified as a downregulated gene when its expression was compared in tumors versus healthy parts of the lungs [145]. Subsequent bioinformatic analysis of four messenger RNA microarray datasets (GSE18842, GSE40275, GSE43458, and GSE102287) from the Gene Expression Omnibus (GEO) database showed that LUAD patients with clinical stages II, III or IV expressed lower levels of *LRRK2* compared to patients that had been diagnosed with LUAD Stage I [146]. Moreover, it was the first time that the *LRRK2* high expression was correlated with a better overall survival of LUAD patients. All of these results are in line with what we also obtained by the bioinformatic analysis of the LUAD TCGA patient data.

In a more in-depth analysis using expression-based molecular LUAD subtyping, Lebovitz et al. divided the *LRRK2*- high and low groups into non-terminal respiratory unit (non-TRU) and terminal respiratory unit (TRU) types, and the non-TRU type into proximal-inflammatory (PI) or proximal-proliferative (PP) tumors. Non-TRU LUAD tumors are associated with mutations like *KRAS, TP53, LKB1* and have a worse

survival outcome. The same study also compared all of these LUAD subtypes with the normal lung. Analysis of differentially expressed genes (DEGs) revealed that the non-TRU gene expression profile was characterized by low *LRRK2* mRNA levels and completely distinct from the transcriptome of TRU tumors. Indeed, TRUs instead highly expressed *LRRK2* and shared a similar gene expression profile with the normal lungs, similarly to what we also observed. Furthermore, both the PP and PI subtypes expressing high levels of *LRRK2* upregulated surfactant-related genes and were found to recapitulate more the normal lung physiology. Finally, the *LRRK2*–high PP tumors were more inflamed than the *LRRK2*-low-expressing ones [147].

In the same study, the development of LUAD in *Lrrk2* KO mice that were intraperitoneally injected with a carcinogen present in cigarette smoke was evaluated. *Lrrk2* KO tumors were bigger compared to the control, indicating that the deletion of *Lrrk2* facilitates tumor initiation [147].

Altogether, these data pointed towards a tumor-suppressive function of LRRK2 in lung adenocarcinoma, with the non-invasive TRU subtype to express high levels of *LRRK2* compared to the non-TRU. Interestingly comparison of the non-TRU PP or PI *LRRK2* high and low groups, the *LRRK2* high one always correlated with an upregulation of gene sets that play a crucial role in the normal lung physiology, like the surfactant metabolism gene set.

4.3. Tumor-bearing KPL mice

4.3.1. LRRK2 overexpression drives the apoptotic cell death of human NSCLC cells

Transient transfection of *LRRK2* in human NSCLC cell lines induced their apoptotic cell death 48h post-transfection (Figure 14b). How LRRK2 facilitated NSCLC cell death is not known. However, Lrrk2 PD-linked mutations display significant neuronal toxicity that can lead to the shortening of primary cortical and pluripotent stem cell-derived sensory neurons [148,149]. Lrrk2-mediated neuronal cell death is mainly due to the KIN and GTPase activities of the enzyme, which perturb downstream signaling

pathways including autophagy, vesicle trafficking, and mitochondrial homeostasis [150,151]. Boecker et al. provided a mechanistic model for the role of G2019S mutant Lrrk2 that disrupts the trafficking of autophagosomes and thus the clearance of misfolded proteins that would eventually lead to cell death through ER stress induction. Specifically, both in primary and in CRISPR-edited stem cell-derived neurons expression of G2019S mutant *LRRK2* at endogenous levels or after CRISPR-guided knock-in induced the recruitment of the motor adaptor JNK- interacting protein 4 (JIP4) to the autophagosomal membrane via its binding to Rab29. Consequently, JIP4 recruited and activated a kinesin that antagonized dynein motor activity. This resulted in dysregulated transport and incomplete maturation of autophagosomes, suggesting an impaired degradation of autophagosomal cargos in neurons that would eventually lead to the accumulation of cellular debris and cell death [152]. Furthermore, there is evidence that mitochondrial-altered homeostasis can lead to neuronal apoptotic cell death through the elevated levels of mitochondrial reactive oxygen species (ROS) production and the inability of the cells to eliminate it [153,154,155]. G2019S LRRK2 PD neuroepithelial stem cells (NESCs) have an increased number of mitochondria that are more fragmented, cleared up less, and produce an excess of ROS compared to the control [154].

Besides the role of the KIN and ROC-COR domains in neuronal cell death, a motif in the ARM domain of LRRK2 has been described to activate the extrinsic cell death pathway. The interaction of LRRK2 with the FAS-associated death domain protein (FADD) stimulates the mitochondria-independent extrinsic proapoptotic pathway via Caspase-8 [156]. Finally, another study described the role of the LRR and WD40 domains in mitochondrial-dependent apoptosis, involving cytochrome c, Apaf-1, and caspase-3 [155].

In our overexpression system, the transiently transfected *LRRK2* was wild-type. Nevertheless, the increased kinase activity induced by the overexpression may perturb autophagosomal activity and/or mitochondrial homeostasis. The latter may in turn activate the intrinsic cell death pathway.

4.3.2. Increased Lrrk2 protein levels in KPL tumors

Quantification of the Lrrk2 protein levels by immunofluorescence in tumors of KP and KPL mice revealed that Lrrk2 fluorescent intensity/cell was significantly increased in KPL compared to control 24 weeks post tumor initiation. To elucidate if this increase was stage-dependent, the Lrrk2 protein levels were assessed in different tumor grades, from alveolar hyperplasia (AH) to grade 4. During AH, the Lrrk2 fluorescent intensity/cell was the same in KP and KPL (Figure 21a). However, this does not necessarily mean that the gene expression of Lrrk2 was regulated identically in these two genotypes. Indeed, some indication of possible differential regulation comes from our RNA-sequencing analysis, where the *Lrrk2* gene appeared to become more severely downregulated in KPL than in KP tumors. Moreover, Lrrk2 is degraded by chaperone-mediated autophagy (CMA) [89]. Compared to wild-type Lrrk2, the R1441C mutant associates less with the lysosomal LAMP-2A and thus is less efficiently internalized and degraded in the lysosomal lumen [89]. Impaired degradation would explain why the R1441C Lrrk2 mutant protein accumulated at increased levels in KPL tumors. Alternatively, the R1441C mutation may impair a negative feedback loop that normally inhibits the Lrrk2 expression when intracellular levels of the protein exceed the demand.

4.3.3. Altered mTORC1 signaling in KPL tumor cells *in vivo* and *in vitro*

As mentioned above, bulk RNA-sequencing of KP and KPL CD45 negative sorted cells revealed that *Lrrk2* was downregulated more in KPL tumors compared to KP. Concomitantly, we noticed that KPL cells downregulated lysosomal and fatty acid metabolism gene signatures. The latter involved several genes important in the beta-oxidation of fatty acids (like the Carnitine Palmitoyltransferase 1A (*Cpt1a*), Medium-Chanin Acyl-CoA Dehydrogenase (*Acadm*) and Short-Chain Acyl-CoA dehydrogenase (*Acadsb*)) (data are not shown). Both lysosomal activity and fatty acid oxidation are known to be downregulated when mTORC1 is in an active phosphorylated form. More specifically, in nutrient-abundant cells, active mTORC1 phosphorylates the transcription factor EB (TFEB) to inhibit its nuclear translocation and thus the expression of lysosomal and autophagy genes [29]. In the same context, beta-oxidation is inhibited and instead, the anabolic pathways are positively regulated

Hence, we reasoned that when *LRRK2* is downregulated, the mTORC1 may become more active to thereby curb lysosomal biogenesis and fatty acid metabolism.

To test whether the Lrrk2 activity can affect the activation of mTORC1 *in vitro*, KP and KPL tumor-derived cell lines were treated with the Lrrk2 kinase inhibitor MLi-2 for 4hrs. Western blot analysis showed that there is a trend for increased phosphorylation and thus activation of mTORC1 in the MLi-2 treated KP and KPL cells, which did not reach statistical significance, though. This combined with the *in vivo* results, made us hypothesize that Lrrk2 regulates the activation of mTORC1. In keeping with this hypothesis, Albanese et al. described the downregulation of *mTOR* and *TFEB* expression in 12-month old kinase dead mice, while G2019S knock-in mice accumulated LAMP2 and downregulated key autophagy-lysosome genes like the *LAMP-2*, *mTOR, TFEB* and *GBA1* [157].

Surprisingly, upon Lrrk2 kinase inhibition *in vitro* and simultaneous activation of mTORC1, I observed increased autophagy. Such an elevation in autophagy had previously been reported in astrocytic cell models where treatment with the Lrrk2 kinase inhibitor LRRK2IN1 stimulates macroautophagy [158,159]. Manzoni et al. concluded that this induction was regulated in a mTOR-independent way that involved PI3K and Beclin-1 activation. Evaluation of changes in Beclin-1 levels among MLi-2 treated and untreated cells did not reveal any differences (Figure 24e). However, we cannot exclude that PI3K and/or Beclin-1 are inactive in the MLi-2 KP and KPL treated cells. To test this, we should knock-down *Beclin-1* and then treat cells with a Lrrk2 kinase inhibitor to assess if the autophagy levels change and if such a change is mediated by Beclin-1.

Overall, the RNA-sequencing and *in vitro* results indicate that Lrrk2 negatively regulates the activation of mTORC1. In parallel, the *in vitro* Lrrk2 kinase inhibition experiments showed that Lrrk2 curbs autophagy through an mTOR-independent pathway. Future studies are warranted to investigate the possible roles of PI3K or Beclin-1 in this process.

4.3.4. Decreased proportion of p-Tfeb+ cells in KPL tumors

Quantification of the proportion of pS6K+ and pTfeb+ cells in KP and KPL tumors revealed no differences in the proportions of pS6K+, but a decrease in the pTfeb+ cells in KPL lesions. These data do not support our hypothesis that mTORC1 activity is diminished in the KPL tumors *in vivo*. Among possible alternative mechanisms to account for altered phosphorylation of Tfeb and its nuclear translocation, it may be worth considering a role for mTORC2 or mTORC3 complexes.

In a recent publication of Nabar et al., a CD38-LRRK2-TFEB signaling axis was identified in B lymphocytes and macrophages [160]. CD38 is a type II transmembrane protein at the cell surface and in endosomes that catalyzes the conversion of nicotinic adenine dinucleotide (NAD) into cyclic ADP-ribose (cADPR), which is the precursor of Nicotinic acid adenine dinucleotide phosphate (NAADP). NAADP acts as a calcium-mobilizing second messenger that can trigger the release of calcium from intracellular stores, like lysosomes [161]. Internalization of CD38-LRRK2 complexes into the endo-lysosomal system generates an NAADP-dependent calcium signal that leads to activation of calcineurin and downstream dephosphorylation and nuclear translocation of TFEB [160]. mTOR signaling appeared to be unaffected by the G2019S LRRK2, at least when examined in HeLa cells, and AMPK was suggested to promote TFEB target gene transcription via epigenetic modifications induced through the coactivator-associated arginine methyltransferase 1 (CARM1). Finally, given the inhibition of TFEB nuclear translocation observed after calcium chelation with BAPTA-AM, inhibition of calcineurin by FK506, knock-down of the calcineurin subunit *PPP3CB*, or knock-down of the NAADP-gated lysosomal calcium channel TPCN2, it was proposed that the G2019S LRRK2 induces activation of TFEB through an NAADP TPCN2-lysosomal calcium-dependent pathway [160]. Here, I compared the activation state of AMPK in KP versus KPL cells by analyzing its phosphorylation. Regardless of whether the cells were treated with the LRRK2 inhibitor MLi-2, phospho-AMPK was low, and no differences were observed between treated and untreated cells. However, one caveat is that in some blots the phospho-AMPK was undetectable (data not shown). Furthermore, the relative expression levels of Tfeb target genes or the translocation efficiency of Tfeb in R1441C *Lrrk2* mutant cells were not analyzed. However, upon

MLi-2 treatment of KP and KPL cells, there was induction of autophagy. If the R1441C Lrrk2 mutant induced the nuclear translocation of Tfeb similarly to the overexpressed G2019S LRRK2 in Hela cells, the basal levels of autophagy in R1441C Lrrk2 cells, should have been high and should have decreased upon MLi-2 treatment. In my western blot analysis, I observed the opposite effect. Hence, it still remains to be demonstrated whether the Lrrk2 R1441C mutant increases the AMPK activation of autophagy in cancer cells.

Chapter 5 - Conclusions

In this *in vivo* study, I characterized morphologically the R1441C Lrrk2 mutant lungs and assessed the role of Lrrk2 in lung adenocarcinoma.

Healthy R1441C Lrrk2 ATII cells had a normal size and shape, and their LBs had a physiological dense multi-lamellae morphology. *Lrrk2* is expressed by ATI, ATII, CD31+, and CD45+ cells in healthy lungs. In ATII cells, it was localized in pro-SPC+ regions corresponding to LBs. The localization of Lrrk2 in the cells examined above did not change in R1441C *Lrrk2* mutant mice. Evaluation of the *in vivo* functionality of the mutant ATII cells showed that there is a trend for decreased SPC concentration, suggesting that Lrrk2 may regulate LB exocytosis.

Assessment of the role of Lrrk2 in lung adenocarcinoma was performed through bioinformatic analysis of the available patient records from the TCGA database and through *in vivo* experiments in *Kras* $^{G12D/WT}$*; Tp53* $^{fl/fl}$ (KP) mice. Our bioinformatic analysis of human LUAD data showed that high *LRRK2* expression correlates with a better survival outcome and that these tumors show transcriptional profiles resembling healthy ATII cells. Tumor growth rate analyses of KPL lesions did not show a consistent reduction in comparison to KPs. Quantification of the Lrrk2 protein levels by immunofluorescence revealed that Lrrk2 was maintained more in KPL compared to KP tumors, probably because of the stabilization of the mutant protein and its slower degradation by the CMA pathway.

Furthermore, considering together RNA-sequencing and *in vitro* results, we think that both the wild-type and R1441C *Lrrk2* can inhibit autophagy, with this effect being exacerbated in mutant cells. On top of that, Lrrk2 mutant cells have been shown to have impaired autophagosome trafficking that could probably add to its autophagy-suppressive role [152]. Autophagy has been shown to play a very striking role in lung tumor progression, with *Kras* $^{G12D/wt}$ *TP53* $^{fl/fl}$ *Atg7* $^{fl/fl}$ mice developing benign oncocytomas that failed to progress toward adenomas or adenocarcinomas in comparison to *Atg7* wild-type tumors [33, 34]. However, in our model we didn't observe a reduction in lung tumorigenesis *in vivo*. which made us hypothesize that the autophagy inhibition may occur in early stages of tumor development but then this

effect is lost when KPL tumors can catch up the KPs. Considering these, my current model is that Lrrk2 suppresses autophagy through the negative regulation of the PI3K/Beclin-1 pathway, as previously described [158].

Furthermore, Lrrk2 slightly alters the mTORC1 activity, which can in turn impact many pathways, including cellular metabolism pathways in KPL cells. For example, mTORC1 has been linked with the regulation of glucose metabolism. Activation of mTORC1 can lead to the expression of *GLUT1*, which is important in the lung adenocarcinoma progression [127,162,163]. Hence, Lrrk2-mediated regulation of mTORC1 could impact on the progression of the disease by inhibiting tumor-promoting pathways, like the glucose metabolism pathway. Finally, we can see that there are fewer Tfeb+ cells in KPL tumors, but with the current data, we cannot explain how the phosphorylation of Tfeb is regulated and what are the downstream effects.

In the future, it would be important to investigate the role of PI3KIII and Beclin-1 in the suppression of autophagy that is observed in KP and KPL cells. Furthermore, identifying the signaling pathways that regulate Tfeb phosphorylation in those cells could promote our understanding of the role of Lrrk2 in autophagy, considering that Tfeb is a master transcription factor of autophagy genes.
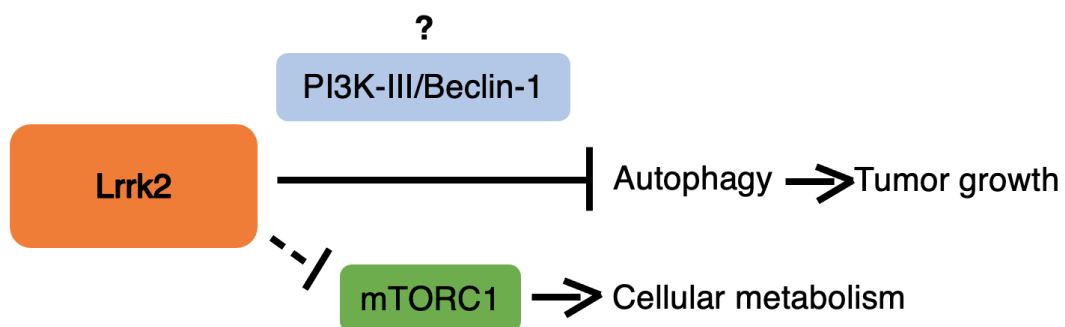
Figure 25. Current working model. Lrrk2 blocks autophagy which is known to facilitate tumor growth progression. This is probably mediated through the inhibition of the PI3K-III/Beclin-1 pathway. Lrrk2 also alters the activation of mTORC1 which regulates many biological pathways including cellular metabolism.

Chapter 6 - Material and Methods

6.1. Bioinformatic Analysis

6.1.1. The Cancer Genome Atlas data processing

The human lung cancer data were retrieved from the public Cancer Genome Atlas (TCGA) database specific for the LUAD data repository (TCGA: https://www.cancer.gov/tcga). Those samples contain clinical information and mRNA sequencing data of 511 LUAD patients (448 samples had also survival data). To remove genes with too low expression of genes with less than one transcript, around fifty samples were removed. After this filtering step, transcript counts for 16'093 genes remained. The binary logarithm (*log2*) was applied to the read counts before batch correction and normalization by the voom function of the 'limma' R-package. Samples were then ordered by *LRRK2* expression, as *LRRK2*-low or -high expression groups.

6.1.2. Human survival analysis

The prognostic value of *LRRK2* expression in LUAD was analyzed by a Kaplan Meier overall survival plot via the 'survival' and 'survminer' R-packages. LUAD patients with available survival data (n=448) were divided into two groups based on the median expression of *LRRK2* and the difference in survival was computed between the two groups. It was evaluated by a log-rank test, and the time threshold was set at 10 years. A significance threshold of $p < 0.05$ was used for each analysis.

6.1.3. Transcription factor binding sites analysis

JASPAR database of transcription factor binding motifs was used to scan the promoter regions (-2000 -> + 500 nucleotides around the transcription starting site of the main transcript) of the following genes: *ABCA3, LPCAT1, SFTPC, LAMP3, SLC34A2,* and

LRRK2. Only the transcription factor binding sites (TFBS) that were predicted with a p-value < 0.05 and were detected in all 6 promoters are presented here.

6.2. Mouse work

6.2.1. Mice

6.2.1.1. Study approval

All the mouse experiments were performed under the Swiss regulations, under the approval of the Veterinary Authority of the Canton de Vaud, Switzerland, License number 2391.6.

6.2.1.2. Engineered mouse models

6.2.1.2.1. *Kras $^{LSL-G12D/WT}$; Tp53 $^{fl/fl}$ mouse models*

Kras $^{LSL-G12D/WT}$ (K) and *Tp53 $^{fl/fl}$* (P) mice in a C57BL6/J background were purchased from the Jackson Laboratory and were inbred to obtain the *Kras $^{LSL-G12D/WT}$; Tp53 $^{fl/fl}$* (KP) mice.

6.2.1.2.2. *Lrkk2 $^{R1441C/WT}$ mouse model*

Lrkk2 $^{R1441C/WT}$ mice (L) in a C57BL6/J background were purchased from the Jackson Laboratory and were crossed with *Kras $^{LSL-G12D/WT}$; Tp53 $^{fl/fl}$* (KP) mice to obtain the *Kras $^{LSL-G12D/WT}$; Tp53 $^{fl/fl}$; Lrkk2 $^{R1441C/WT}$* (KPL $^{mut/wt}$) and *Kras $^{LSL-G12D/WT}$; Tp53 $^{fl/fl}$; Lrkk2 $^{R1441C/R1441C}$* (KPL $^{mut/mut}$) mice.

6.2.2. Genotyping

DNA was extracted from the toe clipping of mice aged 7-12 days. Samples were lysed in 600μl of 50mM NaOH and boiled for 30min at 110°C. Then cooled down for 5min at RT and 50μl of 1M Tris-HCl pH 8.0 was added to each sample. Centrifugation of

13`000 revolutions per minute (rpm) for 6min followed and 2*µ*l of the supernatant was utilized for genotyping. The mouse PCR primer pairs used for each gene are listed in table 3.

Table 2. Primers used for the genotyping of *Kras*, *p53,* and, *Lrrk2* wild-type and mutant alleles. Primer sequences are in 3'-5' orientation.

Gene	Allele	Primer	Amplicon Size(bp)	Primer Sequence
Kras	WT	Forward	500	GTCGACAAG CTATGCGGG
		Reverse		CGCAGACTGTAGAGCAGCG
	LoxP (G12D)	Forward	500	CCATGGCTTGAGTAAGTCTGC
		Reverse		CGCAGACTGTAGAGCAGCG
p53	WT	Forward	288	CACAAAAACAGGTTAAACCCAG
	LoxP	Reverse	370	AGCACATAGGAGGCAGAGAC
Lrrk2	WT	Forward	315	GGAAGGTTTTCCTCCCCGGAAACA
	R1441C	Reverse	676	CTAGATAGGACCGAGTGTCGCAGAG

6.2.3. Mouse intratracheal instillations for tumor initiation

Fourteen-week-old mice were intratracheally instilled with Ad5.SPC-Cre viral vectors for the delivery of the Cre-recombinase to the ATII cells (SPC+ cells). The procedure that was followed is based on the DuPage et al. mouse instillation protocol[17] Mice were weighed and anesthetized with intraperitoneal injection (IP) of 0.1 ml / 10 g of mouse body weight, of 4 mg/ml ketamine (Ketasol-100, Graeub, ATC-vet QN01AX03) and 0.1 mg/ml medetomidine (Dormitor, Orion Corporation, ATC-vet QN05CM91) in sterile 0.9% NaCl (B. Braun, ATC-vet B05BB01). Intratracheal viral delivery was performed 20min post anesthesia, in which 4.2×10^8 plaque forming units (PFU) were administered per animal. At least 30min after the injection of the anaesthetics, subcutaneous (SC) administration of 0.05 ml / 10 g of mouse body weight of Antisedan (Antisedan, Orion Pharma, ATC-vet QV03AB90) followed.

6.2.4. Tumor monitoring by Micro-Computated Tomography (*µ*CT)

Micro-computated tomography (*µ*CT) was used for the monitoring of lung tumors with the use of the Quantum FX by PerkinElmer. Animals were first anesthetized with isofluorane (Piramal, 56.761.002) and were maintained under anesthesia throughout the scanning procedure. The lung imaging was set at 50 µm voxel size, with retrospective gating. The determination of the tumor volumes was performed with the Horos Software, and further analysis was completed with Excel, Microsoft Office.

6.2.5. Analysis of tumor and lung weights

At sacrifice, whole lungs were collected and weighted into an analytical laboratory scale. Then, single lobes were separated in a DMEM-containing 10cm cell culture dish, on ice and single tumors were isolated and weighed.

6.3. Tissue processing

6.3.1. Whole lung and single tumor embedding in Optimal Cutting Temperature compound (OCT)

At sacrifice, mice were placed with the front side facing up on a styro-foam panel and the arms and the legs were fixed with needles. With the use of scissors an incision in the skin from abdomen to neck was made, and the skin was further cut to expose the thoracic cage and the neck. The ribs were then cut on the sides so as to expose the lungs and the heart. To find the trachea, the muscles of the neck were removed. With the use of tweezers and scissors the trachea is then cut and a 22 G x 1" Surflo I.V. Catheter was inserted in it. 1ml of 50% phosphate buffered saline (PBS) 1x and 50% OCT was intratracheally instilled to expand the lungs and the trachea was blocked with the use of tweezers. The whole lung was collected and the lung lobes were then separated and placed in OCT-containing molds on dry ice. In the case of single tumor embedding, single tumors were collected and placed directly in OCT-containing molds on dry ice. The cryoblocks were then cut in 8*µ*m thickness on a Leica CM1950 cryostat and both the blocks and the slides were stored at -80°C.

6.3.2. Whole lung embedding in paraffin

For the collection of whole mouse lungs the procedure is the same as described in 6.3.1. section, but instead of OCT, 4% paraformaldehyde (PFA) in PBS 1x was instilled through the trachea. Then the lungs were separated into single lobes and were placed in cassettes into a becker containing 4% PFA. The following steps of waxing and embedding of the tissue were performed by the Histology Core Facility at EPFL, Lausanne. Sections were cut in $8\mu m$ thickness on the microtome Hyrax M25 and the slides were stored at 4°C.

6.3.3. Tissue staining

6.3.3.1. H&E staining

Lung tissue section dewaxing and hematoxylin and eosin (H&E) staining were performed by the Histology Core Facility at EPFL, Lausanne.

6.3.3.2. Immunofluorescence staining

Slides were transferred from -80°C to room temperature (RT) where they were incubated for 15min to dry. A rehydration step of 10min with PBS 1x followed and then the samples were fixed in 4% PFA for 10min at RT. After the three 5min washes with PBS 1x, the sections were permeabilized for 10 minutes with 0.1% Triton X-100 at RT. Three 5min washes with PBS 1x followed and the blocking with 2% bovine serum albumin (BSA) in PBS 1x for 1h at RT started. The primary antibodies were diluted in 2% BSA in PBS and incubated overnight at 4°C. The following day, the slides were washed three times for 5min with PBS 1x and the secondary antibody mix was added. The sections were incubated for 1h at RT with the secondary antibody mix and then washed three times for 5 minutes with PBS 1x. Finally, DAPI was added and incubated for 20min at RT. One 5-minute wash followed and coverslips were mounted with the use of Fluoromount™ Aqueous Mounting Medium. The samples were stored overnight at RT to dry and the next day placed at 4°C.

Table 3. List of primary antibodies that were used for immunofluorescent staining of cryosections.

Target	Dilution	Supplier	References
anti-ABCA3	1/100	Biolegend	911001
anti-CD31	1/100	eBioscience	14-0311-82
anti-CD45	1/100	eBioscience	14-0451-82
anti-Cleaved Caspase-3 (Asp175)	1/100	Cell Signaling	9661S
anti-Ki-67	1/100	ThermoFisher Scientific	MA5-14520
anti-LRRK2	1/100	Abcam	ab133474
anti-phospho-RAB10 pT73	1/100	Abcam	ab230261
anti-phospho-p70 S6 Kinase (Thr389)	1/100	Cell signaling	9234
anti-phospho-TFEB (Ser211)	1/100	Invitrogen	PA5-114662
anti-Podoplannin	1/100	R&D systems	AF3244
anti-proSPC	1/100	Millipore	Ab3786

6.3.3.3. Lipid droplet staining

Lung tissue sections were stained for neutral lipids with Oil Red O (ORO) and for nuclear staining with Alcian blue by the Histology Core Facility at EPFL, Lausanne.

6.3.4. Tumor grading

Haematoxylin and eosin (H&E) stained lung cryosections were used for the assessment of the tumor grades. That classification was based on a previously published classification system that categorizes the lesions as alveolar hyperplasia (AH), or as tumors on a 1-5 severity grading scale, with grade 1 to be the adenomas and grade 5 the adenocarcinomas [18]. The classification of tumors into the different grades was conducted by the veterinary pathologist, Dr. med. vet., PhD, Göpfert Christine.

6.3.5. Tumor number counts

Haematoxylin and eosin (H&E) stained lung cryosections were used for the assessment of the tumor numbers. That was conducted by the veterinary pathologist, Dr. med. vet., Göpfert Christine.

6.4. Cell-based techniques

6.4.1. Analysis of the tumor microenvironment by flow cytometry

At the day of sacrifice, single lung tumors were collected and kept on ice in 24-well cell culture plates (Falcon, BDAA353047) containing 0.5ml of digestion mix (9.4mg/ml collagenase-I and 0.25g/ml DNase-I in DMEM). With the use of scissors, tumors were cut into smaller pieces and 2ml of digestion mix per well were added. The tumor samples were then transferred into gentleMACS tubes (Miltenyi Biotech, Ref: 130-096-334) and placed into the gentleMACS octo Dissociator (Miltenyi Biotech) for mechanical and enzymatic processing, to obtain single-cell suspensions. Following the digestion, the samples were centrifuged for 3min at 1500 rpm, resuspended into 5ml of basal DMEM, filtered through 70μm pre-separation filters (Miltenyi Biotech, Ref: 130-095-823) into 15ml falcon tubes, and centrifuged for 10min at 1500 rpm to remove the supernatant. Next, the samples were resuspended into 0.1ml FACS buffer (containing 2% Fetal Bovine Serum (FBS) (Gibco, 10270106) and 0.5mM EDTA (AppliChem, A4892) in PBS 1x (BioConcept, 3-05F29-I)) per 20mg of tissue. 0.1ml of the samples were then transferred to a 96-well cell culture plate for staining and use for the flow cytrometric analysis. Cells were first stained with the Live and Dead blue dye (Invitrogen, L23105) in PBS 1x for 20 min at 4°C, washed 3 times with 0.1ml of FACS Buffer and centrifuged for 10min at 1500 rpm. In parallel, the antibodies (Table 5) were diluted into FACS Buffer, and a 15min incubation at 4°C followed. After that, the cell suspensions were washed 3 times with 0.1ml of FACS Buffer, centrifuged for 10min at 1500 rpm, fixed with fixation and permeabilization buffer (Invitrogen, 00-5523-00) for 20 minutes at 4°C and washed three times for 5min with FACS Buffer. All the samples were finally resuspended into 0.15ml of FACS Buffer and transferred into microtubes (Thermo Scientific, 15086) to be acquired with the LSR Fortessa. The flow cytometry data were analyzed with FlowJo X software (FlowJO LLC ©).

Table 4. List of fluorophore-conjugated antibodies that were used for the detection of the main immune cell populations by flow cytometry.

Target	Dilution	Fluorophore	Supplier	References
anti-Ly6C	1/100	Alexa-Fluor-700	Biolegend	128024
anti-CD11c	1/100	Brilliant Violet 421	Biolegend	117330
anti-CD8a	1/100	Brilliant Violet 510	BD Biosciences	563068
anti-NK1.1	1/100	Brilliant Violet 650	Biolegend	108736
anti-CD11b	1/100	Brilliant Violet 710	Biolegend	101241
anti-CD4	1/100	Brilliant Violet 785	Biolegend	100552
anti-B220	1/100	APC	Miltenyi Biotec	130-102-259
anti-MHCII	1/100	APC-Cyanine7	Biolegend	107628
anti-Ly6G	1/100	FITC	Biolegend	127606
anti-CD3	1/100	PE-Cyanine5.5`	eBioscience	35-0031-82
anti-F4/80	1/100	Brilliant Violet 605	Biolegend	123133
anti-CD45	1/100	PerCp	Biolegend	103130
Live and Dead - Blue	1/400	N/A	Thermo Fisher Scientific	L34962

6.4.2. CD45 positive and negative cell sorting and quality control

Single-cell suspensions were first obtained as described in 6.4.2. section, centrifuged for 10min at 1500rpm and the supernatant was removed. The cell pellets were resuspended in 10ml Red Blood Lysis Buffer 1x, transferred into 50ml Falcon tubes, and vortexed every 2-3min for a total of 10min at RT. After the incubation, the samples were centrifuged for 10min at 1500rpm, the supernatant was aspirated and 1ml of FACS Buffer was added on the top. The cell number of all the samples was determined with the use of a cell counter (Biorad) and the tubes were centrifuged for 5min at 1500rpm. For the staining of the CD45+ cells, 0.01ml of mouse anti-CD45 microbeads (Miltenyi Biotech, 130052301) and 0.09ml FACS Buffer per 10^7 total cells/ sample were added on top of the cell pellets and incubated for 15min at 4°C. Then, the cells were washed with 1ml of FACS Buffer per 10^7 cells/ sample, centrifuged for 10min at 1500rpm and the supernatant was removed. The stained cell pellets were resuspended into 0.5ml of FACS Buffer for up to 10^8 cells/sample and placed on the AutoMacs Pro Separator (Miltenyi Biotech) for magnetic sorting of CD45+ cells. Following the cell sorting, CD45 positive and negative cells were collected, centrifuged for 10min at 1500rpm, and resuspended into 1ml FACS Buffer. For the quality control of the sorting, a small fraction of CD45 postive and negative cells was transferred into a 96-well cell culture plate and the rest of the samples were placed into 1.5ml eppendorf tubes, centrifuged for 5min at 1500rpm and stored at -80°C. For the quality control of the sorting, the samples were stained for CD45, incubated for 15min at 4°C,

washed three times for 5min with FACS Buffer and acquired with the LSR Fortessa. Data were analyzed with FlowJo X software (FlowJO LLC ©).

6.4.3. Cell culture

6.4.3.1. Mouse tumor-derived cell lines

Single lung tumors were collected and processed as described in section 6.4.2. to obtain single-cell suspensions. Following the digestion, the samples were centrifuged for 3min at 1500 rpm, resuspended in 7ml complete DMEM (containing DMEM (D5671-500ml) supplemented with 10% Fetal Bovine Serum (FBS) (Gibco, 10270106), 1% Penicilin-Streptomycin (Gibco, 15140-122) and 1% Non-essesntial Amino Acids (Gibco, 11140-035)) and maintained at 37°C under 5% CO_2. The following day the medium was aspirated, the plates were washed two times with PBS 1x, and some days later (depending on the confluency of the attached cells), the cells were expanded.

6.4.3.2. Human Non-Small Cell Lung cancer cell lines

Human Non-Small Cell Lung Cancer cell lines (A549, H441, H1975, H1944, Calu6) as well as the human embryonic cell line (293T) were maintained in DMEM supplemented with 10% Fetal Bovine Serum (FBS) (Gibco, 10270106), 1% Penicilin-Streptomycin at 37°C under 5% CO_2.

6.4.3.3. MLi-2- or Temsirolimus-treated mouse tumor-derived cells

For the *in-vitro* experiments with the mouse tumor-derived cell lines (T1, T5, T19, T22, T23, T36), 10^5 cells were plated in 10cm cell culture dishes containing complete DMEM and grown in culture for two days. The third day after plating the cells, 100nM MLi-2 (MedChemexpress, HY-100411) or 0.1μM, 1 μM, 10μM, 100 μM Temsilolimus (MedChemexpress, HY-50910) or DMSO (for the controls) diluted in complete DMEM, was added to the plates, incubated for 4h and cells collected for further processing.

6.4.3.4. Cell transfection with Lipofectamine reagent

A549, H441, H1975 and 293T cells were transiently transfected with expression vectors with the use of lipofectamine 2000/3000 (Invitrogen, L3000-008). The protocol followed was according to the manufacturer's instructions.

6.5. RNA-based techniques

6.5.1. RNA extraction

6.5.1.1. Total RNA extraction

Total cell RNA was extracted from cell pellets, using the ReliaPrepT^M RNA Cell Miniprep System (Promega, Z6012) according to the manufacturer's instructions. RNA concentration was assessed with a spectrophotometer and the samples were stored at -80°C.

6.5.1.2. Extraction of high-quality total RNA

To extract total RNA from tumors containing less than 10^5 total cells, the RNeasy Plus Micro Kit (QIAGEN, 74034) was used and the protocol followed was according to providers` instructions. RNA concentration was assessed with a spectrophotometer and RNA quality was accessed by the high-sensitivity RNA assay, using a tapestation. Finally, the RNA samples were stored at -80°C.

6.5.2. Reverse transcription

RNA was reverse-transcribed into cDNA with the use of Takara. 500ng of RNA sample was adjusted to a total volume of 8μl in DNase/RNAse free water and then mixed with 5x Takara buffer. The reverse transcription reaction was performed on a thermal cycler according to the manufacturer`s instructions: 10 min at 25°C, followed by 37°C, and finishing by 5 min incubation at 85°C. After the completion of the reaction, the samples were diluted 1:10 in DNase/RNAse-free water and stored at -20°C.

6.5.3. Real-time PCR

Real-time PCR amplifications were performed on 7.5 ng of cDNA samples using the QuantStudio 6 (Applied Biosystems). The distribution of both the cDNA samples and the probes/mastermix was performed by a Microlab STAR Liquid handling system (Hamilton) into 384-well plates. For each sample, 7.5 ng of cDNA, 5 μl of TaqMan Fast Advanced Master Mix 2x (Applied Biosystems, 4444965) and 0.2μl of probes were used. Each sample was analyzed in technical triplicates. Data were analyzed in Excel Microsoft Office and illustrated by GraphPad Prism. The list of commercially available probes is illustrated in the table 6.

Table 5. List of probes used for RT-qPCR analysis of mouse genes.

Mouse gene	Supplier	Mouse Probe Reference
Lrrk2	ThermoFisher Scientific	Mm00481934_m1
Rpl30	ThermoFisher Scientific	Mm01611464_g1

6.6. Protein-based techniques

6.6.1. Protein extraction and Western blot

Cells were lysed in 0.1ml radioimmunoprecipitation assay (RIPA) buffer (150 mM sodium chloride (NaCl) (Fisher scientific, S/3120/60), 20 mM Tris buffer pH 7.4 (Sigma, 93352), 0.1% sodium dodecyl sulfate (SDS) (Applichem, A0675.0500), 0.5% NP-40 (Fluka, 74385) and 0.5% sodium deoxycholate (Sigma, 30970) containing 1 tablet of protease inhibitors per 10ml RIPA buffer (Thermofisscher Scientific, A32953) and 0.01% phosphatase inhibitors (Sigma, P044). Protein concentration was then assessed with the use of a bicinchoninic acid (BCA) assay (Thermofisher Scientific, 23228, 1859078) and absorbance was measured at 562 nm in a spectrophotometer (Plate Reader Spark Tecan). For western blot 50μg of proteins were used, the membranes were blocked in 5% BSA in Tris-Buffered Saline (TBS) 0.5% Tween (TBS-T). The antibodies used for westen blot analysis are shown in table 7. Finally, the imaging of the mebrane`s bands were detected with the ChemiDoc (Biorad) and

quantification of the band intensities performed with the use of the ChemiDoc Biorad Software.

Table 6. List of primary antibodies used for western blot analysis.

Target	Dilution	Supplier	References
anti-Beclin-1	1/1000	Cell signaling	3495S
anti-LC3B	1/1000	Cell signaling	2775S
anti-mTOR	1/1000	Cell signaling	4517
anti-phospho-mTOR (Ser2448)	1/500	Cell signaling	5536
anti-phospho-Rab12 pS106	1/500	Abcam	ab256487
anti-Rab12	1/500	Proteintech	18843-1-AP
anti-γ-tubulin	1/1000	Sigma	T6557

6.7.   Statistical analyses

Plots, graphs and statistical analyses were produced on Prism version 9 and 10.

Chapter 7- References

1. Sung, H. *et al.* Global Cancer Statistics 2020: GLOBOCAN Estimates of Incidence and Mortality Worldwide for 36 Cancers in 185 Countries. *CA. Cancer J. Clin.* **71**, 209–249 (2021).
2. Siegel, R. L., Miller, K. D., Fuchs, H. E. & Jemal, A. Cancer statistics, 2022. *CA. Cancer J. Clin.* **72**, 7–33 (2022).
3. Nicholson, A. G. *et al.* The 2021 WHO Classification of Lung Tumors: Impact of Advances Since 2015. *J. Thorac. Oncol.* **17**, 362–387 (2022).
4. Zito Marino, F. *et al.* Molecular heterogeneity in lung cancer: from mechanisms of origin to clinical implications. *Int. J. Med. Sci.* **16**, 981–989 (2019).
5. Kan, Z. *et al.* Diverse somatic mutation patterns and pathway alterations in human cancers. *Nature* **466**, 869–873 (2010).
6. Greulich, H. The genomics of lung adenocarcinoma: Opportunities for targeted therapies. *Genes and Cancer* **1**, 1200–1210 (2010).
7. Kim, J., Kundu, M., Viollet, B. & Guan, K. L. AMPK and mTOR regulate autophagy through direct phosphorylation of Ulk1. *Nat. Cell Biol.* **13**, 132–141 (2011).
8. Boidot, R. *et al.* Regulation of monocarboxylate transporter MCT1 expression by p53 mediates inward and outward lactate fluxes in tumors. *Cancer Res.* **72**, 939–948 (2012).
9. Mitsudomi, T., Hamajima, N., Ogawa, M. & Takahashi, T. Prognostic significance of p53 alterations in patients with non-small cell lung cancer: A meta-analysis. *Clin. Cancer Res.* **6**, 4055–4063 (2000).
10. Yokoyama, N. *et al.* Kras promotes myeloid differentiation through Wnt/β-catenin signaling. *FASEB BioAdvances* **1**, 435–449 (2019).
11. Juul, N. H. *et al.* KRAS(G12D) drives lepidic adenocarcinoma through stem-cell reprogramming. *Nature* **619**, 860–867 (2023).
12. El Osta, B. *et al.* Characteristics and Outcomes of Patients With Metastatic KRAS-Mutant Lung Adenocarcinomas: The Lung Cancer Mutation Consortium Experience. *J. Thorac. Oncol.* **14**, 876–889 (2019).
13. Arbour, K. C. *et al.* Effects of co-occurring genomic alterations on outcomes in patients with KRAS-mutant non-small cell lung cancer. *Clin. Cancer Res.* **24**, 334–340 (2018).
14. Scheffler, M. *et al.* K-ras Mutation Subtypes in NSCLC and Associated Co-occuring Mutations in Other Oncogenic Pathways. *J. Thorac. Oncol.* **14**, 606–616 (2019).
15. Skoulidis, F. *et al.* Co-occurring genomic alterations define major subsets of KRAS-mutant lung adenocarcinoma with distinct biology, immune profiles, and therapeutic vulnerabilities. *Cancer Discov.* **5**,

861–878 (2015).

16. Jackson, E. L. *et al.* Analysis of lung tumor initiation and progression using conditional expression of oncogenic K-ras. *Genes Dev.* **15**, 3243–3248 (2001).

17. DuPage, M., Dooley, A. L. & Jacks, T. Conditional mouse lung cancer models using adenoviral or lentiviral delivery of Cre recombinase. *Nat. Protoc.* (2009) doi:10.1038/nprot.2009.95.

18. Jackson, E. L. *et al.* The differential effects of mutant p53 alleles on advanced murine lung cancer. *Cancer Res.* **65**, 10280–10288 (2005).

19. Giangreco, A., Groot, K. R. & Janes, S. M. Lung cancer and lung stem cells: Strange bedfellows? *Am. J. Respir. Crit. Care Med.* **175**, 547–553 (2007).

20. Giangreco, A., Reynolds, S. D. & Stripp, B. R. Terminal bronchioles harbor a unique airway stem cell population that localizes to the bronchoalveolar duct junction. *Am. J. Pathol.* **161**, 173–182 (2002).

21. Bender Kim, C. F. *et al.* Identification of bronchioalveolar stem cells in normal lung and lung cancer. *Cell* **121**, 823–835 (2005).

22. Zhao, L., Yee, M. & O'Reilly, M. A. Transdifferentiation of alveolar epithelial type II to type I cells is controlled by opposing TGF-β and BMP signaling. *Am. J. Physiol. - Lung Cell. Mol. Physiol.* **305**, 409–418 (2013).

23. Liu, Y. *et al.* FoxM1 mediates the progenitor function of type II epithelial cells in repairing alveolar injury induced by Pseudomonas aeruginosa. *J. Exp. Med.* **208**, 1473–1484 (2011).

24. Watson, A., Madsen, J. & Clark, H. W. SP-A and SP-D: Dual Functioning Immune Molecules With Antiviral and Immunomodulatory Properties. *Front. Immunol.* **11**, 1–17 (2021).

25. Liu, Z. *et al.* An obligatory role for club cells in preventing obliterative bronchiolitis in lung transplants. *JCI Insight* **4**, (2019).

26. Yokoyama, T. *et al.* Depletion of club cells attenuates bleomycin-induced lung injury and fibrosis in mice. *J. Inflamm. (United Kingdom)* **14**, 1–9 (2017).

27. Sutherland, K. D. *et al.* Multiple cells-of-origin of mutant K-Ras-induced mouse lung adenocarcinoma. *Proc. Natl. Acad. Sci. U. S. A.* (2014) doi:10.1073/pnas.1319963111.

28. Xu, X. *et al.* Evidence for type II cells as cells of origin of K-Ras -Induced distal lung adenocarcinoma. *Proc. Natl. Acad. Sci. U. S. A.* (2012) doi:10.1073/pnas.1112499109.

29. Settembre, C. *et al.* A lysosome-to-nucleus signalling mechanism senses and regulates the lysosome via mTOR and TFEB. *EMBO J.* **31**, 1095–1108 (2012).

30. El-Houjeiri, L. *et al.* The Transcription Factors TFEB and TFE3 Link

the FLCN-AMPK Signaling Axis to Innate Immune Response and Pathogen Resistance. *Cell Rep.* **26**, 3613-3628.e6 (2019).

31. Nishimura, T. & Tooze, S. A. Emerging roles of ATG proteins and membrane lipids in autophagosome formation. *Cell Discov.* **6**, (2020).

32. Runwal, G. *et al.* LC3-positive structures are prominent in autophagy-deficient cells. *Sci. Rep.* **9**, 1–14 (2019).

33. Guo, J. Y. *et al.* Autophagy suppresses progression of K-ras-induced lung tumors to oncocytomas and maintains lipid homeostasis. *Genes Dev.* **27**, 1447–1461 (2013).

34. Guo, J. Y. & White, E. Autophagy is required for mitochondrial function, lipid metabolism, growth, and fate of KRASG12D-driven lung tumors. *Autophagy* **9**, 1636–1638 (2013).

35. Aman, Y. *et al.* Autophagy in healthy aging and disease. *Nat. Aging* **1**, 634–650 (2021).

36. Marks, M. S. & Seabra, M. C. 2001_Marks_melanosome membrane review_Heitor. *Nat. Rev. | Mol. Cell Biol.* **2**, 1–11 (2001).

37. Raposo, G., Marks, M. S. & Cutler, D. F. Lysosome-related organelles: driving post-Golgi compartments into specialisation. *Curr. Opin. Cell Biol.* **19**, 394–401 (2007).

38. Jani, R. A., Mahanty, S. & Setty, S. R. G. SNAREs in the maturation and function of LROs. *Bioarchitecture* **6**, 1–11 (2016).

39. Langemeyer, L., Fröhlich, F. & Ungermann, C. Rab GTPase Function in Endosome and Lysosome Biogenesis. *Trends Cell Biol.* **28**, 957–970 (2018).

40. Schmitz, G. & Müller, G. Structure and function of lamellar bodies, lipid-protein complexes involved in storage and secretion of cellular lipids. *J. Lipid Res.* **32**, 1539–70 (1991).

41. Williams, M. C. Conversion of lamellar body membranes into tubular myelin in alveoli of fetal rat lungs. *J. Cell Biol.* (1977) doi:10.1083/jcb.72.2.260.

42. Voorhout, W. F. *et al.* Surfactant protein A is localized at the corners of the pulmonary tubular myelin lattice. *J. Histochem. Cytochem.* (1991) doi:10.1177/39.10.1940306.

43. CONVERSION TUBULAR OF IN BODY OF MEMBRANES RAT INTO MARY C . WILLIAMS From the Cardiovascular Research Institute and Department of Anatomy , University of California , San Francisco , California 94143 ABSTRACT Fluid-filled lumina of fetal rat lungs contai. **72**, 260–277 (1977).

44. Veldhuizen, R., Nag, K., Orgeig, S. & Possmayer, F. The role of lipids in pulmonary surfactant. *Biochim. Biophys. Acta - Mol. Basis Dis.* **1408**, 90–108 (1998).

45. Kahn, M. C., Anderson, G. J., Anyan, W. R. & Hall, S. B.

Phosphatidylcholine molecular species of calf lung surfactant. *Am. J. Physiol. - Lung Cell. Mol. Physiol.* (1995) doi:10.1152/ajplung.1995.269.5.l567.

46. Surfactant, J. Surfactant phospholipids : synthesis. (1992).

47. Besnard, V. *et al.* Deletion of Scap in alveolar type II cells influences lung lipid homeostasis and identifies a compensatory role for pulmonary lipofibroblasts. *J. Biol. Chem.* **284**, 4018–4030 (2009).

48. Jain, D. *et al.* SP-A is necessary for increased clearance of alveolar DPPC with hyperventilation or secretagogues. *Am. J. Physiol. - Lung Cell. Mol. Physiol.* **284**, 759–765 (2003).

49. Pol, A., Gross, S. P. & Parton, R. G. Biogenesis of the multifunctional lipid droplet: Lipids, proteins, and sites. *J. Cell Biol.* **204**, 635–646 (2014).

50. Bridges, J. P. *et al.* LPCAT1 regulates surfactant phospholipid synthesis and is required for transitioning to air breathing in mice. *J. Clin. Invest.* **120**, 1736–1748 (2010).

51. Agassandian, M. & Mallampalli, R. K. Surfactant phospholipid metabolism. *Biochim. Biophys. Acta - Mol. Cell Biol. Lipids* **1831**, 612–625 (2013).

52. Wang, P. *et al.* Proteomic analysis of lamellar bodies isolated from rat lungs. *BMC Cell Biol.* **9**, (2008).

53. Weaver, T. E. Synthesis, processing and secretion of surfactant proteins B and C. *Biochim. Biophys. Acta - Mol. Basis Dis.* **1408**, 173–179 (1998).

54. WertSE_WhitsettJA_DevBiol1993.

55. Ross, M., Krol, S., Janshoff, A. & Galla, H. J. Kinetics of phospholipid insertion into monolayers containing the lung surfactant proteins SP-B or SP-C. *Eur. Biophys. J.* **31**, 52–61 (2002).

56. Glasser, S. W. *et al.* Altered stability of pulmonary surfactant in SP-C-deficient mice. *Proc. Natl. Acad. Sci. U. S. A.* **98**, 6366–6371 (2001).

57. Johansson, J. & Curstedt, T. Molecular structures and interactions of pulmonary surfactant components. *Eur. J. Biochem.* **244**, 675–693 (1997).

58. Stahlman, M. T., Gray, M. P., Falconieri, M. W., Whitsett, J. A. & Weaver, T. E. *Lamellar Body Formation in Normal and Surfactant Protein B-Deficient Fetal Mice*. (2000).

59. Kuroki, Y., Mason, R. J. & Voelker, D. R. Alveolar type II cells express a high-affinity receptor for pulmonary surfactant protein A. *Proc. Natl. Acad. Sci. U. S. A.* **85**, 5566–5570 (1988).

60. Ban, N. *et al.* ABCA3 as a lipid transporter in pulmonary surfactant biogenesis. *J. Biol. Chem.* **282**, 9628–9634 (2007).

61. Cheong, N. *et al.* ABCA3 is critical for lamellar body biogenesis in

vivo. *J. Biol. Chem.* (2007) doi:10.1074/jbc.M703927200.

62. Patel, A. S. *et al.* Paracrine stimulation of surfactant secretion by extracellular ATP in response to mechanical deformation. *Am. J. Physiol. - Lung Cell. Mol. Physiol.* **289**, 489–496 (2005).

63. Frick, M., Eschertzhuber, S., Haller, T., Mair, N. & Dietl, P. *Secretion in Alveolar Type II Cells at the Interface of Constitutive and Regulated Exocytosis. Am. J. Respir. Cell Mol. Biol* vol. 25 www.atsjournals.org (2001).

64. Haller, T., Auktor, K., Frick, M., Mair, N. & Dietl, A. P. Threshold calcium levels for lamellar body exocytosis in type II pneumocytes. *Am. J. Physiol. - Lung Cell. Mol. Physiol.* **277**, 893–900 (1999).

65. Andreeva, A. V., Kutuzov, M. A. & Voyno-Yasenetskaya, T. A. Regulation of surfactant secretion in alveolar type II cells. *Am. J. Physiol. - Lung Cell. Mol. Physiol.* **293**, (2007).

66. Haller, T., Ortmayr, J., Friedrich, F., Vo¨lklvo¨lkl, H. & Dietl, P. *Dynamics of surfactant release in alveolar type II cells. Cell Biology* vol. 95 www.pnas.org. (1998).

67. Bates, S. R., Xu, J., Dodia, C. & Fisher, A. B. Macrophages primed by overnight culture demonstrate a marked stimulation of surfactant protein A degradation. *Am. J. Physiol. - Lung Cell. Mol. Physiol.* **273**, 831–839 (1997).

68. Wright, J. R. & Youmans, D. C. Degradation of surfactant lipids and surfactant protein A by alveolar macrophages in vitro. *Am. J. Physiol. - Lung Cell. Mol. Physiol.* **268**, (1995).

69. Rider, E. D., Ikegami, M. & Jobe, A. H. Localization of alveolar surfactant clearance in rabbit lung cells. *Am. J. Physiol. - Lung Cell. Mol. Physiol.* **263**, (1992).

70. Quintero, O. A. & Wright, J. R. Clearance of surfactant lipids by neutrophils and macrophages isolated from the acutely inflamed lung. *Am. J. Physiol. - Lung Cell. Mol. Physiol.* **282**, 330–339 (2002).

71. Kurath-Koller, S., Resch, B., Kraschl, R., Windpassinger, C. & Eber, E. Surfactant Protein B Deficiency Caused by Homozygous C248X Mutation—A Case Report and Review of the Literature. *Am. J. Perinatol. Reports* **05**, e053–e059 (2015).

72. Bullard, J. E., Wert, S. E., Whitsett, J. A., Dean, M. & Nogee, L. M. ABCA3 mutations associated with pediatric interstitial lung disease. *Am. J. Respir. Crit. Care Med.* **172**, 1026–1031 (2005).

73. Huizing, M. *et al.* Hermansky–Pudlak syndrome: Mutation update. *Hum. Mutat.* **41**, 543–580 (2020).

74. Guttentag, S. H. *et al.* Defective surfactant secretion in a mouse model of Hermansky-Pudlak syndrome. *Am. J. Respir. Cell Mol. Biol.* **33**, 14–21 (2005).

75. Marín, I., Egmond, W. N. & Haastert, P. J. M. The Roco protein

family: a functional perspective. *FASEB J.* **22**, 3103–3110 (2008).

76. Bosgraaf, L. & Van Haastert, P. J. M. Roc, a Ras/GTPase domain in complex proteins. *Biochim. Biophys. Acta - Mol. Cell Res.* **1643**, 5–10 (2003).

77. Reimer, J. M. *et al.* Structure of LRRK1 and mechanisms of autoinhibition and activation. *Nat. Struct. Mol. Biol.* **30**, 1735–1745 (2023).

78. Biskup, S. *et al.* Dynamic and redundant regulation of LRRK2 and LRRK1 expression. *BMC Neurosci.* **8**, 1–11 (2007).

79. Myasnikov, A. *et al.* Structural analysis of the full-length human LRRK2. *Cell* **184**, 3519-3527.e10 (2021).

80. Snead, D. M. *et al. Structural basis for Parkinson's disease-linked LRRK2's binding to microtubules. Nature Structural and Molecular Biology* vol. 29 (Springer US, 2022).

81. Mills, R. D. *et al.* The Roc-COR tandem domain of leucine-rich repeat kinase 2 forms dimers and exhibits conventional Ras-like GTPase properties. *J. Neurochem.* **147**, 409–428 (2018).

82. Deyaert, E. *et al.* A homologue of the Parkinson's disease-associated protein LRRK2 undergoes a monomer-dimer transition during GTP turnover. *Nat. Commun.* **8**, 1–12 (2017).

83. Deniston, C. K. *et al.* Structure of LRRK2 in Parkinson's disease and model for microtubule interaction. *Nature* **588**, 344–349 (2020).

84. Rubio, J. P. *et al.* Deep sequencing of the LRRK2 gene in 14,002 individuals reveals evidence of purifying selection and independent origin of the p.Arg1628Pro mutation in Europe. *Hum. Mutat.* **33**, 1087–1098 (2012).

85. Bardien, S., Lesage, S., Brice, A. & Carr, J. Genetic characteristics of leucine-rich repeat kinase 2 (LRRK2) associated Parkinson's disease. *Park. Relat. Disord.* **17**, 501–508 (2011).

86. Nuytemans, K., Theuns, J., Cruts, M. & Van Broeckhoven, C. Genetic etiology of Parkinson disease associated with mutations in the SNCA, PARK2, PINK1, PARK7, and LRRK2 genes: A mutation update. *Hum. Mutat.* **31**, 763–780 (2010).

87. Lewis, P. A. *et al.* The R1441C mutation of LRRK2 disrupts GTP hydrolysis. *Biochem. Biophys. Res. Commun.* **357**, 668–671 (2007).

88. Guo, L. *et al.* The Parkinson's disease-associated protein, leucine-rich repeat kinase 2 (LRRK2), is an authentic GTPase thatstimulates kinase activity. *Exp. Cell Res.* **313**, 3658–3670 (2007).

89. Orenstein, S. J. *et al.* Interplay of LRRK2 with chaperone-mediated autophagy. *Nat. Neurosci.* **16**, 394–406 (2013).

90. Ferrazza, R. *et al.* LRRK2 deficiency impacts ceramide metabolism in brain. *Biochem. Biophys. Res. Commun.* **478**, 1141–1146 (2016).

91. Wang, X. *et al.* Understanding LRRK2 kinase activity in preclinical

models and human subjects through quantitative analysis of LRRK2 and pT73 Rab10. *Sci. Rep.* **11**, 1–17 (2021).

92. Steger, M. *et al.* Phosphoproteomics reveals that Parkinson's disease kinase LRRK2 regulates a subset of Rab GTPases. *Elife* **5**, 1–28 (2016).

93. Waschbüsch, D. *et al.* LRRK2 transport is regulated by its novel interacting partner Rab32. *PLoS One* **9**, (2014).

94. Greggio, E. *et al.* The Parkinson's disease kinase LRRK2 autophosphorylates its GTPase domain at multiple sites. *Biochem. Biophys. Res. Commun.* **389**, 449–454 (2009).

95. Gloeckner, C. J. *et al.* Phosphopeptide analysis reveals two discrete clusters of phosphorylation in the N-terminus and the Roc domain of the Parkinson-disease associated protein kinase LRRK2. *J. Proteome Res.* **9**, 1738–1745 (2010).

96. Pungaliya, P. P. *et al.* Identification and characterization of a leucine-rich repeat kinase 2 (LRRK2) consensus phosphorylation motif. *PLoS One* **5**, 1–13 (2010).

97. Kluss, J. H. *et al.* Detection of endogenous S1292 LRRK2 autophosphorylation in mouse tissue as a readout for kinase activity. *npj Park. Dis.* **4**, 1–5 (2018).

98. Sheng, Z. *et al.* Ser1292 autophosphorylation is an indicator of LRRK2 kinase activity and contributes to the cellular effects of PD mutations. *Sci. Transl. Med.* **4**, (2012).

99. Wang, J. & Song, W. Regulation of LRRK2 promoter activity and gene expression by Sp1. *Mol. Brain* **9**, 1–13 (2016).

100. Szmeja, Z. Recenzja podręcznika pt. „CT Teaching Manual. A Systematic Approach to CT Reading". *Otolaryngol. Pol.* **62**, 117 (2008).

101. Brandeis, M. *et al.* The structure-specific endonuclease activity was intrinsic to XPG. An anti-XPG antibody 5. **371**, 435–438 (1994).

102. Dynan, W. S. & Tjian, R. The promoter-specific transcription factor Sp1 binds to upstream sequences in the SV40 early promoter. *Cell* **35**, 79–87 (1983).

103. Snoderly-Foster, L. J. & Olivas, W. M. Regulation of Parkinson's disease-associated genes by Pumilio proteins and microRNAs in SH-SY5Y neuronal cells. *PLoS One* **17**, 1–25 (2022).

104. Wang, H. *et al.* MiR-205 Regulates LRRK2 Expression in Dopamine Neurons in Parkinson's Disease through Methylation Modification. *Iran. J. Public Health* **51**, 1637–1647 (2022).

105. Bohn, J. A. *et al.* Identification of diverse target RNAs that are functionally regulated by human pumilio proteins. *Nucleic Acids Res.* **46**, 362–386 (2018).

106. Nishanth, M. J. & Simon, B. Functions, mechanisms and regulation

of Pumilio/Puf family RNA binding proteins: a comprehensive review. *Mol. Biol. Rep.* **47**, 785–807 (2020).

107. Giesert, F. *et al.* Expression Analysis of Lrrk1, Lrrk2 and Lrrk2 Splice Variants in Mice. *PLoS One* **8**, (2013).

108. Vlachakis, D. *et al.* Insights into the influence of specific splicing events on the structural organization of LRRK2. *Int. J. Mol. Sci.* **19**, 1–13 (2018).

109. Trabzuni, D. *et al.* Fine-Mapping, Gene Expression and Splicing Analysis of the Disease Associated LRRK2 Locus. *PLoS One* **8**, (2013).

110. Trabzuni, D. *et al.* Quality control parameters on a large dataset of regionally dissected human control brains for whole genome expression studies. *J. Neurochem.* **119**, 275–282 (2011).

111. J bioi Chern, M. J. 11. Hershko, A. & Ciechanover, A. A. *14. Seufert, W. Jentsch, S. EMBO J* **248**, 1773–1784 (1995).

112. Mao, Y. Structure, Dynamics and Function of the 26S Proteasome. *Subcell. Biochem.* **96**, 1–151 (2021).

113. Ding, X. & Goldberg, M. S. Regulation of LRRK2 stability by the E3 ubiquitin ligase CHIP. *PLoS One* **4**, (2009).

114. Ko, H. S. *et al.* CHIP regulates leucine-rich repeat kinase-2 ubiquitination, degradation, and toxicity. *Proc. Natl. Acad. Sci. U. S. A.* **106**, 2897–2902 (2009).

115. Chiang, H. L. & Dice, J. F. Peptide sequences that target proteins for enhanced degradation during serum withdrawal. *J. Biol. Chem.* **263**, 6797–6805 (1988).

116. Tedesco, B., Vendredy, L., Timmerman, V. & Poletti, A. The chaperone-assisted selective autophagy complex dynamics and dysfunctions. *Autophagy* **19**, 1619–1641 (2023).

117. Wojewska, D. N. & Kortholt, A. Lrrk2 targeting strategies as potential treatment of parkinson's disease. *Biomolecules* **11**, (2021).

118. Deng, X. *et al.* Characterization of a selective inhibitor of the Parkinson's disease kinase LRRK2. *Nat. Chem. Biol.* **7**, 203–205 (2011).

119. Reith, A. D. *et al.* GSK2578215A; A potent and highly selective 2-arylmethyloxy-5-substitutent- N-arylbenzamide LRRK2 kinase inhibitor. *Bioorganic Med. Chem. Lett.* **22**, 5625–5629 (2012).

120. Fell, M. J. *et al.* MLi-2, a potent, selective, and centrally active compound for exploring the therapeutic potential and safety of LRRK2 kinase inhibition. *J. Pharmacol. Exp. Ther.* (2015) doi:10.1124/jpet.115.227587.

121. Kingwell, K. LRRK2-targeted Parkinson disease drug advances into phase III. *Nat. Rev. Drug Discov.* **22**, 3–5 (2023).

122. Rinaldi, C. & Wood, M. J. A. Antisense oligonucleotides: The next

frontier for treatment of neurological disorders. *Nat. Rev. Neurol.* **14**, 9–22 (2018).

123. Fusco, D. Di *et al.* Antisense oligonucleotide: Basic concepts and therapeutic application in inflammatory bowel disease. *Front. Pharmacol.* **10**, (2019).

124. Miklavc, P. *et al.* Surfactant secretion in LRRK2 knock-out rats: Changes in lamellar body morphology and rate of exocytosis. *PLoS One* (2014) doi:10.1371/journal.pone.0084926.

125. Herzig, M. C. *et al.* LRRK2 protein levels are determined by kinase function and are crucial for kidney and lung homeostasis in mice. *Hum. Mol. Genet.* **20**, 4209–4223 (2011).

126. Baptista, M. A. S. *et al.* LRRK2 inhibitors induce reversible changes in nonhuman primate lungs without measurable pulmonary deficits. *Sci. Transl. Med.* **12**, (2020).

127. Contat, C. *et al.* Combined deletion of Glut1 and Glut3 impairs lung adenocarcinoma growth. *Elife* (2020) doi:10.7554/eLife.53618.

128. Sanaei, M. J., Razi, S., Pourbagheri-Sigaroodi, A. & Bashash, D. The PI3K/Akt/mTOR pathway in lung cancer; oncogenic alterations, therapeutic opportunities, challenges, and a glance at the application of nanoparticles. *Transl. Oncol.* **18**, 101364 (2022).

129. Liang, S. Q. *et al.* mTOR mediates a mechanism of resistance to chemotherapy and defines a rational combination strategy to treat KRAS-mutant lung cancer. *Oncogene* **38**, 622–636 (2019).

130. Gardet, A. *et al.* LRRK2 Is Involved in the IFN-γ Response and Host Response to Pathogens. *J. Immunol.* **185**, 5577–5585 (2010).

131. Cook, D. A. *et al.* LRRK2 levels in immune cells are increased in Parkinson's disease. *npj Park. Dis.* **3**, 1–11 (2017).

132. Eguchi, T. *et al.* LRRK2 and its substrate Rab GTPases are sequentially targeted onto stressed lysosomes and maintain their homeostasis. *Proc. Natl. Acad. Sci. U. S. A.* (2018) doi:10.1073/pnas.1812196115.

133. Jacquet, A. de R. *et al.* The lrrk2 g2019s mutation alters astrocyte-to-neuron communication via extracellular vesicles and induces neuron atrophy in a human ipsc-derived model of parkinson's disease. *Elife* **10**, 1–37 (2021).

134. Bonet-Ponce, L. *et al.* LRRK2 mediates tubulation and vesicle sorting from lysosomes. *Sci. Adv.* **6**, 1–16 (2020).

135. Baptista, M. A. S. *et al.* Loss of leucine-rich repeat kinase 2 (LRRK2) in rats leads to progressive abnormal phenotypes in peripheral organs. *PLoS One* **8**, 1–16 (2013).

136. Torday, J., Hua, J. & Slavin, R. Metabolism and fate of neutral lipids of fetal lung fibroblast origin. *Biochim. Biophys. Acta (BBA)/Lipids Lipid Metab.* **1254**, 198–206 (1995).

137. Torday, J. S. & Rehan, V. K. Stretch-stimulated surfactant synthesis is coordinated by the paracrine actions of PTHrP and leptin. *Am. J. Physiol. - Lung Cell. Mol. Physiol.* **283**, 130–135 (2002).

138. Miklavc, P. *et al.* Surfactant secretion in LRRK2 knock-out rats: Changes in lamellar body morphology and rate of exocytosis. *PLoS One* **9**, (2014).

139. Liu, Q., Bautista-gomez, J., Higgins, D. A., Yu, J. & Xiong, Y. Dysregulation of the AP2M1 phosphorylation cycle by LRRK2 impairs endocytosis and leads to dopaminergic neurodegeneration. **3555**, 1–15 (2021).

140. Araki, M., Ito, K., Takatori, S., Ito, G. & Tomita, T. BORCS6 is involved in the enlargement of lung lamellar bodies in Lrrk2 knockout mice . *Hum. Mol. Genet.* **00**, 1–14 (2021).

141. Yakhine-Diop, S. M. S. *et al.* Metabolic alterations in plasma from patients with familial and idiopathic Parkinson's disease. *Aging (Albany. NY).* **12**, 16690–16708 (2020).

142. Galper, J. *et al.* Lipid pathway dysfunction is prevalent in patients with Parkinson's disease. *Brain* **145**, 3472–3487 (2022).

143. Tong, Y. *et al.* R1441C mutation in LRRK2 impairs dopaminergic neurotransmission in mice. *Proc. Natl. Acad. Sci. U. S. A.* **106**, 14622–14627 (2009).

144. Dickens, J. A. *et al.* Novel insights into surfactant protein C trafficking revealed through the study of a pathogenic mutant. *Eur. Respir. J.* **59**, (2022).

145. Lebovitz, C. B. *et al.* Cross-cancer profiling of molecular alterations within the human autophagy interaction network. *Autophagy* **11**, 1668–1687 (2015).

146. Ma, Q. *et al.* Identification and validation of key genes associated with non-small-cell lung cancer. *J. Cell. Physiol.* **234**, 22742–22752 (2019).

147. Lebovitz, C. *et al.* Loss of Parkinson's susceptibility gene LRRK2 promotes carcinogen-induced lung tumorigenesis. *Sci. Rep.* **11**, 1–14 (2021).

148. Schwab, A. J. & Ebert, A. D. Neurite Aggregation and Calcium Dysfunction in iPSC-Derived Sensory Neurons with Parkinson's Disease-Related LRRK2 G2019S Mutation. *Stem Cell Reports* **5**, 1039–1052 (2015).

149. MacLeod, D. *et al.* The Familial Parkinsonism Gene LRRK2 Regulates Neurite Process Morphology. *Neuron* **52**, 587–593 (2006).

150. Nguyen, A. P. T. *et al.* Dopaminergic neurodegeneration induced by Parkinson's disease-linked G2019S LRRK2 is dependent on kinase and GTPase activity. *Proc. Natl. Acad. Sci. U. S. A.* **117**, 17296–

17307 (2020).

151. Greggio, E. *et al.* Kinase activity is required for the toxic effects of mutant LRRK2/dardarin. *Neurobiol. Dis.* **23**, 329–341 (2006).

152. Boecker, C. A., Goldsmith, J., Dou, D., Cajka, G. G. & Holzbaur, E. L. F. Increased LRRK2 kinase activity alters neuronal autophagy by disrupting the axonal transport of autophagosomes. *Curr. Biol.* **31**, 2140-2154.e6 (2021).

153. Ludtmann, M. H. R. *et al.* LRRK2 deficiency induced mitochondrial Ca 2+ efflux inhibition can be rescued by Na + /Ca 2+ /Li + exchanger upregulation. *Cell Death Dis.* **10**, (2019).

154. Walter, J. *et al.* Neural Stem Cells of Parkinson's Disease Patients Exhibit Aberrant Mitochondrial Morphology and Functionality. *Stem Cell Reports* **12**, 878–889 (2019).

155. Iaccarino, C. *et al.* Apoptotic mechanisms in mutant LRRK2-mediated cell death. *Hum. Mol. Genet.* **16**, 1319–1326 (2007).

156. Antoniou, N. *et al.* A motif within the armadillo repeat of Parkinson's-linked LRRK2 interacts with FADD to hijack the extrinsic death pathway. *Sci. Rep.* **8**, 1–17 (2018).

157. Albanese, F. *et al.* Constitutive silencing of LRRK2 kinase activity leads to early glucocerebrosidase deregulation and late impairment of autophagy in vivo. *Neurobiol. Dis.* **159**, 105487 (2021).

158. Manzoni, C. *et al.* MTOR independent regulation of macroautophagy by Leucine Rich Repeat Kinase 2 via Beclin-1. *Sci. Rep.* **6**, (2016).

159. Manzoni, C. *et al.* Inhibition of LRRK2 kinase activity stimulates macroautophagy. *Biochim. Biophys. Acta - Mol. Cell Res.* **1833**, 2900–2910 (2013).

160. Nabar, N. R. *et al.* LRRK2 is required for CD38-mediated NAADP-Ca2+ signaling and the downstream activation of TFEB (transcription factor EB) in immune cells. *Autophagy* **18**, 204–222 (2022).

161. Malavasi, F. *et al.* Evolution and function of the ADP ribosyl cyclase/CD38 gene family in physiology and pathology. *Physiol. Rev.* **88**, 841–886 (2008).

162. Buller, C. L. *et al.* A GSK-3/TSC2/mTOR pathway regulates glucose uptake and GLUT1 glucose transporter expression. *Am. J. Physiol. - Cell Physiol.* **295**, 836–843 (2008).

163. Mossmann, D., Park, S. & Hall, M. N. mTOR signalling and cellular metabolism are mutual determinants in cancer. *Nat. Rev. Cancer* **18**, 744–757 (2018).

Curriculum Vitae

Aspasia GKASTI
PhD Candidate in Molecular Life Sciences, EPFL

Personal Data

Address: Passage de Montriond 4, 1006 Lausanne, Switzerland

Phone:

+41 78 658 87 81

E-mail address:

aspa-gs@hotmail.com

Linkedin:

https://www.linkedin.com/in/aspasia-gkasti-03-ag188

Date of birth:

21st March 1992

Nationality: Greek

Languages

-English: C1

-French: A2

-Greek: Native

Computer Skills

-Microsoft Office tools (Word, Excel, Power Point, Outllook),Qupath, ImageJ, GraphPad Prism

Interests

Volleyball, Tennis, Padel, Running, Travelling, Volunteering

Work experience

PhD Candidate in Molecular Life Sciences   **Mar. 2019 -Present**
EPFL (École Polytechnique Fédérale de Lausanne), Lausanne, Switzerland
- Investigated the role of Lrrk2 in lung adenocarcinoma (planning and execution of experiments, analysis- interpretation- and presentation of experimental data)
- Supervised a master student
- Worked as a teaching assistant

Lung Cancer Research Intern   **Sep. 2018 – Jan. 2019**
EPFL (École Polytechnique Fédérale de Lausanne), Lausanne, Switzerland
- Studied the effects of neutrophil depletion on immune cells *in vivo*

Graduate Research Assistant   **Feb. 2018- Jul. 2018**
EPFL (École Polytechnique Fédérale de Lausanne), Lausanne, Switzerland
- Tested methods for neutrophil depletion *in vivo* (publication doi: 10.1038/s41467-020-16596-9)

Undergraduate Research Assistant   **Mar.2014 – Nov.2014**
BSCR (Biomedical Sciences Research Center) Alexander Fleming, Athens, Greece
- Investigated the role of the protein Talin-1 in tumour angiogenesis

Molecular Diagnostic Laboratory Intern   **June 2013 - Aug. 2013**
Locus Medicus, Athens, Greece
- Performed molecular diagnostic tests on human samples for the detection of mutations and viral infections

Education

PhD in Molecular Life Sciences   **March 2019 -Present**
EPFL (École Polytechnique Fédérale de Lausanne), Lausanne, Switzerland

MSc in Medical and Pharmaceutical Biotechnology   **Sep. 2016 - Feb 2019**
IMC University of Applied Sciences Krems, Austria

BSc in Molecular Biology and Genetics   **Sep. 2010- July 2015**
Democritus University of Thrace, Alexandroupolis, Greece